Universidad Nacional Autónoma de México

Posgrado en Ciencia e Ingeniería de Materiales
Centro de Física Aplicada y Tecnología Avanzada

DESIGN, FABRICATION, AND CHARACTERIZATION OF ONE-DIMENSIONAL PHOTONIC CRYSTALS BASED ON POROUS SILICON

TESIS

QUE PARA OPTAR POR EL GRADO DE:
DOCTOR EN CIENCIA E INGENERÍA DE MATERIALES

PRESENTA:

M. en C. CRISTIAN FELIPE RAMÍREZ GUTIÉRREZ

TUTOR
DR. MARIO ENRIQUE RODRÍGUEZ GARCÍA
Centro de Física Aplicada y Tecnología Avanzada, UNAM

MIEMBROS DEL COMITÉ TUTOR
DRA. BEATRIZ MARCELA MILLÁN MALO
Centro de Física Aplicada y Tecnología Avanzada, UNAM
DRA. ELSA GUTIÉRREZ CORTÉZ
Facultad de Estudio Superiores de Cuautitlan, UNAM

Ciudad de México, Julio 2019.

UNAM – Dirección General de Bibliotecas
Tesis Digitales
Restricciones de uso

DERECHOS RESERVADOS ©
PROHIBIDA SU REPRODUCCIÓN TOTAL O PARCIAL

Todo el material contenido en esta tesis esta protegido por la Ley Federal del Derecho de Autor (LFDA) de los Estados Unidos Mexicanos (México).

El uso de imágenes, fragmentos de videos, y demás material que sea objeto de protección de los derechos de autor, será exclusivamente para fines educativos e informativos y deberá citar la fuente donde la obtuvo mencionando el autor o autores. Cualquier uso distinto como el lucro, reproducción, edición o modificación, será perseguido y sancionado por el respectivo titular de los Derechos de Autor.

Contents

Introduction **3**

1 Porous silicon formation **8**

1.1 Silicon crystalline structure 9

1.2 Chemistry of Si dilution 9

1.2.1 Direct dilution of Si 10

1.2.2 Si oxidizing 11

1.2.3 Dilution of Si oxide 12

1.2.4 Hydrogen terminations 12

1.3 J-V curve for silicon in an HF-based media 12

1.4 Manufacturing of porous silicon by electrochemical etching 15

2 Experimental Methods **17**

2.1 Sample description 18

2.2 Equipment description 18

2.2.1 In-situ photoacoustic equipment 18

2.2.2 Characterization techniques 22

2.3 In situ photoacoustic characterization for porous silicon growing: Detection principles 24

2.3.1 Reflectance Corrections 26

2.3.2 Time dependence of photoacoustic signal 28

2.3.3 Photoacoustic signal wavelength dependence 32

2.4 Modeling of the photoacoustic signal 34

2.4.1 PA amplitude fitting 40

3 Optical properties of porous silicon 48

3.1 PSi optical constants determination 48

3.1.1 Thin-film calculations 49

3.1.2 Genetic fit 52

3.2 PSi photoluminescence 57

3.2.1 PL experiments on single and double PSi layers 60

4 One-dimensional photonic crystal based on porous silicon 67

4.1 Etch Calibration 68

4.1.1 Substrate quality determination by PCR imaging 69

4.1.2 Etch calibration by in-situ photoacoustics 70

4.2 Design and Simulation of Photonic Structures. 74

4.3 Fabrication and characterization of photonic structures 76

4.4 Tolerance fabrication 84

5 Conclusions 85

References **88**

A *In situ* Photoacoustic signals from calibration series **101**

B *UV-Vis spectra of calibration series* **103**

C Effects of the interface roughness in the optical response of one-dimensional photonic crystals **104**

D Papers published during PhD studies **112**

D.1 2016 . . . 112

D.1.1 In situ photoacoustic characterization for porous silicon growing: Detection principles . . . 112

D.1.2 Study of bovine hydroxyapatite obtained by calcination at low heating rates and cooled in furnace air . . . 112

D.2 2017 . . . 113

D.2.1 Modeling the photoacoustic signal during the porous silicon formation 113

D.2.2 Effect of the temperature and sintering time on the thermal, structural,morphological, and vibrational properties of hydroxyapatite derived frompig bone . . . 113

D.3 2018 . . . 113

D.3.1 Photoluminescence study of porous p-type silicon: Identification of radiative transitions . . . 113

D.3.2 Porosity and roughness determination of porous silicon thin films by genetic algorithms . . . 114

D.3.3 Optical interferometry and photoacoustics as in-situ techniques to characterize the porous silicon formation: a review . . . 114

D.3.4 A comparative study on heat capacity, magnetization and magnetic susceptibility for a GaAs quantum dot with asymmetric confinement 114

D.3.5 The Influence of the Precipitation Heat Treatment Temperature on the Metallurgical, Microstructure, Thermal Properties, and Microhardness of an Alpha Brass 114

D.4 2019 115

D.4.1 Effects of the interface roughness in the optical response of one-dimensional photonic crystals of porous silicon 115

D.4.2 Impact of a topological defect and Rashba spin-orbit interaction on the thermo-magnetic and optical properties of a 2D semiconductor quantum dot with Gaussian confinement 115

D.4.3 Chapter 14 - Study of microstructural, structural, mechanical, and vibrational properties of defatted trabecular bovine bones: natural sponges 115

Figure List

1 Flowchart of the procedures to design and fabricate PSi photonic crystals. . 7

1.1 (a) Silicon crystalline structure. (b) shows the (111) and the (c) (001) plane view. 9

1.2 Simplified Si dilutions scheme 10

1.3 J-V characteristic curve during the etching process of Si for (a) p-type Si. (b) n-type Si 13

1.4 PSi doublelayer. This figure shows a top layer with a low porosity and down layer with high porosity obtained at 20 mA and 100 mA cm respectively. (c) and (d) show a cross section of PSi films by suing a $< 001 >$ and $< 111 >$ substrates respectively. As can be seen, the porous morphology is dependent of substrate crystalline orientation. 14

1.5 Generic configuration of an electrochemical cell. 15

2.1 Schematic setup used to study in real time the PSi formation process. (a) Electrochemical cell coupled to a photoacoustic with temperate monitoring and control. (b) Acquisition data setup. 19

2.2 Cell scheme designed in SolidWorks. The figure shows the solid isometric orientation of a) empty cell and b) with the platinum guide in it. The c) and d) show inside split views. The lower part of the cell is composed of a screw which fixes the microphone on the back of the silicon substrate and makes an airtight seal of the electrochemical cell and electrical contact with the Si. Also, the electrolyte container ends in a cone of 45° to induce the hydrogen bubbles, produced during the c-Si etching, move across the container walls for reducing the effect of them in the c-Si surface (homogeneous surface etching) and the optical path of photoacoustic cell configuration. 20

2.3 Photos of the complete equipment. (a) It is a complete look. (b) A detailed look of the electronically cell coupled to the photoacoustic system. Also, temperature control. (c) and (d) show a photograph of the developed cell. As can be seen, the silicon sample is fixed from the back of the cell (c) where O-rings seals and pin-up the c-Si sample. 21

2.4 (a) Schematic representation of photoacoustic cell and (b) optical effects. . . 24

2.5 Simulation of reflectance as a function of the $Re(\delta)$. The color scale represents the behaviour of the reflectance as a function of porosity using a Looyenga [1, 2] effective medium mixture rule for the system electrolyte/PS/Si (Figure 2.4(b)). 26

2.6 Photoacoustic signals for four different etching times at 20 mA current anodization. Each one of the etching processes was stopped at 1(a), 2(b), 3(c), and 4(c) photoacoustic cycles. 29

2.7 SEM images of cross sections of PS films growing for 1(a), 2(b), 3(c), and 4(d) photoacoustic cycles 30

2.8 Relationship between photoacoustic cycles and the thickness of the sample. The inset shows that the etching rate for these anodization conditions is $8{,}3 \pm 0{,}1$ nm/s 31

2.9 Photoacoustic signal wavelength dependence. Three different samples growth under the same anodizing condition but monitoring with lasers with different wavelengths. 33

2.10 Cross-section of the photoacoustic cell. The labels s, b, and g correspond to sample, backing, and gas, respectively. 35

2.11 (Color line) The experimental data of the PA signal as a function of the etching time (blue). The inset shows the contribution from the DC component extracted from the experimental data (green). 42

2.12 AC-photoacoustic signal computed from Eq. (2.36), at $T_0 = 0$, in the interval of etching $450 < t < 2700$. It is observed that the modulation comes from the frequency ω_2, i. e., the effect of reflectance in the PS which is related to a period $T \sim 40$s. 42

2.13 Photoacoustic signal of experimental data (blue) and phenomenological model (red). Also the contribution of etching and DC component is shown (green) for the etching time 450 s $< t <$ 1500 s. 44

2.14 Photoacoustic signal of experimental data (blue) and phenomenological model (red). Also the contribution of etch and DC component is shown (green) for the etching time 1500 s $< t <$ 2000 s. 44

2.15 Photoacoustic signal of experimental data (blue) and phenomenological model, for different values of ω_2 and v. The fit has been done with the values $\omega_{21} = \pi/20 \approx 0{,}157$ rad/s, $v_1 = 8$ nm/s (green), $\omega_{22} = 0{,}167$ rad/s, $v_2 = 44$ nm/s (red), and $\omega_{23} = 0{,}170$ rad/s, $v_3 = 60$ nm/s (black). 46

2.16 Photoacoustic signal of experimental data (blue) and phenomenological model, for different values of ω_2 and v. The fit has been done with the values $\omega_{24} = 0{,}166$ rad/s, $v_1 = 50$ nm/s (black), and $\omega_{25} = 0{,}165$ rad/s, $v_2 = 43$ nm/s (red) 47

3.1 Multilayer structure form with $m+1$ interfaces. This scheme shows the field amplitudes of the moving waves from left to right. Parameter σ_3 represents the RMS roughness of the third interface and Δh the size of the irregularities in nanometers. It is assumed that $\Delta h << \lambda$. 51

3.2 SEM image of sample fabricated under the same condition of sample S4. (a) Shows a closer zoom of the interface Air/Psi, (b) shows a closer look of the interface PSi/Si and it is highlighted the rough interface, and (c) shows the complete cross section of the PSi sample. 51

3.3 Measured reflectance of PSi layers (black dash line), genetic fit without roughness (blue dash line), genetic fit with roughness (red line), and comparison between simulated and measured reflectance (black line) 55

3.4 Penalty function evaluation progress. Each point represents the best adapted individual of each generation. 57

3.5 Photoacoustic amplitude obtained during the Si etching. (a) Single layer etched at 5 mA cm $^{-2}$, (b) single layer etched at 40 mA cm $^{-2}$, (c) bilayer etched at 5 and 40 mA $^{-2}$, (d) bilayer etched at 40 mA cm-2 and 5 mA cm^{-2}. 61

3.6 Top SEM view of the PSi layers: (a) layer A, (b) layer B, (c) bilayer AB, and (d) bilayer BA. 62

3.7 Cross section SEM images of PSi layer A (a), layer B (b), bilayer AB (c), and bilayer BA (d). 62

3.8 PL spectra as a function of temperature for (a) layer A, (b) layer B, (c) bilayer AB, and (d) bilayer BA. 64

3.9 Temporal evolution of the PL spectra for layers A and B from 0 min (initial step) to 319 min (final stage) under continuous laser fluency. 65

3.10 (a) PL spectra of layer A taken at 11 K (black line), 319 min after continuous laser fluency (green line), and 24 h after turning off laser incidence (blue line). (b) The same experiment for layer B. 66

4.1 Optical constants of crystalline silicon. (a) Refractive index. (b) Extinction coefficient. 68

4.2 (a) Shows the silicon wafer and the scanned places by PCR radiometry. (b) PCR amplitude and phase of five points located at the center of the wafer. (c) Thermal images across the wafer. Laser beam radius 500μm. Frequency 1 kHz. 70

4.3 Calibration series parameters. (a) PA time as a function of current density that exhibits an exponential decay behavior. (b) Average porosity determined by GA and PA-SEM, (c) and (d) interfaces roughness as a function of current density determined by GA fitting of UV-Vis spectrum. (d) Etching rate that exhibits linear behaviour. 72

4.4 Cross-section SEM images of calibration series. (a) 5 mA cm^{-2}, (b) 10 mA cm^{-2}, (c) 15 mA cm^{-2}, (d) 20 mA cm^{-2}, (e) 30 mA cm^{-2}, (f) 40 mA cm^{-2}, (g) 50 mA cm^{-2} y (h) 60 mA cm^{-2}. 73

4.5 Schematic of the multilayer structure composed by n films that form $n+1$ interfaces. The order of subscripts indicates the propagation direction. . . . 75

4.6 PA amplitude during DBRs fabrication. (a) DBR550, (c) DBR700, (e) DBR750. (b), (d), and (f) are its respective cross-section SEM images. Inset in (a) shows the current density profile used for DBRs fabrication. 78

4.7 Reflectance spectra simulated (blue line) and measured (black line) for (a) DBR550, (b) DBR700, and (c) DBR750. 80

4.8 PA amplitude during OMC fabrication. (a) OMC1, (c) OMC2, and its respective SEM cross-section images (b) and (d). Inset in (a) and (c) shows the current density profile used. 82

4.9 Reflectance spectra simulated (blue line) and measured (black line) of (a)OMC1 and (b)OMC2 83

A.1 PA amplitude of the calibration series. Anodization current density from 5 mA cm^{-2} to 60 mA cm^{-2} 102

B.1 UV-Vis reflectance spectrum of the calibration series. Anodization current density from 5 mA cm^{-2} to 60 mA cm^{-2} 103

C.1 Numerical results. (a) Single PSi layer with a roughness contribution in PSi/c-Si (substrate) interface. PSi DBR optical response with roughness contribution on: (b) Air/DBR interface, (c) DBR2 internal interfaces (H/L), and (d) DBR/c-Si (Substrate) interface. 106

C.2 Aspect ratio between ideal reflectance and the reflectance with roughness contributions for: (a) Single PSi layer case, (b) DBR1, (c) DBR2, and (d) DBR3. 107

C.3 (a) Comparison of the optical response of ideal PSi DBR (blue line), the fitted reflectance with a contribution of H/L interface roughness of 20 nm (red line), and the experimental PSi DBR fabricated (black line). (b) and (c) SEM images of cross section of PSi DBR. (d) and (e) correspond top view of high porosity and low porosity layer respectively. 111

Table List

1.1 Manufacture parameters and its heights on PSi porosity, etching rate, and critical current density. 16

2.1 Values of the real part of the refractive index and the etching rate for the films of PS obtained during 1, 2 , 3, and 4 photoacoustic cycles. The anodizing current was 20 mA and the ratio Ethanol/HF was 7:3 in volume. 32

2.2 Reported values for the thermal and electric properties of Si at different doped levels. 41

2.3 Values for the relevant parameters used in Eq. (2.36) in order to reproduce Fig. 2.12. 43

3.1 Shows the parameter values of best fit for UV-Vis spectra of PSi films shown in Fig. 3.3 and the comparison between the thickness measured by SEM and by the genetic fit. 56

4.1 Parameters design of photonic PSi structures. 76

4.2 Experimental parameters used for PSi PhC fabrication. The thickness of each layer was determined by SEM. 77

C.1 It shows the simulated values for the single layer PSi and the DBRs. Also, it contains the place where rough contribution is located and the sequence of the structure. 105

C.2 Etch conditions used for PSi DBR fabrication. SEM determined the layer thickness and roughness, and the porosity and refractive index calculated by fitting the UV-Vis spectrum. 109

Dedication

The brave choice is ever the family...

Because of my Mom and Dad,

my Siblings and their Sons,

and always there, to my other ***Soul****.*

La elección valiente es siempre la familia ...

A mi Madre y Padre,

a mis Hermanas y Hermano y sus Hijos,

y siempre allí, a mi otra ***Alma.***

Acknowledgments

I want to thanks my Ph.D. scholarship provided by CONACyT (Consejo Nacional de Ciencia y Tecnología de México). Also, the financial support received from the PAEP program of UNAM.

I'm eternally gratefully with the technical support for the assistance in photonic crystal characterization received from Laboratorio Nacional de Caracterización de Materiales (LaNCaM) from CFATA-UNAM .

Thanks to Alicia del Real and Carmen Peza Ledezma for SEM measurements, and Beatriz Millán Malo for her assistance in the simulations and XRD characterizations.

Thanks to Ivan Alonso Lujan Cabrera from Universidad Autónoma de Queretaro for his experimental support in the porous silicon fabrication.

Introduction

The investigations around porous silicon (PSi) technology are focused on PSi for optoelectronic and photonics. Surface modification of crystalline silicon (c-Si) such as porosification in the nanometric range has allowed tuning optical, electrical, thermal, and mechanical properties of Si expanding the applications of PSi in diverse fields. Especially, the field of sensing allows the study of physical, chemical, and biochemical interactions of transducing systems. Nowadays, groundbreaking sensors are based on photonic crystals (PhC)[3], porous materials [4], and bio-inspired structures that allow accurate and reliable measures through its optical and electrical response [5, 6, 7, 8]. Moreover, PChs are fundamental components of other optoelectronic devices such as light emitting diodes (LEDs) and lasers. One of the promissory materials for these applications is porous silicon (PSi) thin films. PSi is a nanostructured and nanocomposite material with diverse porous morphology, different surface chemistry, and the large surface area, commonly obtained through etching in hydrofluoric based (HF) aqueous media. The self-limited character of the PSi electrochemical reaction allows the fabrication of homogeneous films and heterostructures [9, 10]. Besides, it is possible to custom PSi properties by changing the growing parameters, oxidation grade [11, 12], and surface chemistry through functionalization [9, 13, 14]. This fact makes the PSi an excellent candidate to develop photonic structures such as porous distributed Bragg reflector (DBR) and optical microcavities (OMC) [15, 16]. However, the physicochemical properties of PSi are critically dependent on the etching parameters, and there are not theoretical models to predict the refractive index, absorption coefficient, thickness, porosity, and interfaces roughness. Nonetheless, in-situ methodologies based on infrared spectroscopy [17], laser interferometry [18, 19, 20], and photoacoustics [20, 21, 22] had been developed as an alternative to monitoring the formation in real time of PSi thin films that allows feedback

to control the electrochemical reaction.

There are several reports about DBRs based on PSi and methods to fabricate tunable PSi thin films [23, 24, 25, 26]. The first one, related to the fabrication of PSi DBRs in the infrared range, was reported by Vincent [27]. In his work, the manufacture of DBR was performed applying a square waveform of current density to produce a periodic structure of the PSi layer. This type of current profiles produced a periodic structure with an interleaved high (n_H) and low (n_L) refractive index.

Nevertheless, some limitations were found related to the thickness of the layers, bandwidth, spectral position, and optical quality. Pavesi *et al.* [28] used the same methodology [27] but changing the time of etching of the high refractive index film randomly. This means that the obtained DBR is, in fact, a random system. Setzu *et al.* [29] studied the optical properties of multilayered PSi system; they fabricated DBR using square waveform of current density selected arbitrary, and they presented a methodology to control the interface roughness to improve the optical quality of PSi structures. Other works are related to applications of PSi DBR as chemical and biological sensors [30, 31, 32], and mirrors for photovoltaics devices [33, 34]. Nevertheless, a common characteristic in the works mentioned before is that the fabrication of the PSi DBRs relays in always using an arbitrary value of current density and etching time, resulting in a random optical response referred to the position of photonic band-gap, limited bandwidths, and low optical quality. This means that there is not a previous design or control during the PSi DBR fabrication. Therefore, it is imperative to mention that random devices are not related to quasi-periodic or disordered photonic structures [35, 36, 37], that in fact, PSi exhibits [38]. The randomness is referred to as no surety of optical properties at determined experimental fabrication conditions. For these reasons, the in-situ monitoring of the fabrication processes is needed to obtain reliable PSi devices. Therefore, intrinsic and extrinsic parameters must be taken into account to produce high quality and reproducible PSi devices. Extrinsic parameters are closely related to the fabrication methods of PSi films to obtain a tunable thickness, reflective index (porosity), and smoothness interfaces. On the other hand, intrinsic parameters are associated with the substrate quality which is directly related to the carrier distribution, the crystalline quality, and the optothermal surface stability [39, 40, 41].

Psi has been studied widely in the last years, from formation mechanisms until physico-chemical properties. One of the most common techniques to study optical properties of

PSi is UV-Vis spectrophotometry that lets to measure the optical response to determine the dielectric function of PSi. However, determination of optical constants and dielectric function from reflectance, transmittance, or absorbance spectra requires physical models that give information on all interaction between radiation and matter. In the case of thin films, optical models involve a bunch of variables such as refractive index, extinction coefficient, thickness, porosity, interface roughness, and other intrinsic and extrinsic parameters. Hence, the estimation of optical constants represents an inverse problem. This problem has been attacked from two points of view: the first corresponds to using mathematical methods of approximation from the perspective of optimization which is done by comparing the experimental measure with the physical model and choosing the best parameters that adjust and reproduce the experimental spectrum. The second point of view corresponds to using complementary characterization techniques that allow reducing the number of unknown parameters in the optical model; for example, knowing the thickness of the films, number of layers, porosity and roughness by means of scanning electron microscopy (SEM), gravimetry, atomic force microscopy (ATM); and that these variables are fixed parameters.

In this direction, there are few works about techniques that monitor the formation in real time of PSi films. Particularly interferometry and photoacoustic are non-contact and non-destructive techniques that can follow the etching rate, the evolution of thickness, porosity, and interfaces roughness in real time. However, the main limitation of interferometry is related to the monitoring of temperature during the chemical reaction; this is a crucial parameter because it changes the etching kinetics. As a solution for this limitation, this group have reported a differential photoacoustic system as well as a systematic study on following the PSi films formation [22, 21]. The photoacoustic (PA) signal contains information about the electrochemical reaction [22], optical, and thermal properties of layered systems [20, 42]. Indeed, photoacoustic is an excellent technique to follow the fabrication process and reach tunable optical devices based on PSi. Therefore, this work is focused on establishing a methodology based on photoacoustic to monitor the DBR fabrication and a procedure to design and customize optical devices based on PSi such as DBRs and OMC. This means, the design and fabrication of PSi photonic structures at defined wavelength ranges.

According to this, this work shows key-points such as substrate quality, etching rate, porosity determination, and a model to determine the refractive index of porous media by using

photoacoustic and effective medium approximation (EMA)[1, 2, 43] that are necessaries to fabricate high-quality DBRs and OMC. Fabrication of tunable PSi thin films requires a previous determination of c-Si substrate quality. This can be done by using photocarrier radiometry spectroscopy (PCR) imaging. PCR is a non-contact, non-intrusive, and non-destructive technique that has been used for mapping the implant dose across the Si wafers [44, 45, 46] as well as to determine the carrier distribution on p and n Si wafers [47]. In this work, the perspectives mentioned have been used in a complementary manner. This means, the fabrication of PS structures by electrochemical etching monitored and controlled by *in-situ* photoacoustic technique which allows determining the number of layers formed, its porosity, thickness, and roughness. These parameters can be determined through a direct correlation between the anodization current and geometry of the electrochemical cell, which is calibrated and extrapolated using SEM measurements of the manufactured films. These parameters are fixed variables that should no longer be adjusted in the optical model. This allows the adjustment of the optical constants (η and k) to be efficient and precise, reducing the optimization problem to few variables. The porosity, optical constants, interface roughness, and thickness of PSi films are determined simultaneously from the adjustment of experimental measurements of specular reflectance. For this, we have opted for random search methods based on evolutionary algorithms such as genetic algorithms. On the other hand, two methods (characteristic matrix and transfer matrix) of summing [1] have been considered from classical electrodynamics to simulate the optical response of multilayer arrays and have been implemented in Matlab.

Using the optical model that estimates the optical response of multilayer PSi films, we performs simulations of reflectance spectra to design a variety of multilayer arrays according to the requirement, providing the conditions in the electrochemical attack to fabricate optical devices such as Distributed Bragg Reflectors (DBR) Optical Microcavities (OMC) (Fraby-Perot resonator).

This work is divided into two parts: a first stage study the fabrication process of PSi based on photoacoustic technique for monitoring *in situ* of the electrochemical etching and the optical characterization of thin films of PS by UV-VIS spectrophotometry and

[1] Methods to obtain the total optical response of thin film multilayer systems

photoluminescence. In this first step, I present a series of published papers that contains the detailed description of the photoacoustic technique, the principles of detection and phenomenological model. After, I introduced another set of papers where optical properties of porous silicon were studied. A second part consists of the simulation, design, and fitting of reflectance spectra in the UV-VIS range of DBR's and OMC's using a method based on *in-situ* photoacoustic, genetic algorithms that allow fabricating optical devices of PSi with reproducibility and good fabrication tolerance. Therefore, the published papers appear like chapters in this document.

Thus, calibration of the electrochemical setup was performed. Then, a specific design of the device configuration was carried out, and finally, the fabrication monitoring and control processes are described. Figure 1 summarizes all steps followed that combine simulation, design, and experimental.

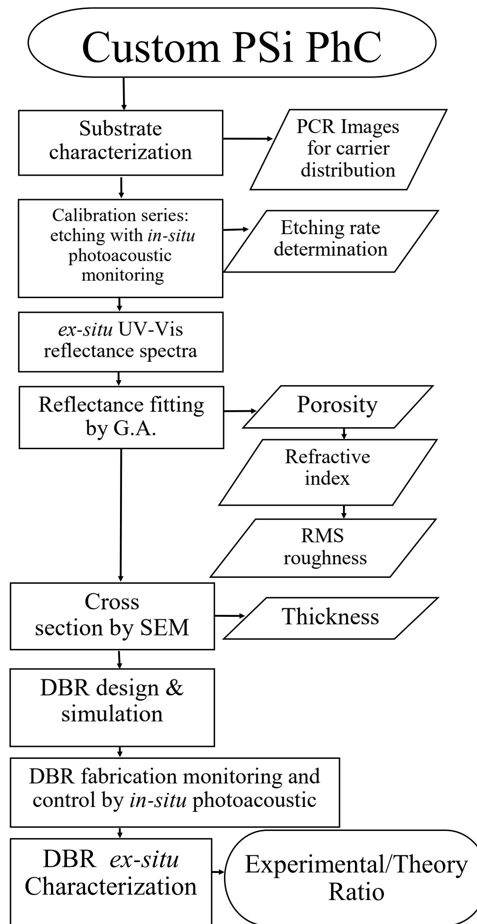

Figure 1: Flowchart of the procedures to design and fabricate PSi photonic crystals.

CHAPTER 1

Porous silicon formation

Silicon etching process was used first by Uhlir of the Bell [48] laboratories in 1956 with the aim of polishing crystalline silicon substrates (c-Si) in hydrofluoric acid (HF) aqueous media. However, it was observed that polishing only occurred after a threshold current density, and below this, the surface of the c-Si becomes of different colours. Turner [49] reported similar experiences and reports that the porosity of the substrates of c-Si is depended on HF concentration, temperature, and current density. These kinds of effects below of electro-polishing current did not generate interest, and since 1958 research in the subject focused on the study of oxidized films of PS as dielectrics [50]. In 1990 L. Canham reported that under certain anodizing conditions PSi exhibits efficient photoluminescence at room temperature [51]. Thus, investigations around PSi takes a new approach towards studying the optoelectronic properties its applications.

Other studies about PS focused on the pore morphology and optical properties [52, 53] that resulted in the bases for the study of more complex structures based on multilayers of PSi such as photonic crystals [54], optical microcavities (OMC), distributed Bragg reflectors (DBR) [55], light emitting structures [56], gas and liquid sensors, also functionalized PSi surfaces to be used as biosensors [57, 58]

1.1. Silicon crystalline structure

Crystalline silicon (c-Si) is a semiconductor material located at IV group and 14 of atomic number. It has a cubic diamond-like crystalline structure with sp^3 hybridization so that the bonds of the structure are set in a tetrahedron giving it a coordination number of 4 in each Si atom. The symmetry space group of Si is Fd$\bar{3}$m (227), cell length $a = b = c =$ 5,4317(6)$\AA$. Figure 1.1 (a) shows the Si structure and the (001) and (111) crystallographic planes that are important because of the up and down coordination change as a function of crystalline directions as it shows in Figures 1.1 (b) and (c).

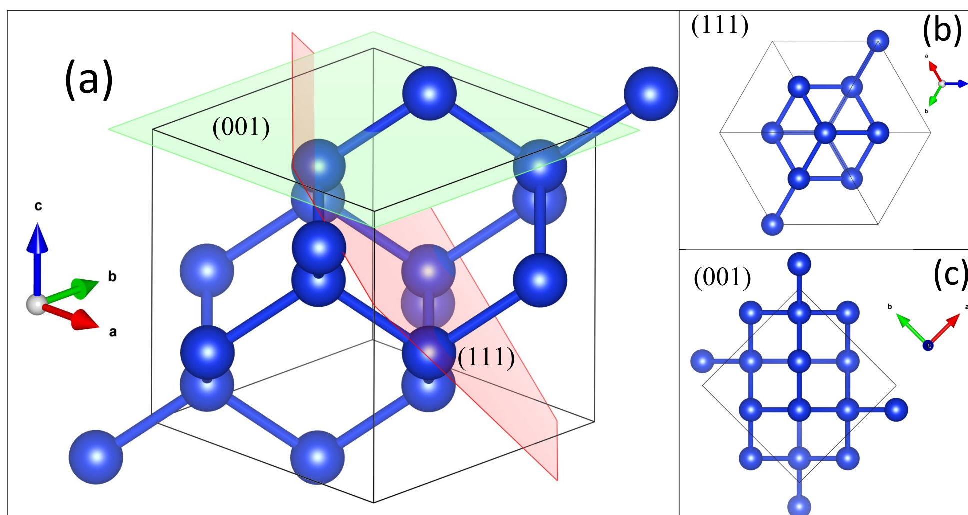

Figure 1.1: (a) Silicon crystalline structure. (b) shows the (111) and the (c) (001) plane view.

1.2. Chemistry of Si dilution

PSi is usually obtained through electrochemical etching where a c-Si sample is used as a sacrifice electrode into contact with an HF-based electrolyte. However, there are other alternative methods to electrochemical anodization such as photoetching which consists of activating the electrochemical reaction with radiation [59], the use of oxidizing agents such (HNO_3) with HF [60] which does not require the application of external electric current.

There are several models to explain the mechanisms of dilution of c-Si and the formation of pores in HF aqueous media. For pore formation or c-Si dilution, the c-Si sample is used as an anode and it is put in contact with an HF solution which is in contact with an inert electrode (cathode) generally made of platinum. When current is circulated through the circuit, the ions of F^{-} in the electrolyte move towards the c-Si surface and react. In general, the etching of c-Si consists of a combination of four different chemical reactions [9]:

1.2.1. Direct dilution of Si

$$\mathrm{Si} + xh^{+} - ye^{-} \rightarrow \mathrm{Si}^{4+} \tag{1.1}$$

where x holes ($h+$, with $x \geq 1$) are consumed together with y electrons ($e-$) injected that contribute to the rest of the required charge. This type of solution turns out to be the most efficient in that only one hole is necessary. In the presence of HF-based electrolytes, the reaction takes the following form [61]:

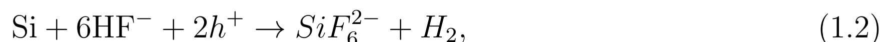

$$\mathrm{Si} + 6\mathrm{HF}^{-} + 2h^{+} \rightarrow SiF_6^{2-} + H_2, \tag{1.2}$$

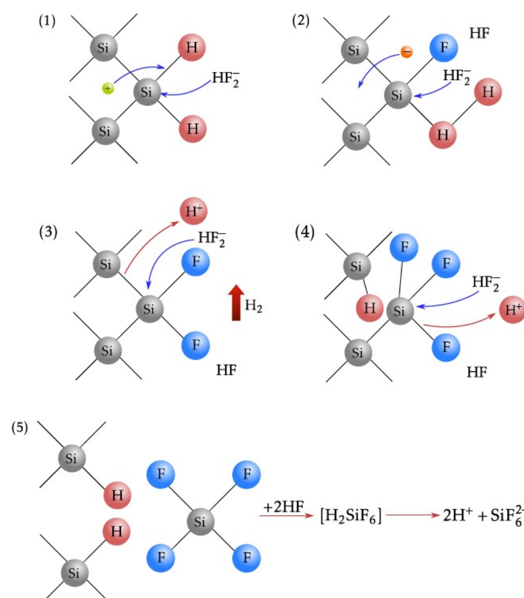

Figure 1.2: Simplified Si dilutions scheme

Fig. 1.2 shows the scheme of the reaction where a hole is injected from the Si bulk towards the Si/electrolyte interface, allowing the Si-Si bonds to weaken. The active species in the electrolyte dissociates near the surface in HF and F^-. When a Si−F bond occurs, a new attack occurs due to the injection of an electron that comes from the previous reaction. Hydrogen gas is released, and the Si atoms are hydrogenated again. The surface returns to its initial state until the injection of a new hole. In general, two holes are necessary to start the process, and the Si with valence 4+ is considered as shown by Ec. 1.2. This reaction is usually called divalent dilution due to the need two charges for the process [62]. According to the equation 1.1, the direct Si dilution can have valence between 1 and 4. However, in most cases it occurs with valence 2. The final product of the reaction is a stable complex $[2H^+ - SiF_6^{2-}]$ or H_2SiF_6.

The direct Si dilution consumes HF and releases H_2, however, in the common reactions the presence of H^+ is possible. This is an indication that the reaction rate is sensitive to pH of the electrolyte and it is possible local pH variations (for example, at the pore ending).

1.2.2. Si oxidizing

The oxidation process of Si can be described by the following reaction:

$$\mathrm{Si} + 4\,\mathrm{h}^+ + 2\,\mathrm{O}^{2-} \longrightarrow \mathrm{SiO_2} \tag{1.3}$$

According to Eq.1.3, four holes participate in Si oxidation process. In the presence of water the reaction takes the form:

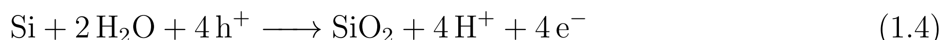

$$\mathrm{Si} + 2\,\mathrm{H_2O} + 4\,\mathrm{h}^+ \longrightarrow \mathrm{SiO_2} + 4\,\mathrm{H}^+ + 4\,\mathrm{e}^- \tag{1.4}$$

This process occurs if the current density is not compensated by F^- ions from the dissociation of the HF. In this regime, the available concentration of HF is less than the amount of water, so the water molecules pass to form Si−O bonds [63]. Thus, Si oxides are easily diluted by HF, and the dilution rate depends on the concentration of HF in the electrolyte.

1.2.3. Dilution of Si oxide

In the pore formation voltage range, Si oxide dilution occurs mainly chemically, i.e. current involved. This reaction can be written as:

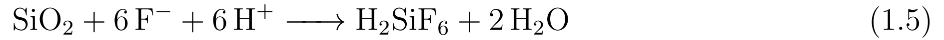

$$\mathrm{SiO_2 + 6\,F^- + 6\,H^+ \longrightarrow H_2SiF_6 + 2\,H_2O} \quad (1.5)$$

This process is coupled with oxide formation and limits the total current density in the system because the oxide generation cannot be higher than the dilution rate (on average). This combined process of oxidation and dilution is known as Si tetravalent dilution since four holes are required.

1.2.4. Hydrogen terminations

$$\mathrm{Si}^x + x\mathrm{H}^+ \longrightarrow \mathrm{SiH}_x, \quad (1.6)$$

where x is the number of covalent bonds on the surface of the Si.

The hydrogen termination on the Si surface can be considered as a passivation process. The passivation rate depends on parameters such as the crystalline direction of the substrate, the temperature and the composition of the electrolyte [63]. Although it is accepted that pore formation is favored by surface defects and irregularities, there are other models to explain the formation of pores, some reviews on the formation of PS can be consulted in the following references [9, 64].

1.3. J-V curve for silicon in an HF-based media

Pore formation is limited by the current density through the circuit. In Fig. 1.3, the current-voltage (J-V) curves for n-type p-type are shown [64], and the electrolyte/semiconductor interface has a similar behavior to a Schottky diode. However, it presents two characteristic peaks in the anodization region. The first peak ($\mathrm{J_{PS}}$) delimits the region in which the

sample is electropolished. In this region, the dilution of Si does not occur directly, since a first oxidation step occurs (valence 4). The chemical reactions for both types of doping are the same and show essential differences when the reaction occurs in the presence of light footnote Radiation of energy greater than the energy gap (E_g) of the Si and when it is not illuminated (dark)). These differences are caused by the formation of holes produced by radiation which react with the ions of F^-.

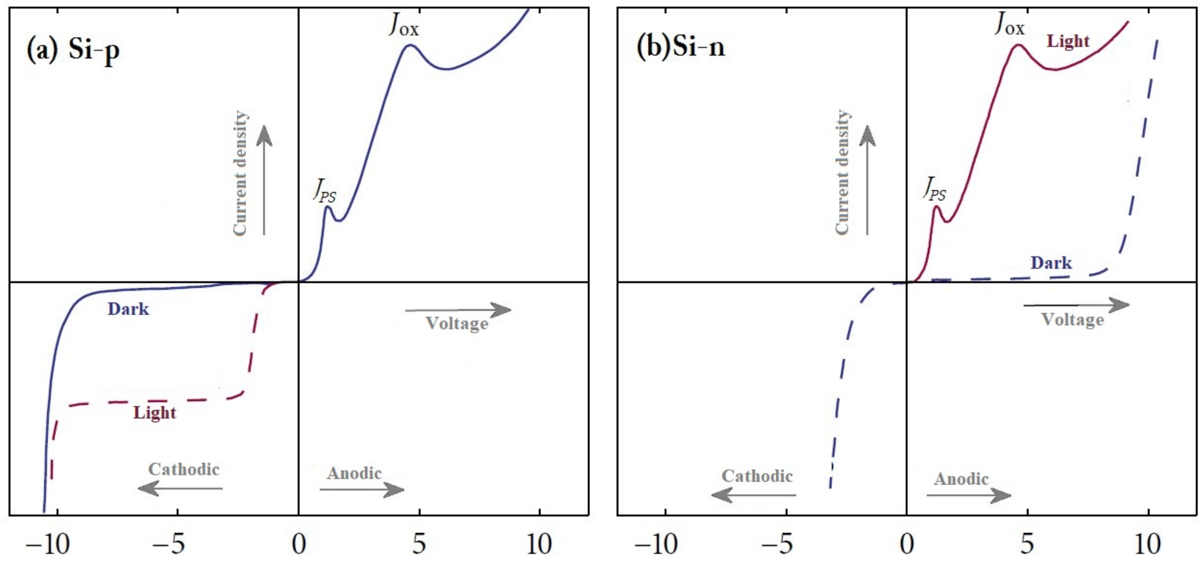

Figure 1.3: J-V characteristic curve during the etching process of Si for (a) p-type Si. (b) n-type Si

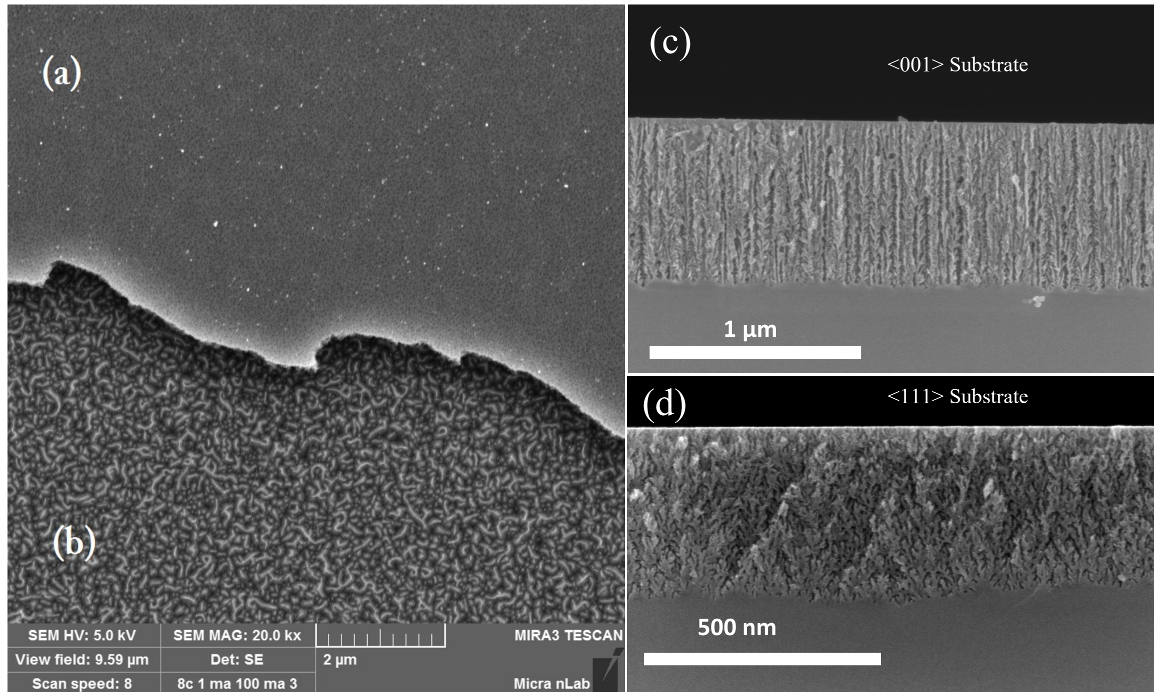

Figure 1.4: PSi doublelayer. This figure shows a top layer with a low porosity and down layer with high porosity obtained at 20 mA and 100 mA cm respectively. (c) and (d) show a cross section of PSi films by suing a $< 001 >$ and $< 111 >$ substrates respectively. As can be seen, the porous morphology is dependent of substrate crystalline orientation.

Fig. 1.3 shows the general trends of J-V behavior of c-Si anodizing. However, today there are not models that allow predicting the behavior of the J-V curve and how other environmental conditions affect it. Also, it is not modeled how extrinsic parameters such as temperature, pH of the solution, electrolyte composition, and intrinsic parameters of c-Si wafers like doping type and concentration, carrier distribution, crystalline quality, and crystalline orientation get effects over the porous nucleation.

Despite the mentioned limitations, it is possible to identify parameters that intervene in the etching and act on the morphology of the PS film. The pore size is sensitive to the current density, the resistivity of the substrate and the concentration of HF in the electrolytic solution producing pores ranging from 2 nm to 100 nm before electropolishing. Fig. 1.4 shows the region (a) of attack at nominal 20 mA (nominal) through the circuit in which small pores are observed compared with the region (b) of attack at 100 mA (nominal) where it

is observed a large pore formation near the electropolishing region.

1.4. Manufacturing of porous silicon by electrochemical etching

Currently, there are a large number of reports dedicated to the analysis of different aspects of the formation of porous silicon, including the mechanisms of the chemical reaction. However, the experimental aspects of the manufacturing process are critical, such as the configuration of the electrochemical cell geometry, circuit configuration, among extrinsic other factors. The generic cell to perform the anodization process in c-Si includes the following elements: three electrodes that are immersed in the electrolyte, a current source, a voltmeter and an ammeter (Fig. 1.5).

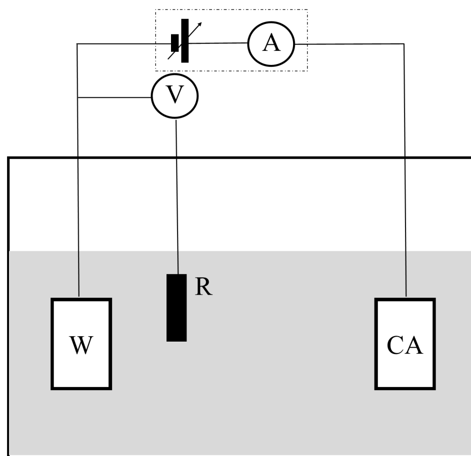

Figure 1.5: Generic configuration of an electrochemical cell.

The silicon electrode is commonly called the working electrode (W), the second is an auxiliary (Counter electrode, CA) and it is an inert electrode (usually platinum) used to close the circuit. Finally, a reference electrode (R) is used which is used to measure the voltage between the counter and the working electrode (W). It should be noted that some configurations of electrochemical cells do not use a reference electrode as it is considered that this can affect the electrode potential. This situation can be improved by using a potentiostat

Table 1.1: Manufacture parameters and its heights on PSi porosity, etching rate, and critical current density.

Parameter	Porosity	etching rate	critical current density
HF concentration $\uparrow$	$\downarrow$	$\downarrow$	$\uparrow$
Current density $\uparrow$	$\uparrow$	$\uparrow$	–
Anodizing time $\uparrow$	$\uparrow$	almost constant	–
Temperature $\uparrow$	–	–	$\uparrow$
p doping level $\uparrow$	$\downarrow$	$\uparrow$	–
n doping level $\uparrow$	$\uparrow$	$\uparrow$	–

which controls the voltage between the working electrode (W) and the counter electrode (AC).

It is clear that the design of the electrochemical cell for the manufacture of PSi must resolve various aspects so that pore formation is controlled and reproducible, it is even possible to couple other sub-systems to monitor in real time pore formation, that's is the case of infrared spectroscopy, real time ellipsometry, interferometry, light scattering, and photoacoustics. On the other hand, the manufacture parameters that have effects on PSi manufacture and its heights are summarized in table 1.1.

CHAPTER 2

Experimental Methods

This section corresponds to the design, construction, and implementation of a differential photoacoustic cell coupled to an electrochemical cell for in-situ monitoring of porous silicon (PSi) formation. In this section, it is shown the detection principles and experimental performance of our developed system.

The photoacoustic methodology proposed in this study permits the obtainment of PS samples with the same characteristics assuming no changes occurred in the impurities distribution across the sample. This means that it is possible to determine the etching rate and the effective refractive index of the sample. Comparing the refractive index with any model of an effective medium [2], such as Looyenga [1], Bruggeman [65], and Maxwell-Garnet [66], this methodology can also determine the porosity of the sample. The method permits monitoring of the etching process using different laser wavelengths. This fact can be used to calculate the refractive index for these wavelengths and to construct a real curve of the effective medium. Another critical issue is the direct relationship between the laser wavelength and the period of the amplitude of the photoacoustic signal.

2.1. Sample description

For all experiments in this thesis, it was used a boron doped Si, $< 100 >$ crystalline orientation, and resistivity 0,001 Ωcm from Polish Corporation of America-USA. Substrates were cut into squares of 14 mm in length; each one was washed using the standard method RCA Silicon wafer organic cleaning [67, 68]. The electrolyte concentration ratio was 3:7 (HF (38 %)/ethanol (99.9 %) in volume), this concentration was selected to provide a good wet surface, allowing homogeneous growth of porous silicon [69]. All samples were fabricated keeping the electrolyte temperature constant at 25 C°.

2.2. Equipment description

2.2.1. In-situ photoacoustic equipment

For photoacoustic experiments, a laser line of 808 nm ($<$200 mW of power by Laser-Mate Group) modulated at 35 Hz, and an electret condenser microphone were used. Pt wire and a Cu ring were used as a counter electrode and as a collector respectively. The anodization current profiles were created using a precision current Source (6220) brand Keithley. During the etching, the photoacoustic amplitude and phase signals were recorded using a Stanford Research SR830 Lock-In Amplifier and GPIB-USB-HS (National Instruments) acquisition card. Figure 2.1 shows a schematic of the complete differential PA system. In Fig. 2.2 (a) and (b) it is shown a schematic of a cell manufactured in PVC. In the laterals, there are square cavities for Peltier cells that are cooled using fans and controlled using a PID control. The c-Si sample is located from the back side and is fixed by a screw that contains the microphone. Fig 2.2 (C) and (d) also shows a guide to controlling the height of the platinum electrode. Fig. 2.3 shows photographs of the complete equipment.

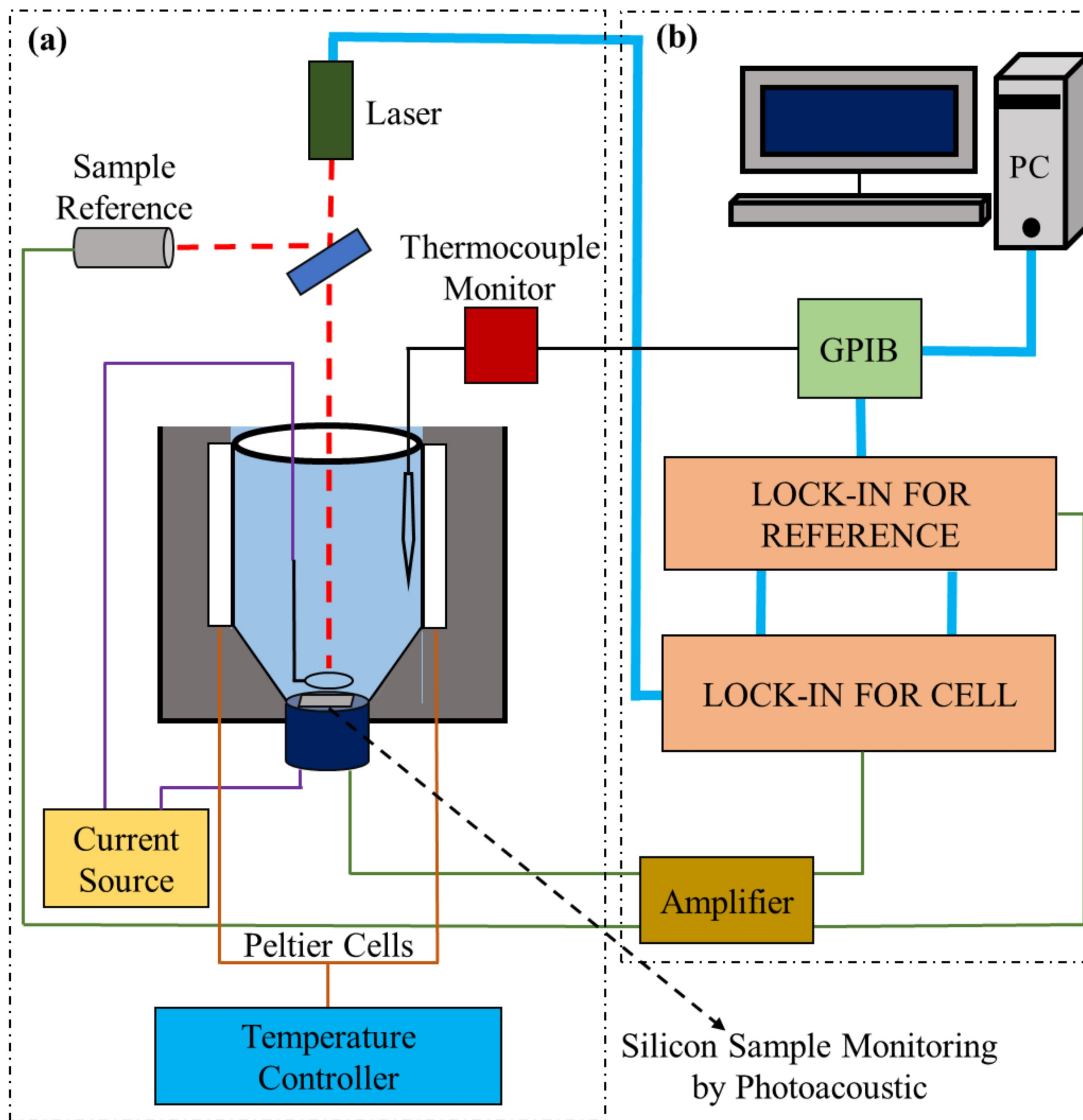

Figure 2.1: Schematic setup used to study in real time the PSi formation process. (a) Electrochemical cell coupled to a photoacoustic with temperate monitoring and control. (b) Acquisition data setup.

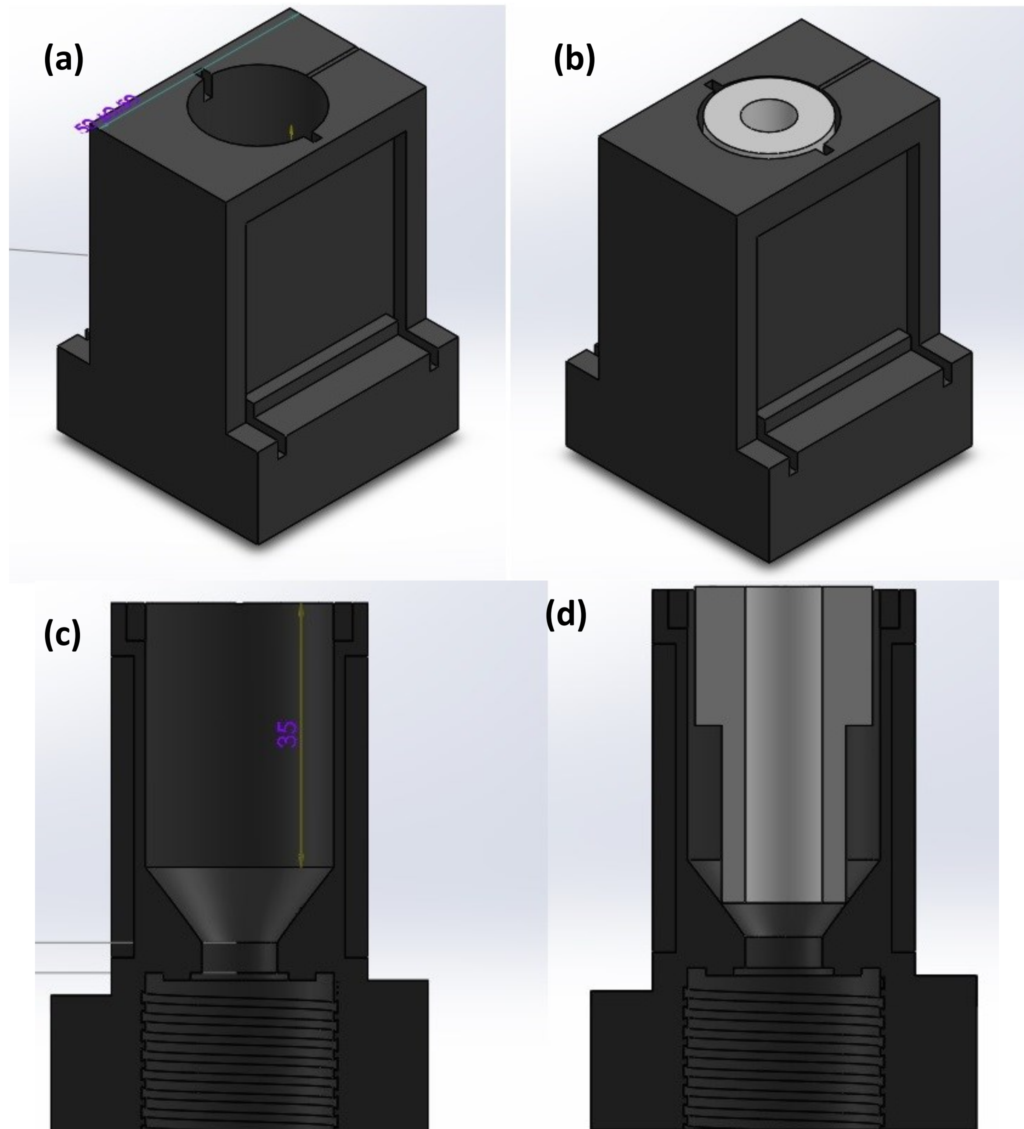

Figure 2.2: Cell scheme designed in SolidWorks. The figure shows the solid isometric orientation of a) empty cell and b) with the platinum guide in it. The c) and d) show inside split views. The lower part of the cell is composed of a screw which fixes the microphone on the back of the silicon substrate and makes an airtight seal of the electrochemical cell and electrical contact with the Si. Also, the electrolyte container ends in a cone of 45° to induce the hydrogen bubbles, produced during the c-Si etching, move across the container walls for reducing the effect of them in the c-Si surface (homogeneous surface etching) and the optical path of photoacoustic cell configuration.

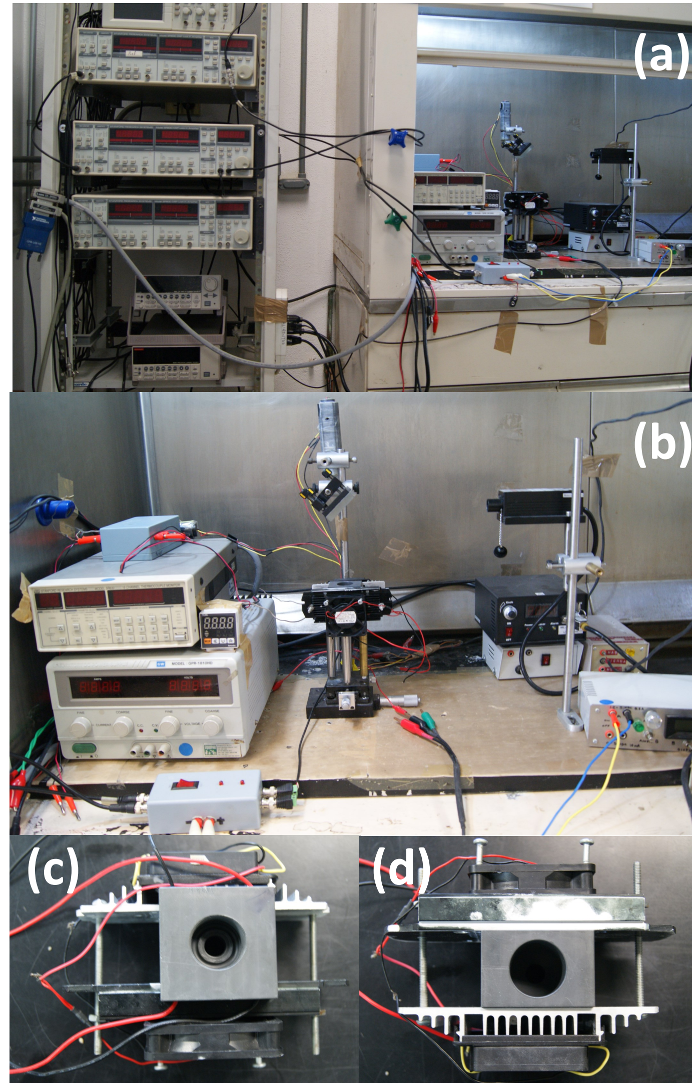

Figure 2.3: Photos of the complete equipment. (a) It is a complete look. (b) A detailed look of the electronically cell coupled to the photoacoustic system. Also, temperature control. (c) and (d) show a photograph of the developed cell. As can be seen, the silicon sample is fixed from the back of the cell (c) where O-rings seals and pin-up the c-Si sample.

2.2.2. Characterization techniques

Scanning electron microscopy SEM

Electron microscopy allows to study the material morphology. This technique was used to study the surface porous morphology and the layer thickness. It was used a Mira3 by TESCAN and Hitachi SU8230 microscopes.

Near specular UV-Vis spectrophotometry

Spectrophotometry is a method to measure how much a material absorbs, reflects, and transmit light by measuring the intensity of light. The basic principle is that each compound absorbs or transmits light over a certain range of wavelength. This measurement can also be used to measure the amount of a known chemical substance. Spectrophotometry is one of the most useful methods of quantitative analysis in various fields such as chemistry, physics, biochemistry, material and chemical engineering and clinical applications. Particularly, it is useful for optical constants calculation.

Optical characterization of PSi films was carried out using a Perkin Elmer UV-Vis Spectrophotometer Lambda 35 in the near-normal (6°) relative specular reflectance mode from 1100 to 210 nm range. The spectrophotometer was self-calibrated using an aluminum mirror, and the samples were measured over the Si substrate. It means that the reflectance is the optical response of the PSi thin film Si substrate (PSi/Si structure).
The spectra were corrected following the Eqs. 2.1 and 2.2 to obtain the absolute reflectance.

$$R(\lambda) = R_{relative}(\lambda) R_{transfer}(\lambda), \tag{2.1}$$

$$R_{transfer}(\lambda) = \frac{R^{(Si)}_{Teo}(\lambda)}{R^{(Si)}_{relative}(\lambda)}, \tag{2.2}$$

where $R(\lambda)$ is the absolute reflectance of the sample (PSi/Si- structure), $R_{transfer}$ is the transfer function of the spectrophotometer built through theoretical reflectance of Si ($R^{(Si)}_{Teo}$) and the measured reflectance of a Si substrate ($R^{(Si)}_{relative}$).

Photoluminescence (PL)

Details about the photoluminescence system, used to perform the optical characterization of the PSi layers, described in this work, was reported elsewhere [70]. The system features an external excitation source as an argon-ion laser LEXEL 95 beam with a wavelength of 488 nm (2.54 eV) with tunable excitation power focused on the sample by a cylindrical lens. Samples were located inside a closed-cycle helium cryostat with temperature control, in a copper sample holder and its temperature varied from 11 to 300 K. The light emission from the sample was focused by a convergent lens in the entrance slit of a Horiba FHR1000 spectrophotometer. To remove the laser reflection, a LP'540 filter was located near the entrance slit. This spectrophotometer has a focal distance of 100 cm, a spectral resolution of 0.010 nm and a diffraction grating of 1800 lines per millimeter. A CCD camera with thermo-electric cooling was used as a photodetector. The PL studies cover two fundamental aspects to determine the presence of quantum confinement and surface states in the PL spectrum. The first experiment was carried out to study the PL temperature dependence from room temperature to 11 K in single layers A, B, and bi layers AB and BA. The second PL study was focused on investigating the dependence of the photoluminescence response vs. laser exposition time, keeping the same laser power 40 mW, to analyze the effect of the optothermal annealing in the quantum confinement and surface states of the PSi sample [71]. In addition, studies were performed to analyze the electronic states involved in optical transitions and participation of bound or free carriers.

Photocarrier radiometry spectroscopy (PCR) imaging

The carrier distribution of c-Si substrates was characterized by using PCR implementing the methodology proposed by Mandelis and Rodriguez-Garcia.[40, 72, 45]. An InGaAs infrared detector with spectral range 0.8-1.8 μm, and a laser 532 nm was modulated from 10 to 5000 Hz. PCR images were taken at 1 kHz with a step size 100 μm, and spot size of 40 μm in the linear regimen. [39] Each image was taken in a 9×9 mm square and a 1 mm gap between areas.

2.3. In situ photoacoustic characterization for porous silicon growing: Detection principles

The main mechanism of the photoacoustic signal generation when there are no physico-chemical changes in the sample is the absorption of modulating light by the sample. The classical theory of the photoacoustic effect in solids, as described by Rosencwaig and Gershoallows, is to formulate the heat flow equations in the cell resulting from the absorption of energy [73]. Figure 2.4(a) shows the geometrical configuration of the PS/Si system. It is characterized by three regions: the region $0 < x < l_g$ is the gas chamber, the Si sample is located in $-(l_b - l_s) < x < 0$, and the region $-l_b < x < -(l_b - l_s)$ represents the PS film. By using this coordinate system, the heat equation in each region can be written as:

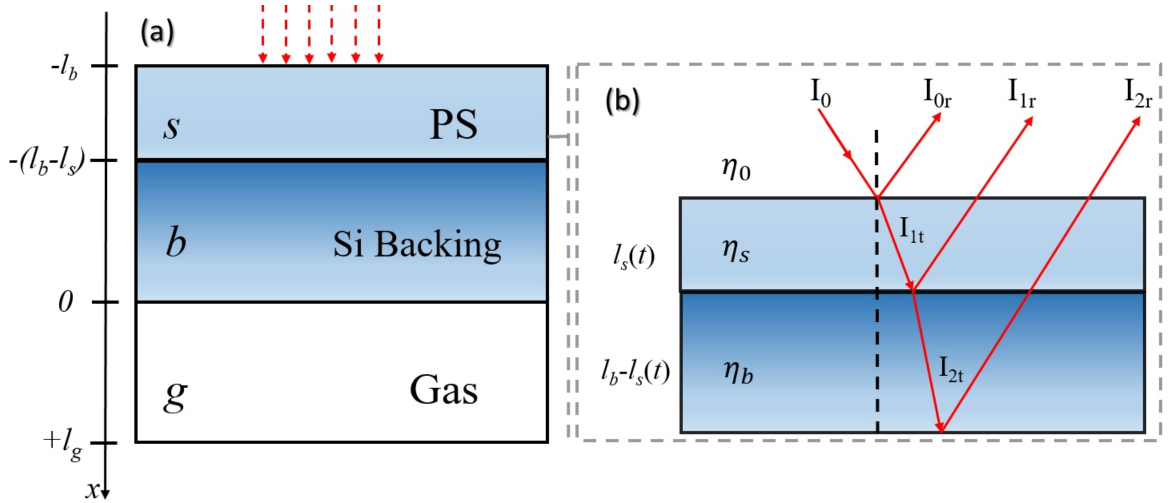

Figure 2.4: (a) Schematic representation of photoacoustic cell and (b) optical effects.

$$\frac{\partial^2 T_s}{\partial x^2} - \frac{1}{\alpha_s}\frac{\partial T_s}{\partial t} = f_s(x,t) + Q(x,t) \quad , \qquad \text{for} \quad -l_b < x < -(l_b - l_s(t)) \quad , \tag{2.3}$$

$$\frac{\partial^2 T_b}{\partial x^2} - \frac{1}{\alpha_b}\frac{\partial T_b}{\partial t} = f_b(x,t), \quad \text{for} \quad -(l_b - l_s(t)) < x < 0, \tag{2.4}$$

and

$$\frac{\partial^2 T_g}{\partial x^2} - \frac{1}{\alpha_g}\frac{\partial T_g}{\partial t} = 0, \quad \text{for} \ \ 0 < x < l_g, \tag{2.5}$$

where $f_{s,b}(x,t)$ and $Q(x,t)$ are the heat sources, produced by the light absorption and electrochemical reaction, respectively. However, the term related to the electrochemical reaction is unknown and is taken as a constant in this study. Also, the Joule effect appears in the sample during the etching process, the main effect of this is the increase in the DC level.

The terms in relation to the light absorption source has the following form:

$$f_s\left(x,t\right) = \frac{\beta_s I_0 \eta_s \left(1 - R(t)\left|_{x=-l_b}\right.\right)}{2k_s} e^{\beta_s x}\left(1 + e^{i\omega t}\right), \tag{2.6}$$

$$f_b\left(x,t\right) = \frac{\beta_b I_{1t} \eta_b \left(1 - R(t)\left|_{x=-(l_b-l_s)}\right.\right)}{2k_b} e^{\beta_b x}\left(1 + e^{i\omega t}\right), \tag{2.7}$$

where I_o is the intensity of the incident light source, I_{1t} is the intensity of transmitted light, ω is the modulated frequency, β_s is the effective absorption coefficient (PS-electrolyte mixture), β_b the absorption coefficient of Si, $\eta_{s,b}$ is the efficiency of the light absorption, $k_{s,b}$ is the thermal conductivity, and R is the reflectance evaluated at the electrolyte/PS ($x = -l_b$) and PS/Si ($x = -(l_b - l_s)$) interfaces. The Eqs. (2.3) to (2.5) must satisfy the Neumann and Dirichlet boundary conditions.

The incidence of the light is by the front of the Si sample, and it is clear that before the etching, $l_s(t = 0) = 0$. When the source is turned on, the electrochemical reaction takes place. As a result of the chemical reaction, the thickness of the PS begins to increase, as does the optical path of the light. The interference effects appear to be the product of the creation of the new interface. Thus, the reflectance (R) now has become thickness dependent. The Figure 2.4(b) shows the schematic representation of the reflection process and the interference effect. Taking into account the above-mentioned effect, the R in the Eqs. (2.6) and (2.7), is now a function of the etching time.

2.3.1. Reflectance Corrections

The system represented in Figure 2.4(b) is composed of three different mediums where the light can propagate. In the case of the silicon etch, the first medium with a refractive index $\tilde{n}_0$ corresponds to the electrolyte composed of Ethanol/HF. The second medium is the PS film with refractive index $\tilde{n}_s$, and finally, the third medium corresponds to silicon backing with $\tilde{n}_b$. The interfaces electrolyte/PS and PS/Si-backing can reflect and transmit the laser beam, but the last interface Si-backing/gas can only reflect, and does not permit the transmission of radiation for the gas. Taking into account that the thickness of the Si backing is bigger than the penetration depth of wavelength λ_0, the fraction of the reflected radiation was determined using a transfer matrix method as follows [74]:

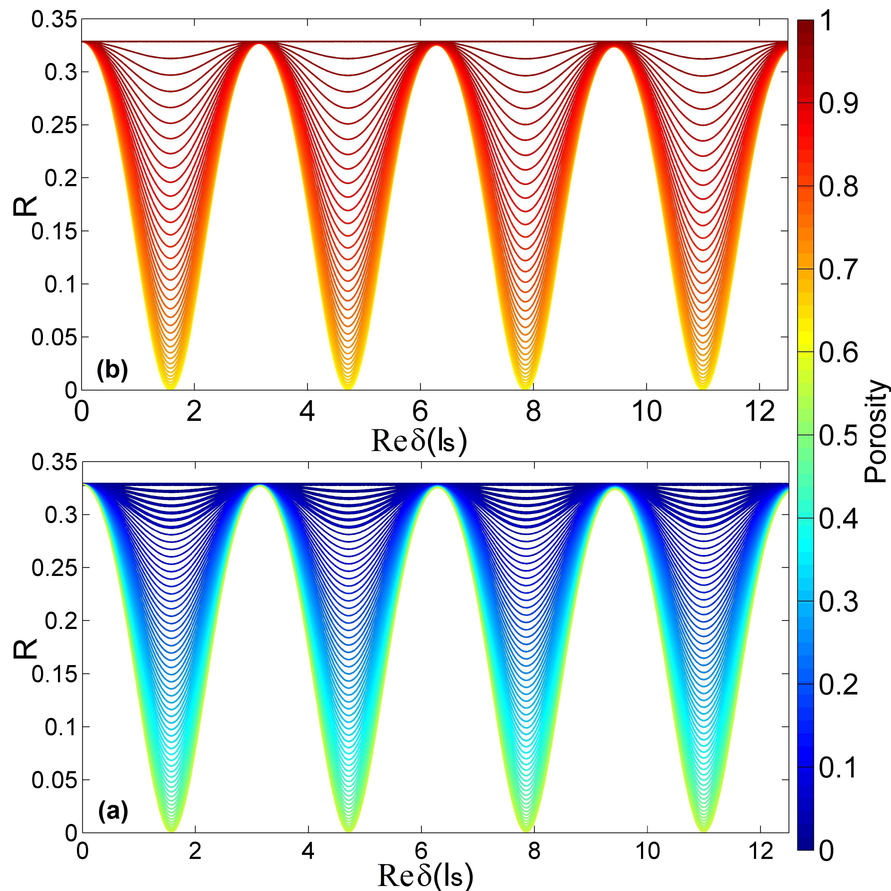

Figure 2.5: Simulation of reflectance as a function of the $Re(\delta)$. The color scale represents the behaviour of the reflectance as a function of porosity using a Looyenga [1, 2] effective medium mixture rule for the system electrolyte/PS/Si (Figure 2.4(b)).

$$R(t) = \left|r^2\right| = \frac{\cos^2(\delta)(\alpha_0 - \alpha_1)^2 + \sin^2(\delta)(\alpha_0\alpha_1 - 1)^2}{\cos^2(\delta)(\alpha_0 + \alpha_1)^2 + \sin^2(\delta)(\alpha_0\alpha_1 + 1)^2}, \tag{2.8}$$

where $\alpha_0 = \tilde{n}_0/\tilde{n}_s$ and $\alpha_1 = \tilde{n}_b/\tilde{n}_s$, using the convention $\tilde{n}_x = n_x + i\kappa_x$, where the real part corresponds to the refractive index and the imaginary part corresponds to the extinction coefficient.

Here is important to note that $l_s(t)$ represents the change in the sample thickness as a function of the time. However, due to the etching process on the front surface of the substrate, it is necessary to consider and take the porosity into account. This means that $\tilde{n}_s$ is, in fact, a function of the porosity p.

$$\delta(t) = \frac{2\pi\tilde{n}_s(p)l_s(t)}{\lambda_0}, \tag{2.9}$$

Figure 2.5(a) and 2.5(b) shows the reflectance changes as a function of the real part of the $\delta(t)$. The color scale represents the changes in the porosity between 0 to 1. For each one of the simulations, a wavelength of 808 nm was used, and $\tilde{n}_s$ was calculated using an effective medium rule for a known porosity [1, 2]. The product $\tilde{n}_s l_s$ that represents the optical path in Eq. (2.9), and these behave as follows: it is possible to have a sample with a high $\tilde{n}_s$ and a thin l_s or a sample with a low $\tilde{n}_s$ and thick l_s and the product is the same. It means that there exist pairs of these parameters that give the same reflectance conditions, for this reason, it is necessary to separate the results into two porosity ranges (see Figure 2.5). It is clear that there are values of $\delta(t)$ in which the reflectance changes between maximum and minimum located at $l_s = \frac{1+2m}{2\tilde{n}_s}\lambda_0$ and $l_s = \frac{m}{2\tilde{n}_s}\lambda_0$. These values show that the reflectance changes as a function of the sample thickness and it is modulated by the relationship between the incident wavelength and the change in the thickness of the sample. This fact will be correlated with the photoacoustic signal for the PS formation in the next section.

This section shows the results obtained from two different experiments: the first experiment consists of the etching of four samples of silicon with the same anodization current and electrolyte composition when the etching time is changed, in order to prove that the

photoacoustic signal is self-modulated by the changes in the reflectance of the heterostructure and that it is periodic. The second experiment consisted of the etching the three samples of silicon using a different wavelength of the laser, to prove the relation shift between the wavelength and the period of the photoacoustic signal.

2.3.2. Time dependence of photoacoustic signal

Figure 2.6 shows the amplitude of the photoacoustic signal as a function of the time for four different growing processes using the same experimental conditions. In Figure 2.6(a) the change in the amplitude signal labeled with the red circle represents the moment in which the electrolyte has been emptied in the cell. At this time the current source is still turned off. When there are no changes in the PA amplitude, the current source is turned on. As can be seen, an increase in the amplitude of the photoacoustic signal immediately appears. If the etching time increases, the photoacoustic signal becomes periodical (see Figure 2.6(b) to 2.6(d)). From this figure, it is possible to calculate the etching times. The thickness of the PS can be determined by using SEM images and by using the maximum and minimum conditions given by Eq. (2.9) it is possible to determine the real part of the refractive index at this wavelength.

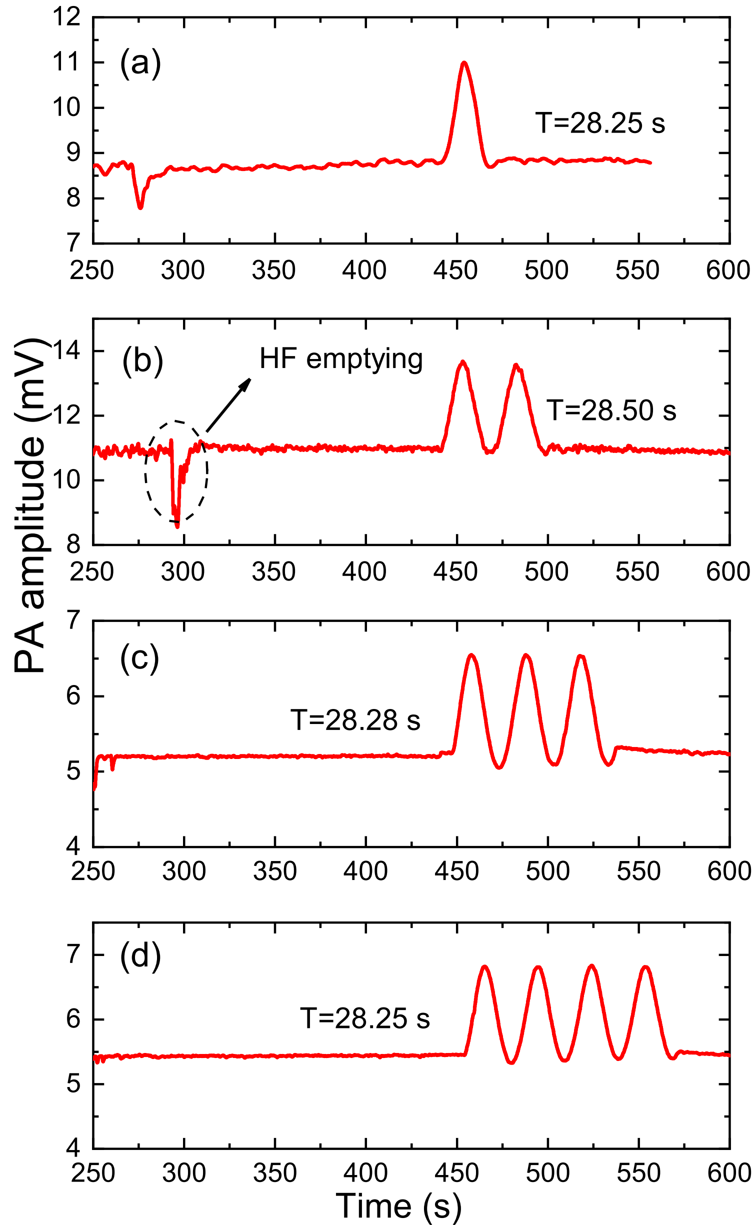

Figure 2.6: Photoacoustic signals for four different etching times at 20 mA current anodization. Each one of the etching processes was stopped at 1(a), 2(b), 3(c), and 4(c) photoacoustic cycles.

Taking into account the Eqs. (2.6) and (2.7), the change in the temperature of the sample is governed by the apparition of the porosity and changes in the thickness of the sample as shown in Eqs. (2.8) and (2.9). From a physics point of view, the reflectance during the etching process is periodic (see Figure 3 (a)). Therefore, the changes in the amplitude of

the photoacoustic signal are produced by the changes in the reflectance. Maximums in the reflectance correspond with a minimum in the photoacoustic signal, and minimums in the reflectance correspond with the maximum absorption of the radiation in the structure (PS/Si).

Here, it is imperative to clarify that the periodicity in the photoacoustic signal does not mean that the growing process is periodic. The PA signal is due to the light absorption and changes in the sample due to the modulation of the temperature. At this point, the chemical reaction is considered constant during the process.

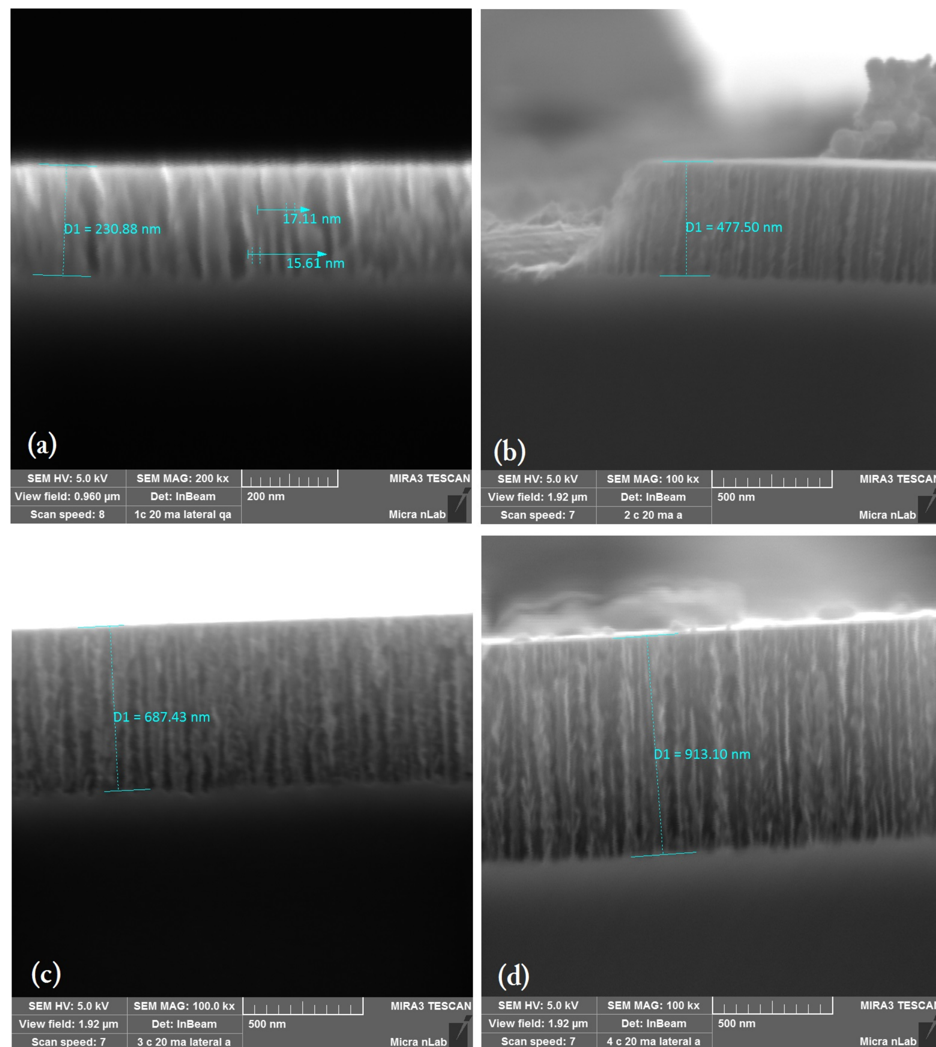

Figure 2.7: SEM images of cross sections of PS films growing for 1(a), 2(b), 3(c), and 4(d) photoacoustic cycles

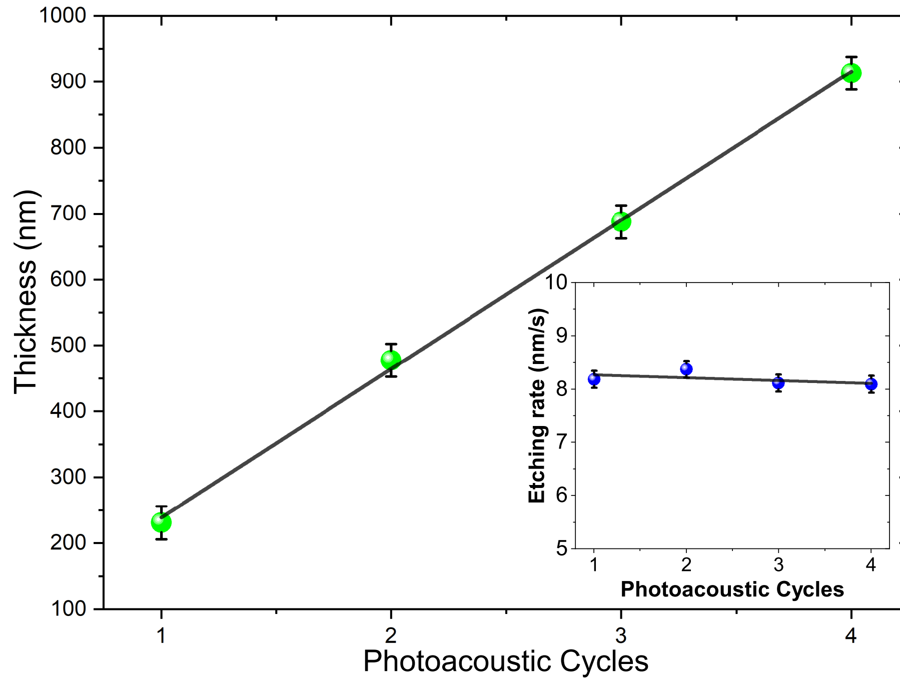

Figure 2.8: Relationship between photoacoustic cycles and the thickness of the sample. The inset shows that the etching rate for these anodization conditions is $8{,}3 \pm 0{,}1$ nm/s

To make a correlation between the photoacoustic signal for each period and the thickness of the samples, SEM images were obtained at the end of the 1st, 2nd, 3rd, and 4th photoacoustic periods. Figure 2.7 shows the cross sections of the PS films. As can be seen, the PS growing process produces nonregular Si columns in the range of 5 and 20 nm. The end of the pores are shown to be concave. From the data shown in Figure 2.6, is possible to determine the value of the period of the photoacoustic signal, and from Figure 2.7 it is possible to establish the average value of the sample thickness.

It is clear that a linear relationship exists between the thickness of the sample and the period of the photoacoustic signal (see Figure 2.8); by the obtainment of the time for each one of the periods and thickness of the sample, the etching rate can be determined. From the inset shown in Figure 2.8, the conclusion can be made that the etching rate is constant along the growing process, and that by using this methodology it is possible to obtain PS films with pre-established thickness values. Using the data obtained for the thickness of each sample, it was possible to obtain the value of the real part of the refractive index for the wavelength of the laser (λ_0 = 808 nm). Table 1 shows the computed values obtained

Table 2.1: Values of the real part of the refractive index and the etching rate for the films of PS obtained during 1, 2 , 3, and 4 photoacoustic cycles. The anodizing current was 20 mA and the ratio Ethanol/HF was 7:3 in volume.

PA cycles	λ_0 (nm)	Thickness (nm)[1].	$\mathrm{Re}(\eta\,(\lambda))$	Etching rate nm/s ±0,1
1	808	230.88	1.75	8.1
2	808	477.50	1.76	8.3
3	808	687.43	1.76	8.1
4	808	913.10	1.76	8.0

using the Eq. (2.9). According to this table, it shows clearly that if the sample is grown under the same experimental conditions, the photoacoustic methodology shown for all cases has the same period for the amplitude of the signal. This is an important fact because this method allows the obtainment of samples with the same optical properties. Samples with the same photoacoustic history should be samples with similar physical properties.

2.3.3. Photoacoustic signal wavelength dependence

Another experiment was carried out to prove that the periodic behaviors of the reflectance are correlated to the photoacoustic period. The reflectance is dependent on the wavelength of the incident radiation. For this reason, three samples were grown using the same anodizing conditions and power illumination, but now using three different wavelengths: 1024, 808, and 450 nm. Tsai *et al.* [75] studied the influence of the illumination during the etching process for p-type Si using a polychromatic light source center at 620 nm with different irradiation levels, they found that the power of illumination changes the size of the microstructure of PS. In our case, we do not have any dependence on this parameter. Analyzing the Eq. (2.9), the period of the photoacoustic signal must increase if the incident wavelength increases.

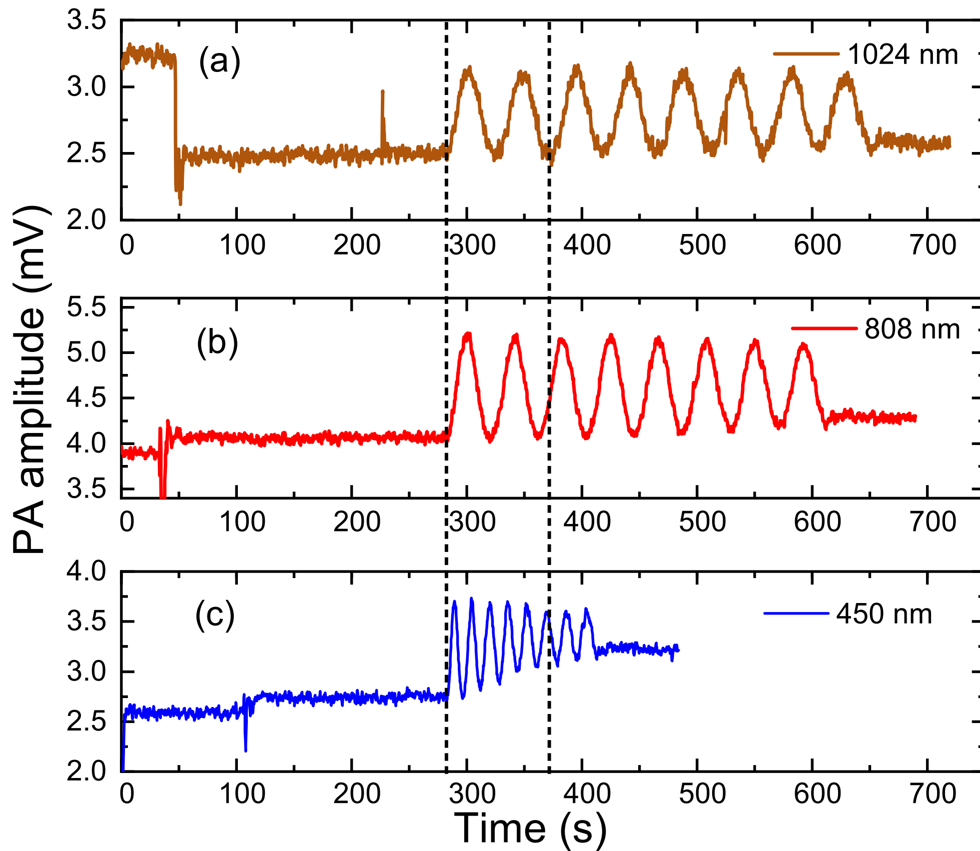

Figure 2.9: Photoacoustic signal wavelength dependence. Three different samples growth under the same anodizing condition but monitoring with lasers with different wavelengths.

Figure 2.9 (a) to (c) show the photoacoustic amplitude signal for three different wavelengths as a function of the time for eight photoacoustic cycles. It is clear that the value of the period in each case is different, and the experiment proved the correlation between the wavelength and the photoacoustic period proposed in the Eq. (2.9). This is a very important fact because the most precise determination of the sample thickness can be achieved using a laser with a shorter wavelength. In Figure 2.9(c) the attenuation of the PA amplitude signal is related to the increases in the absorption coefficient at this wavelength.

As a result of the design of the photoacoustic (PA) cell, it is required to reduce the noise (electronic, instrumental among others) by the construction of a differential PA cell that includes a reference signal in order to determine the instrumental function (transfer function)

to minimize noise.

It is clear that the AC component of the DC signal can be removed from the signal sample. However, other random fluctuations could appear in the sample signal. Any modulated signal can be described as a complex number, so two independents Lock-in amplifiers registers an amplitude and phase signal of the c-Si sample and the reference sample (aluminum foil), which mathematical representation the Eq. 2.10:

$$Z = R_j e^{i\theta_j} \tag{2.10}$$

Then, differential signal corresponds to:

$$R_D = \frac{R_s}{R_{ref}}, \tag{2.11}$$

$$\theta_D = \theta_s - \theta_{ref}, \tag{2.12}$$

where sub-indices *"s"* indicates the amplitude and phase of the c-Si sample and *"ref"* of the reference ones.

2.4. Modeling of the photoacoustic signal

After the implementation of differential PA cell the amplitude and phase signals for the PSi formation required a model that includes the sources that produce and affect the photoacoustic effect.

This section proposes a phenomenological model to reproduce the photoacoustic signal obtained during the porous silicon formation. It is introduced an extension of Rosencwaig and Gersho model to analyze the temporary changes that take place in the amplitude and phase of the photoacoustic signal during the PSi growth. It was solved the one-dimensional heat equation taking into account three thermal sources:

1. The laser modulated at ω_1.

2. The changes in the reflectance caused by the interference effect of the porous silicon thin film.

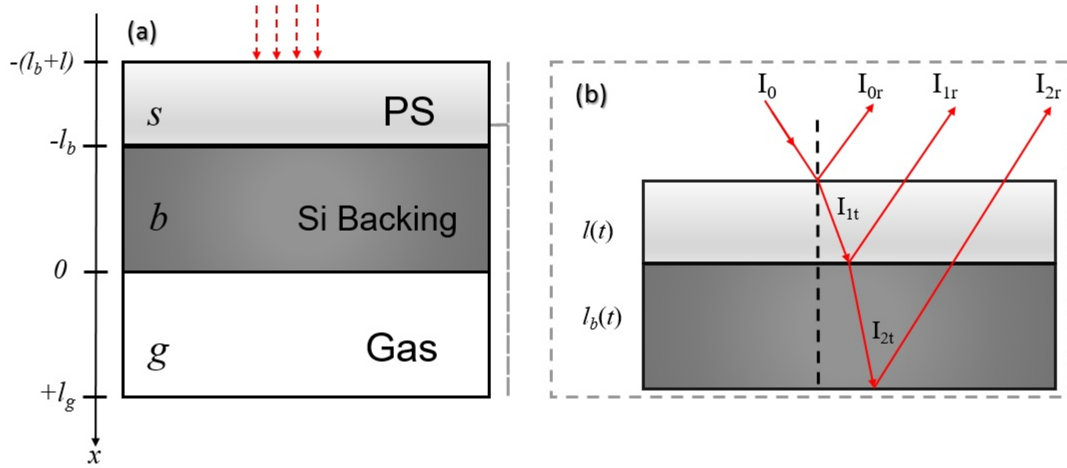

Figure 2.10: Cross-section of the photoacoustic cell. The labels s, b, and g correspond to sample, backing, and gas, respectively.

3. The AC components of the DC signal originated by electrochemical reaction and Joule effect.

In this experiment, the incident radiation is from the front, and the photoacoustic detection is located at the back of the Si sample as it is seen in Fig. 2.10(a). It is also considered a cylindrical photoacoustic cell with a cross-section geometry as it is shown in Fig. 2.10 (b). It is assumed that l, l_b, and l_g are the thickness of the sample (s), the backing material (b), and the gas column (g), respectively. The heat transfer is considered one-dimensional in the x-direction,[76] and the dilatation/contraction by the thermal effects is ignored. The electrochemical reaction causes the sample-backing boundary l_b to move in time. It is considered that v is the velocity of the PS formation which can be taken as a constant [21]. Thus, the moving boundary can be written as:

$$l_b(t) = l_b - vt, \tag{2.13}$$

giving as a result two scenarios: the first one is when the reaction has not consumed the backing and the second is when there is only PS. It implies that there is an interval of time $T = l_b/v$ where there are three regions (sample, backing, and gas) and for times $t > T$ there are only two parts (sample and gas). The thermal sources arise from the periodic excitation of the sample and the electrochemical etching in the sample-backing interface.

The sample heats the backing material which in turn modifies the temperature distribution of the surrounding gas where the microphone is fixed for the signal detection. Thus, the heat equation for the sample is:

$$\nabla^2 T_s(x,t) - \frac{1}{\alpha_s}\frac{\partial T_s(x,t)}{\partial t} = f_s(x,t) + Q(t,x), \tag{2.14}$$

where $f_s(x,t)$ and $Q(t,x)$ are the heat sources identified as the modulated laser and the electrochemical reaction respectively. The electrochemical reaction occurs only at the PS/Si interface.

In order to determine $f_s(x,t)$, it is assumed that a modulated light source impinges the surface at a frequency ω_1 with an intensity of I_0.The incident radiation (I_0) is in part reflected (I_{0r}) and transmitted (I_{1t}). At the interface sample-backing, the transmitted light is reflected (I_{1r}) to the sample and transmitted (I_{2t}) to the backing (Fig. 2.10(b)). The backing thickness changes as a function of time by the electrochemical etch. The reflected light appears with a different phase in relation to the incident light to satisfy the boundary conditions of the electromagnetic field. This effect can be represented by an additional light source with frequency ω_2 in the backing-sample direction. The superposition of these two effects allows to write $f_s(x,t)$ in the region $-(l+l_b) < x < -l_b + vt$ as:

$$\begin{aligned} f_s(x,t) = & - A(1+e^{i\omega_1 t})e^{-\beta_s(x+l_b+l)} \\ & - B(1+e^{i\omega_2 t})e^{\beta_s(x+l_b+vt)}, \end{aligned} \tag{2.15}$$

where:

$$A = \frac{\beta_s I_{1t}\eta_s}{2k_s} \text{ and } B = \frac{\beta_s I_{1r}\eta_s}{2k_s} \tag{2.16}$$

represent the heat density at $x = -(l+l_b)$ and $x = -l_b$, respectively, with η_i the efficiency in which the absorbed light is converted to heat by the nonradiative deexcitation processes [73]. Also, α_i represents the total thermal diffusivity, k_i is the total thermal conductivity, and β_i is the optical absorption coefficient for each material.

For the backing material in the region $-l_b + vt < x < 0$:

$$\nabla^2 T_b(x,t) - \frac{1}{\alpha_b}\frac{\partial T_b(x,t)}{\partial t} = f_b(x,t) \tag{2.17}$$

and its heat source term:

$$\begin{aligned} f_b(x,t) = & - C(1+e^{i\omega_1 t})e^{-\beta_b(x+l_b+vt)} \\ & - D(1+e^{i\omega_2 t})e^{\beta_b x}, \end{aligned} \tag{2.18}$$

where C and D M Eq. (2.16) with the respective index and intensities. The β_b [77]is 8,12$\times 10^2$ cm^{-1} and the thermal conductivity can take values between 1 to 1.3 W/K cm in this simulation (see Table 2.2). These intensities satisfy the system of equations given by:

$$\begin{aligned} I_{1t} + I_{r0} &= I_0 \\ I_{2t} + I_{1r} &= I_{1t} \\ I_{2t} + I_{2r} &= 1, \end{aligned} \tag{2.19}$$

where I_0 and I_{r0} can be extracted from the experiment. Finally, the heat equation for the gas is given by:

$$\nabla^2 T_g(x,t) - \frac{1}{\alpha_g}\frac{\partial T_g(x,t)}{\partial t} = 0. \tag{2.20}$$

To solve the Eqs. (2.14), (2.17), and (2.20) we use the superposition principle for each source of heat by an extension of the (RG) model.[73] The temperature field in the cell is given by:

$$T(x,t) = \mathrm{Re}\left\{\phi(x,t)\right\} + T_0, \tag{2.21}$$

where T_0 is the room temperature, this allows us to write the solution of ϕ_i for each region as:

$$\phi_g(x,t) = \tilde{\phi}_g(x,t) + \sum_{n=1}^{2} \theta_n \exp\left[-\sigma_g^n x + i\omega_n t\right], \tag{2.22}$$

$$\begin{aligned} \phi_b(x,t) &= \tilde{\phi}_b(x,t) \\ &+ \left[U_1 e^{-\sigma_b^1(v)(x+l_b+vt)} - V_1 e^{-\beta_b(x+l_b+vt)}\right] e^{i\omega_1 t} \\ &+ \left[U_2 e^{\sigma_b^2(0)x} - V_2 e^{\beta_b x}\right] e^{i\omega_2 t}, \end{aligned} \tag{2.23}$$

and

$$\begin{aligned} \phi_s(x,t) &= \phi_s^{\mathrm{DC}}(x,t) - \alpha_s \int_0^t Q(\tau)d\tau \\ &+ \left[W_1 e^{-\sigma_s^1(0)(x+l+l_b)} + W_2 e^{\sigma_s^1(0)(x+l+l_b)}\right. \\ &- \left. E_1 e^{-\beta_s(x+l+l_b)}\right] e^{i\omega_1 t} \\ &+ \left[W_3 e^{-\sigma_s^2(v)(x+l_b+vt)} + W_4 e^{\sigma_s^2(v)(x+l_b+vt)}\right. \\ &- \left. E_2 e^{\beta_s(x+l_b+vt)}\right] e^{i\omega_2 t}, \end{aligned} \tag{2.24}$$

in which we have defined:

$$\begin{aligned}\tilde{\phi}_i(x,t) &= \text{DC component of the PA signal} \\ &+ \text{Etch heating contribution} \\ &+ \text{Joule effect from the current source} \\ &\equiv \Delta P_{\mathrm{DC}} + \mathrm{Etch}, \end{aligned} \tag{2.25}$$

where the contributions from the etching heat and the the Joule effect have been included with the label Etch. The coefficients W_n and U_n are obtained from the temperature and the flux continuity for each AC component of Eqs. (2.22)-(2.24). It is easy to show that σ's are related to the thermal diffusivity α as follows:

$$\begin{aligned}\sigma_g^n &= (1+i)\sqrt{\frac{\omega_n}{2\alpha_g}} \\ \sigma_j^n(v) &= \frac{1}{2}\left(\frac{v}{2} + \frac{\sqrt{v^2 + 4i\alpha_j\omega_n}}{\alpha_j}\right), \quad j = b, s. \end{aligned} \tag{2.26}$$

The constants V_n and E_n are determined by using Eqs. (2.23) and (2.24) in Eqs. (2.17) and (2.14), which give us:

$$V_1 = \frac{C}{\beta_b^2 + \frac{\beta_b v - i\omega_1}{\alpha_b}}, \quad V_2 = \frac{D}{\beta_b^2 - \frac{i\omega_2}{\alpha_b}} \tag{2.27}$$

and

$$E_1 = \frac{A}{\beta_s^2 - \frac{i\omega_1}{\alpha_s}}, \quad E_2 = \frac{B}{\beta_s^2 + \frac{\beta_s v - i\omega_2}{\alpha_s}} \tag{2.28}$$

The temperature and flux continuity conditions at the sample surfaces are explicitly given by:

$$\begin{aligned}\phi_g(0,t) &= \phi_b(0,t) \\ \phi_b(-l_b + vt, t) &= \phi_s(-l_b + vt, t) \\ k_g \frac{\partial \phi_g}{\partial x}(0,t) &= k_b \frac{\partial \phi_b}{\partial x}(0,t) \\ k_b \frac{\partial \phi_b}{\partial x}(-l_b + vt, t) &= k_s \frac{\partial \phi_s}{\partial x}(-l_b + vt, t), \end{aligned} \tag{2.29}$$

which we apply separately to each source and to their AC and DC components. Our attention is focused on θ_n, the complex amplitude of the periodic temperature at $x = 0$, which

give us the source of photoacoustic signal. By using the Eqs. (2.29), these amplitudes are:

$$\begin{aligned}\theta_1 &= \frac{k_b(\beta_b - \sigma_b^1(v))}{k_b\sigma_b^1(v) - k_g\sigma_g^1} V_1 e^{-\beta_b(l_b - vt)},\\ \theta_2 &= \frac{k_b(\beta_b - \sigma_b^2(0))}{k_b\sigma_b^2(0) + k_g\sigma_g^2} V_2.\end{aligned} \tag{2.30}$$

The periodic excitation of the backing-gas boundary expands the gas column and contract at the same frequency of the oscillations of the temperature field. The PA amplitude signal is time dependent; therefore, it is convenient to define the average temperature of the gas. From the functional form of the temperature field, there is a characteristic length λ_g in which the periodic temperature variation in the gas is completely damped out. As a result, the gas average temperature is defined as:

$$\bar{\phi}(t) \equiv \frac{1}{\lambda_g}\int_0^{\lambda_g} dx\ \phi_{AC}(x,t), \tag{2.31}$$

from Eq. (2.22) this gives:

$$\begin{aligned}\bar{\phi}(t) &= \sum_{n=1}^{2} \frac{\theta_n}{2}\sqrt{\frac{2\alpha_g}{\omega_n}}(1-i)\left(1 - e^{-\sigma_g^n \lambda_g}\right) e^{i\omega_n t}\\ &\approx \sum_{n=1}^{2} \sqrt{\frac{\alpha_g}{\omega_n}}\theta_n e^{i(\omega_n t - \pi/4)}.\end{aligned} \tag{2.32}$$

By using the ideal gas law, the displacement $\delta x(t)$ of a column of gas is given by:

$$\delta x(t) = \lambda_g \sum_{n=1}^{2} \sqrt{\frac{\alpha_g}{\omega_n}}\frac{\theta_n}{\Phi} e^{i(\omega_n t - \pi/4)}, \tag{2.33}$$

where we have set the average DC temperature of the gas boundary layer equal to the DC temperature at the solid surface:

$$\Phi = \theta_0 + T_0. \tag{2.34}$$

The pressure at time t can be derived if it is assumed that the gas is compressed adiabatically. From the adiabatic gas law and along with Eq. (2.33) is obtained:

$$\begin{aligned}\delta P(t) &= \gamma\frac{P_0}{V_0}\delta V(t)\\ &= \gamma P_0 \frac{\lambda_g}{l_g} \sum_{n=1}^{2} \sqrt{\frac{\alpha_g}{\omega_n}}\frac{\theta_n}{\Phi} e^{i(\omega_n t - \pi/4)},\end{aligned} \tag{2.35}$$

where γ is the adiabatic index. Finally, $\Delta P(t)$ is modeled by using the Eq. 2.36 and detected by the microphone at x_{mic} and converted in the photoacoustic signal.

$$\Delta P(t) = \Re\{\delta P(t)\}. \tag{2.36}$$

2.4.1. PA amplitude fitting

The laser wavelength used in this experiment was 808 nm which is super-band gap for Si (1.12 eV) and sub band gap for PS that is typically about 2.2 eV -3.2 eV depending on its porosity [78]. The etching conditions were 7:3 V/V ethanol/HF ratio, and 20 mA/cm^2 current density.

The PA amplitude signal was divided into four regions (See Fig. 2.11). Region (a) in which the Si sample is directly impinged by the laser, the part (b) is characterized by a drastic change in the PA signal which is related to the emptying of the electrolyte into the chamber. A pause takes place while the native surface of silicon oxide reacts with the HF and it is removed from the surface. At this stage, the power supply is still off. In the region (c) the power supply is turned on and the PS formation takes place. This region is characterized by the oscillatory shape of the PA signal. Finally, for the region (d) the power supply is still turned on, but the coherent interference effect is lost due to the thick film [74, 79] of PS. The inset in Fig. 2.11 is the total contribution to the PA signal from the non-radiative process as a function of the etching time. The way in which this curve was obtained is explained in Sec. IV. It is suggested the Ref. [21] for a more detailed description of the electrochemical PA experimental setup.

The modified RG model for the PA signal takes into account the above-mentioned thermal sources. By using experimental values of the PA cell size, the modulated frequency, the thermal properties of the sample and gas, and the sample size, it is possible to calculate the AC component of the PA amplitude signal during PS growing (Eq. 2.34). Table 2.2 shows the experimentally reported values for the electronic and thermal parameters for p and n Si. The velocity of the chemical reaction is involved in the PA amplitude signal, such is analyzed in detail in the next section.

Table 2.2: Reported values for the thermal and electric properties of Si at different doped levels.

Type	Dopant concentration cm^{-3}	Resistivity (300K) Ω cm	Thermal conductivity W K^{-1} cm^{-1}	Thermal diffusivity cm^2 s^{-1}	$D_{n,p}$ cm^2s^{-1}	τ μs	Ref
n	10^{15}	0.025	-	0,795	-	-	[80]
n	5×10^5	1	-	0.797	-	-	[80]
n	$1{,}5 \times 10^{14}$	25	-	0.821	-	-	[80]
n	$5{,}7 \times 10^{13}$	75	-	0.868	-	-	[80]
n	10^{12}	4000	-	0.985	-	-	[80]
p	–	14-24	-	0.80	30	10.5	[81]
p	–	14-24	-	0.75	5.5	95	[39]
p	–	25-44	-	0.96	3.1	1400	[39]
p	$1{,}5 \times 10^{14}$	88.9	-	0.76	5	100	[82]
p	1×10^{16}	0.52	1.48	-	-	-	[83]
p	2×10^{19}	0.005	1.22	-	-	-	[83]

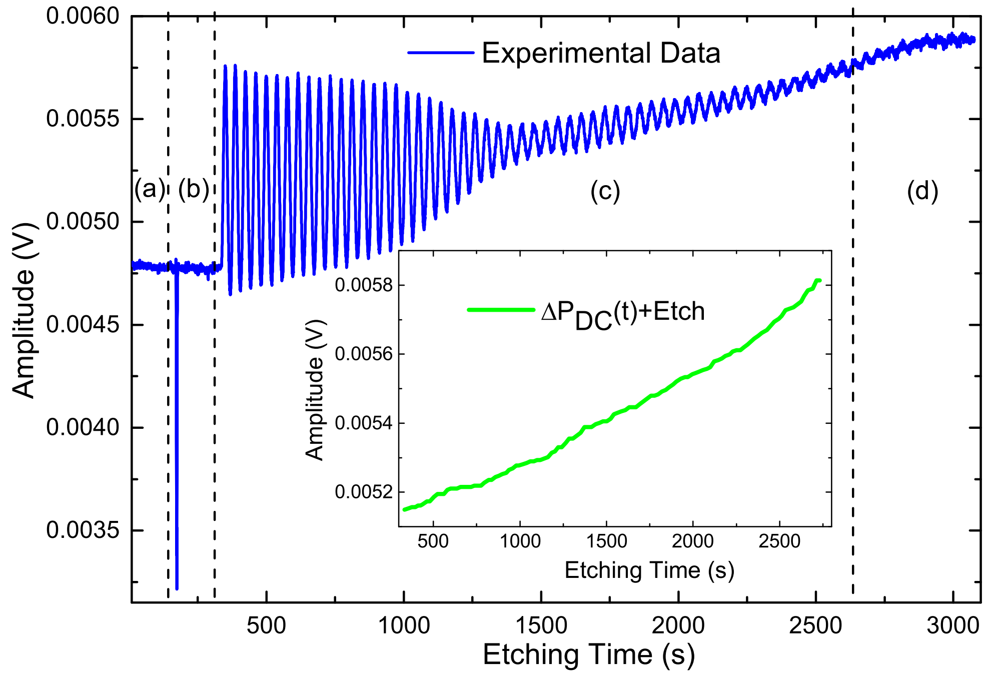

Figure 2.11: (Color line) The experimental data of the PA signal as a function of the etching time (blue). The inset shows the contribution from the DC component extracted from the experimental data (green).

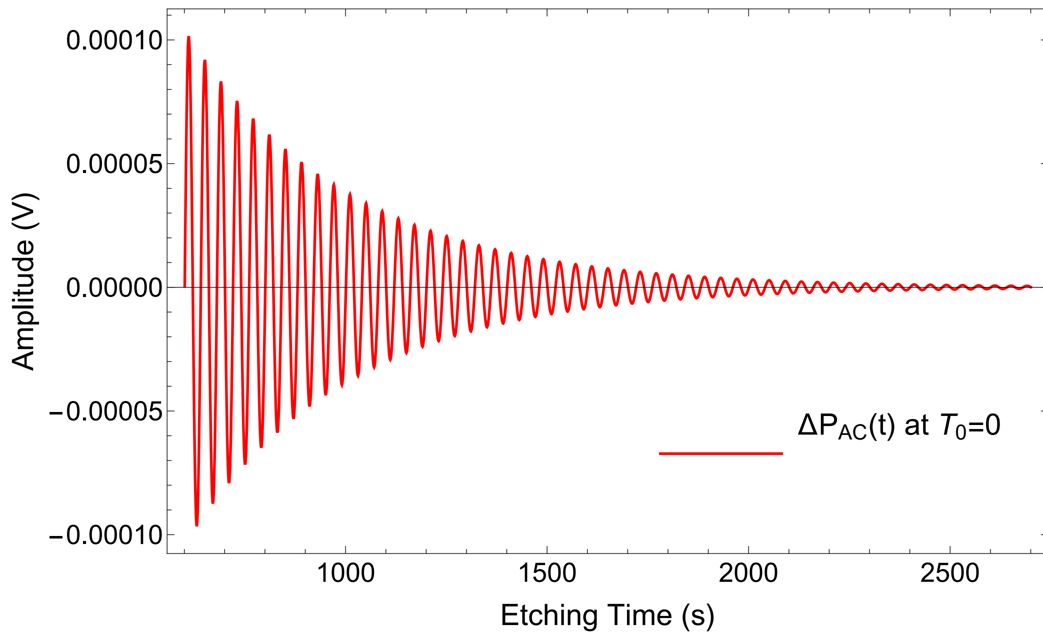

Figure 2.12: AC-photoacoustic signal computed from Eq. (2.36), at $T_0 = 0$, in the interval of etching $450 < t < 2700$. It is observed that the modulation comes from the frequency ω_2, i. e., the effect of reflectance in the PS which is related to a period $T \sim 40$s.

Table 2.3: Values for the relevant parameters used in Eq. (2.36) in order to reproduce Fig. 2.12.

C	2×10^6	$\mathrm{K/m^2}$
D	2×10^6	$\mathrm{K/m^2}$
ω_1	$26\ \pi$	rad/s
ω_2	$5 \times 10^{-2}\pi$	rad/s
α_g[84]	0.20	$\mathrm{cm^2/s}$
κ_g[84]	$2{,}53 \times 10^{-4}$	W/(cmK)
β_b(808 nm)	$8{,}12 \times 10^2$	$\mathrm{cm^{-1}}$
β_s(808 nm)	$2{,}20 \times 10^2$	$\mathrm{cm^{-1}}$
l_b	500×10^{-6}	m
x_{mic}	2×10^{-6}	m
v	8	nm/s

Fig. 2.12 shows the AC component of the PA amplitude signal calculated from Eq. (2.36) as a function of the etching time at $T_0 = 0$. This simulation includes the values shown in Tables 2.2 and 2.3. The frequency of this signal is constant in time. That means that one of the real parts of the amplitudes in Eq. (2.30) predominates in the heat transfer. Also, the amplitude of this signal is modulated and it is related to the increase in the optical path of the transmitted light mainly in the PS layer. The baseline in Fig. 2.12 is centered at zero, given that the modulated source does not produce an average heating of the sample since there are continuous excitation/deexcitation processes.

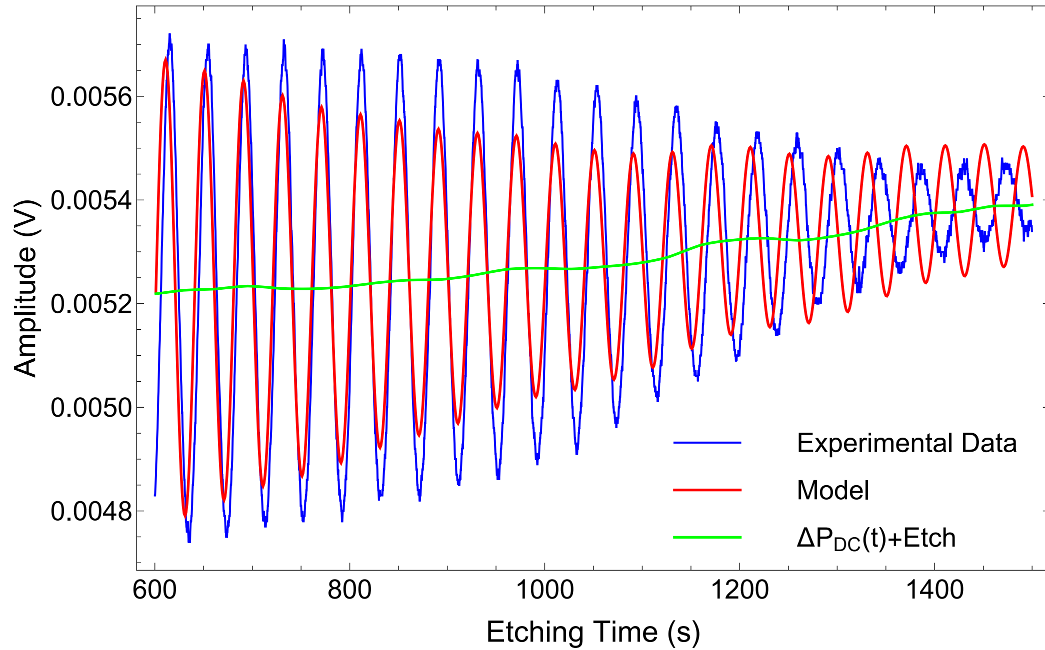

Figure 2.13: Photoacoustic signal of experimental data (blue) and phenomenological model (red). Also the contribution of etching and DC component is shown (green) for the etching time 450 s $< t <$ 1500 s.

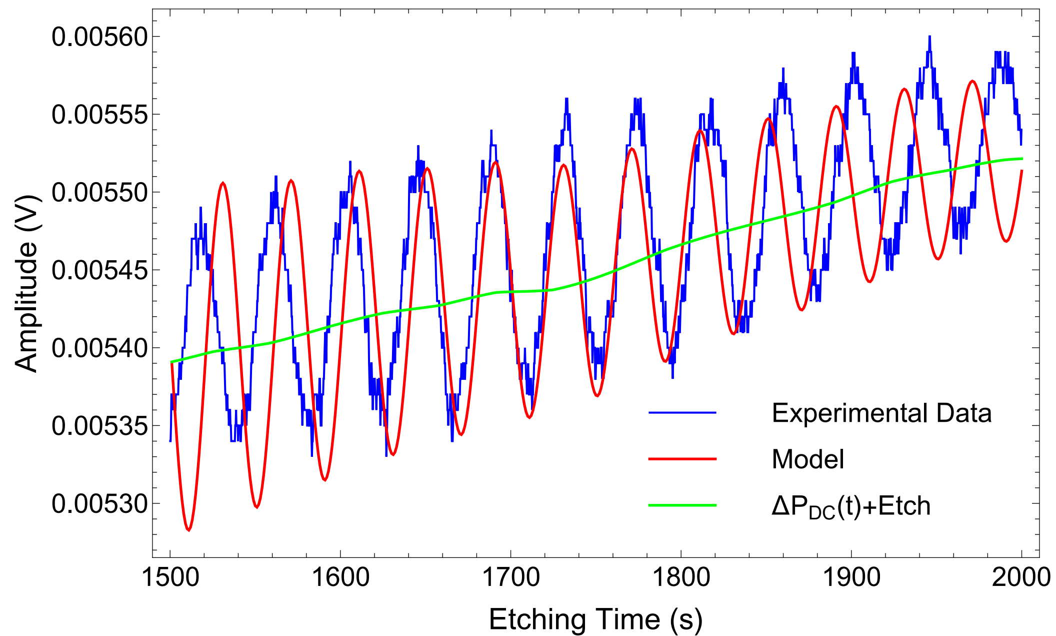

Figure 2.14: Photoacoustic signal of experimental data (blue) and phenomenological model (red). Also the contribution of etch and DC component is shown (green) for the etching time 1500 s $< t <$ 2000 s.

Comparing Figs. 2.11 and 2.12, it can be seen that the predominant amplitude in this signal comes from θ_2 (Eq. 20) given that the AC-PA cycles correspond to the frequency ω_2 in accordance with the experimental data in which a complete cycle approximates $t_{\text{etching}} \sim 40$ s.

It is necessary to take into account that the etching process also contributes to the PA signal as well as the DC component of the process (thermal inertia) which can be obtained from the experimental data using different criteria, such as: the minimum, the maximum, or the average of the PA amplitude signal of the characteristic growing process as a function of the etching time. In this case, the average criterion was used. It is important to note that this average temperature is the contribution of the DC and the etching heating. The inset in Fig. 2.11 shows the average temperature for the etching process in which it is noticeable that the temperature of the PA chamber increases. The changes in the pressure can be written as follows:

$$\Delta P = \Delta P_{\text{AC}} + \Delta P_{\text{DC}} + \text{Etch}. \quad (2.37)$$

Figs. 2.13 and 2.14 exhibit a comparison between the experimental data (blue line) for 64 PA cycles and the theoretical results for the amplitude obtained using the Eq. (2.36) and the values from Tables 2.2 and 2.3 (red line), as well as the DC contribution coming from the chemical reaction (green line). It can be noticed that there are regions where the theoretical prediction does not fit the experimental data. It is taken into account that the velocity of the PS for growing with four PA cycles was determined earlier[21], indicating that the velocity of the etching is constant almost for a few cycles. The shift in some intervals of etching time evidence changes in the velocity of the PS formation. This behaviour can be associated with the spatial distribution of the impurities[39] and the variations in the crystalline quality of the Si wafer.[71].

Figs. 2.15 and 2.16 show a more detailed fit of the experimental data. For the simulations, the plot was divided into several regions, each one with its own parameter of etching velocity v_i and frequency ω_{2i} in order to test the model when these variables were changed. The values of the parameters used are shown in Table 2.3. It can be seen that at the beginning of the etching process the velocity of the PS growing is constant. As time passes, the etching velocity increases until a certain point in which v decreases. This behaviour can be attributed to the depletion of the electrolyte. The results of the simulations show that

a change in the etching velocity implies a change in the frequency ω_2, and proves that the model allows the determination of these parameters which are the most important information of the PA signal at any time interval of interest.

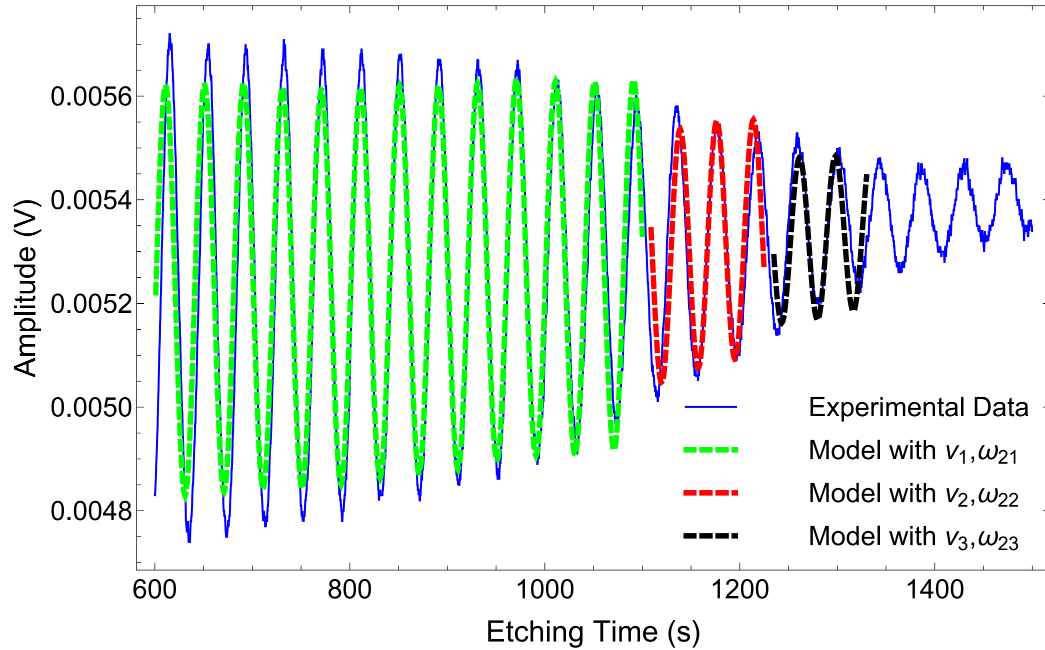

Figure 2.15: Photoacoustic signal of experimental data (blue) and phenomenological model, for different values of ω_2 and v. The fit has been done with the values $\omega_{21} = \pi/20 \approx 0{,}157$ rad/s, $v_1 = 8$ nm/s (green), $\omega_{22} = 0{,}167$ rad/s, $v_2 = 44$ nm/s (red), and $\omega_{23} = 0{,}170$ rad/s, $v_3 = 60$ nm/s (black).

From a physical point of view, the model reproduces the phenomenology of experimental the PA signal and predicts that the changes in the reflectance have a frequency characteristic (ω_2) that governs the PA amplitude in some interval of the etching time. An envelope function decays like exponential in accordance with the Lambert-Beer law. It gives information about the PS thickness, and the increases of the DC level is related to thermal inertia (Electrochemical etch + Joule Effect). Also, the thermal properties of the structure determined the behaviour of this envelope (see Eq. 2.30).

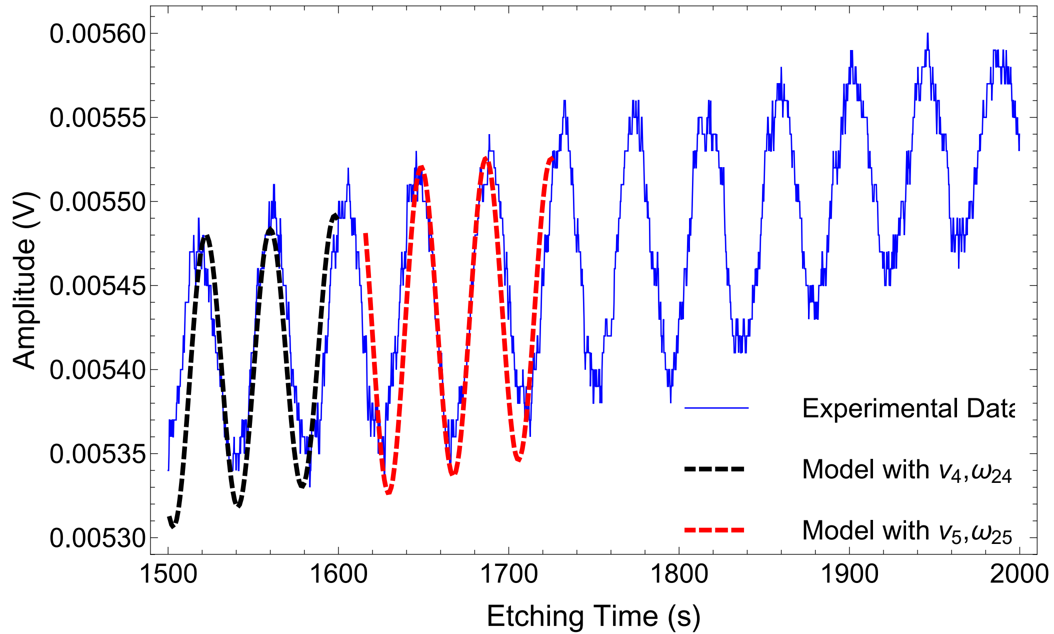

Figure 2.16: Photoacoustic signal of experimental data (blue) and phenomenological model, for different values of ω_2 and v. The fit has been done with the values $\omega_{24} = 0{,}166$ rad/s, $v_1 = 50$ nm/s (black), and $\omega_{25} = 0{,}165$ rad/s, $v_2 = 43$ nm/s (red) .

In this case, the different frequencies (ω_2) for the simulation were taken from the experimental data, to appreciate the accuracy of the model. The theoretical results exhibit an excellent comparison match with the experiment data. The reproduction of these cycles using our model is the most relevant information, for there is a direct relationship between the cycles and the velocity of the PS formation.

In summary, the photoacoustic signal of the porous silicon formation has been studied by solving a one-dimensional heat equation with an extension of the RG model. This modification takes into account three thermal sources: laser, reflectance changes, and electrochemical reaction (etching process and Joule effect). The model reproduces in detail the growing conditions of PS. The frequency of the reflectance changes governs the PA signal; therefore, using this model, it is possible to determine the velocity of the etching process. Finally, from the inset in Fig. 2.11 the electrochemical reaction is continuous, and the increment of the PA amplitude can be considered as an exothermic reaction.

CHAPTER 3

Optical properties of porous silicon

3.1. PSi optical constants determination

The calculation of the optical constants (refractive index $n(\lambda)$, and extinction coefficient, $k(\lambda)$) is usually made by fitting the reflectance or transmittance spectra. However, the methods are not trivial, in fact, they represent an inverse problem. This problem of estimating optical constants and thickness using only transmittance or reflectance data has been addressed by using fitting procedures and optimization algorithms. However, in the case of PSi, due to the nature of the random porous formation, it is necessary to consider other parameters such as porosity and interface roughness because this variety of inhomogeneities causes light scattering. These inhomogeneities and roughness are no longer negligible, and they can introduce a significant error in the determination of the optical constants [85].
Optimization algorithms solve this kind of problems, especially evolutionary algorithms because they can avoid local minima following many search pats simultaneously [86, 87, 88, 89]. Torres-Acosta et al. [86] used a self-adaptive genetic algorithm (GA) to determine optical constants and thickness of PSi films in the visible range (400-800 nm). However, the fitting procedure used a parametrization of the real part of the refractive index, and it did not consider the porosity and roughness of the PSi film because the experimental setup includes an integrating sphere. On the other hand, Peña and Torres [90] propose to determine

the optical constants of PSi films using diffuse and specular reflectance simultaneously. The comparison between the scattering and specular spectrum allows an estimation of film roughness. However, this methodology fails in the ultraviolet region due to the difficulty to extrapolate the refractive index and the high absorption contribution in this region. Nevertheless, it is possible to use the same methodologies to introduce the porosity and interface roughness, and fit the specular reflectance spectrum to determine the thickness, optical constants, porosity, and interfacial roughness simultaneously.
To add the porosity percentage and roughness interface, the electrical permittivity of PSi can be described as an effective medium. This method takes into account the system as a mixture composed by a host medium with $\hat{\epsilon}_m$ (c-Si) with inclusions within it, characterized by $\hat{\epsilon}_i$, which allows the determination of the optical properties in the linear regimen. Thus, the PSi is modeled as an effective medium [2] that is the result of a mixture of c-Si and the material that fill the pores that can be a gas or liquid.
To overcome this problem, this work proposes a methodology based on genetic algorithms to fit the near-specular reflectance (6° incidence) spectrum of single films of PSi over the c-Si substrate. A simultaneous determination of PSi properties such as optical constants, thickness, porosity, and interface roughness is made only by using reflectance measures. The system is considered as a silicon (c-Si) single crystal, and by using an effective medium approximation (EMA) the algorithm can determine the refractive index $\eta(\lambda)$, extinction coefficient $\kappa(\lambda)$, PSi thickness, interfaces RMS roughness (σ) (Air/PSi and PSi/Si substrate) and the porosity. The model is tested by using several films of p-type Si fabricated with different anodizing times. Also, the thickness of the PSi samples was determined by the genetic fit and compared with the thickness obtained by electron scanning microscopy (SEM) images.

3.1.1. Thin-film calculations

The method of the optical admittance is valid in the case of a linear regimen, that is very convenient because of the optical constants, or the complex refractive index ($\hat{N} = \eta + i\kappa$),

can be expressed regarding dielectric constant of the medium ($\hat{\varepsilon} = \varepsilon_1 + i\varepsilon_2$) as follows:

$$\mathrm{Re}(\hat{N}) = \eta = \sqrt{\frac{|\hat{\varepsilon}| + \varepsilon_1}{2}},$$
$$\mathrm{Im}(\hat{N}) = \kappa = \sqrt{\frac{|\hat{\varepsilon}| - \varepsilon_1}{2}}. \tag{3.1}$$

The Eqs. 3.1 are useful because the dielectric constant of two-component materials (host and filling material) can be expressed through the effective medium approximation (EMA)[2, 1], where the volume fraction of the filling material is directly related with the porosity. For these simulations, it was proved the Maxwell-Garnett, Bruggeman, and Looyenga EMA formulas. However, due to the porous morphology, it is recommended to use Looyenga EMA formula (Eq. 3.2) [1], because it does not consider a regular geometry of the incrustations.

$$\hat{\epsilon}_{eff}^{1/3} = \hat{\epsilon}_{Si}^{1/3} + p\left(\hat{\epsilon}_{air}^{1/3} - \hat{\epsilon}_{Si}^{1/3}\right) \tag{3.2}$$

To determine the reflectance of multilayers systems, the optical admittance method [74, 79] introduces the transfer matrix $\mathbf{S}$ of the complete system through the multiplication of the refractive matrix $\mathbf{W}_{i-1,i}$ of each interface and phase matrix $\mathbf{U}_i$ of each single film, where their components are expressed regarding the Fresnel coefficients. This notation indicates that i-th interface is the i-th material to the right of the interface and it is numbered as is shown in Fig. 3.1.

$$\mathbf{W}_{i-1,i} = \frac{c_{i-1,i}}{t_{Ri}}\begin{pmatrix} 1 & -r_{Li} \\ r_{Ri} & t_{Ri}t_{Li} - r_{Ri}r_{Li} \end{pmatrix}, \tag{3.3}$$

where ${r_{Ri,Li}}^{(0)}$ and ${t_{Ri,Li}}^{(0)}$ are the usual Fresnel coefficients defined for optical admittance [74, 79] of the i-th interface. The coefficients written in the form showed in the Eq. 3.4 introduce the RMS roughness (σ_i) of the i-th interface.

$$\begin{aligned}
r_{Ri} &= r_{Ri}^{(0)}\exp\left[-2(2\pi\sigma_i\eta_{i-1}/\lambda)^2\right] = \alpha r_{Ri}^{(0)}, \\
r_{Li} &= r_{Li}^{(0)}\exp\left[-2(2\pi\sigma_i\eta_i/\lambda)^2\right] = \beta r_{Li}^{(0)}, \\
t_{Ri} &= t_{Ri}^{(0)}\exp\left[-1/2(2\pi\sigma_i/\lambda)^2(\eta_i - \eta_{i-1})^2\right] = \gamma t_{Ri}^{(0)}, \\
t_{Li} &= t_{Li}^{(0)}\exp\left[-1/2(2\pi\sigma_i/\lambda)^2(\eta_{i-1} - \eta_i)^2\right] = \gamma t_{Li}^{(0)}.
\end{aligned} \tag{3.4}$$

The $c_{i-1,i}$ parameter is related with the light polarization given by

$$c_{i-1,i} = \begin{cases} \cos\theta_{i-1}/\cos\theta_i & \text{for p-polarization} \\ 1 & \text{for s-polarization} \end{cases}. \tag{3.5}$$

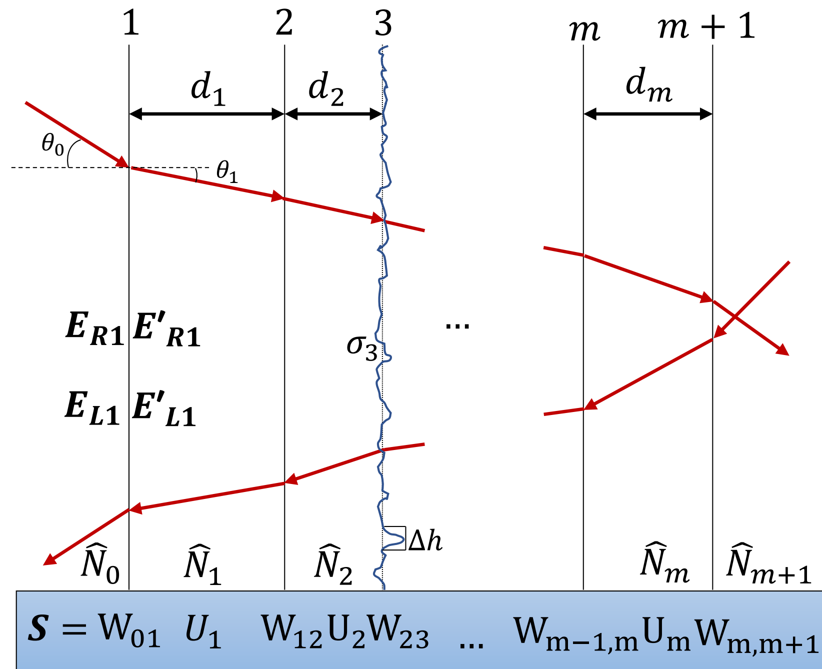

Figure 3.1: Multilayer structure form with $m+1$ interfaces. This scheme shows the field amplitudes of the moving waves from left to right. Parameter σ_3 represents the RMS roughness of the third interface and Δh the size of the irregularities in nanometers. It is assumed that $\Delta h << \lambda$.

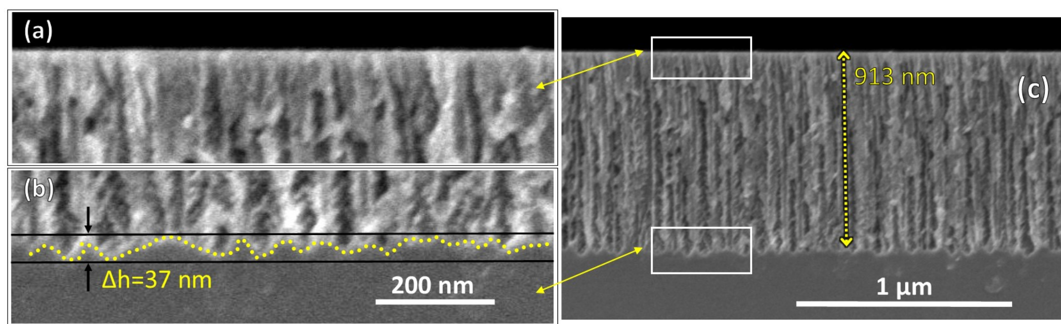

Figure 3.2: SEM image of sample fabricated under the same condition of sample S4. (a) Shows a closer zoom of the interface Air/Psi, (b) shows a closer look of the interface PSi/Si and it is highlighted the rough interface, and (c) shows the complete cross section of the PSi sample.

The phase matrix is defined by Eq. 3.6, where $\hat{N}_i$ is the complex refraction index and d_i is the medium thickness.

$$\mathbf{U}_i = \begin{pmatrix} \exp\left(i\frac{2\pi}{\lambda}\hat{N}_i d_i\right) & 0 \\ 0 & \exp\left(-i\frac{2\pi}{\lambda}\hat{N}_i d_i\right) \end{pmatrix}. \tag{3.6}$$

Finally, the transfer matrix of the multilayer structure is defined as

$$\mathbf{S} = \mathbf{W}_{01}\mathbf{U}_1\mathbf{W}_{12}\mathbf{U}_2...\mathbf{W}_{m,m+1} = \begin{pmatrix} s_{11} & s_{12} \\ s_{21} & s_{22} \end{pmatrix}, \tag{3.7}$$

and the reflectance and transmittance are determined by

$$\begin{aligned} R = |r_R|^2 &= \left|\frac{s_{21}}{s_{11}}\right|^2, \\ T = |t_R|^2 &= \left|\frac{1}{s_{11}}\right|^2. \end{aligned} \tag{3.8}$$

This method permits to calculate the total response of multilayer systems based on porous silicon (PSi) such as distributed Bragg reflector (DBR)[91] or resonator cavities.

3.1.2. Genetic fit

The genetic algorithm used in this work is useful to determine the optical constants, porosity, roughness, and thickness of PSi by using its reflectance spectrum and an effective medium approximation [2, 1]. In the case of absolute reflectance of thin films stacks, the optical response is dependent on several optical and structural parameters. Here, each parameter will be a gene, and the complete array of these genes is the chromosome ($\mathbf{V}$) that is defined as follows:

$$\mathbf{V} = (v_1, v_2, v_3, v_4) = (p, d, \sigma_0, \sigma_1), \tag{3.9}$$

where p is the porosity, d the PSi thickness, σ_0 the roughness in the interface air/PSi, and σ_1 the roughness in the interface PSi/Si. The parameters defined in the chromosome are used to calculate the theoretical reflectance spectrum ($R_G(\lambda)$), and it is compared with the experimental ($R_{exp}(\lambda)$) through the penalty function (Eq. 3.10). $R_{exp}(\lambda)$ is the absolute reflectance of PSi/Si structure obtained by using Eq. 2.1. Thus, the method to estimate the

parameters related in the chromosome (Eq. 3.9) is a problem of least squares fitted between as a measured and theoretical reflectance.

$$F(\mathbf{V}) = \sum_{i=1}^{N} \left[R_{exp}(\lambda_i) - R_G(\lambda_i, p, d, \sigma_0, \sigma_1)\right]^2 . \tag{3.10}$$

The values of some genes are constraints [87, 88] in order to guarantee values with physical sense. Indeed, the initial population and the next generations have to satisfy the condition of the Eq. 3.11.

$$\begin{aligned} 0 < p < 1 \text{ for all } \lambda \, \epsilon \, [\lambda_{min}, \lambda_{max}] \, , \\ \sigma_i < 100 \text{ nm for all } \lambda \, \epsilon \, [\lambda_{min}, \lambda_{max}] \, , \end{aligned} \tag{3.11}$$

The genetic algorithm used for this calculations is described in the next steps and it is based on the works of references [86, 87, 88].

1. **Population**: a number of J_{P_0} individuals (chromosomes) are created by choosing a random value for every single gen. The values of genes have to satisfy the constrain conditions (Eq. 3.11).

2. **Reproduction**: each individual V_{father} has given a number K_{off} offspring. For that, another individual of the same generation called V_{mother} is select randomly. The offspring is given by two reproduction ways determined with ρ probability.

$$v_i^{son} = \begin{cases} v_i^{(father)} \text{ if } r < \rho_1 \\ v_i^{(mother)} \text{ if } r \geqslant \rho_1, \end{cases} \tag{3.12}$$

$$v_i^{son} = \frac{v_i^{(father)} + v_i^{(mother)}}{2}, \tag{3.13}$$

where ρ_1 is the probability of inheriting the father's gene and r is a random number used to decide it.

3. **Mutation**: a certain number of individuals are mutated to introduce new genes in order to avoid local minima. The mutation is generated in the chromosome as following:

$$\tilde{v}_i^{son} = v_i^{son} \left(1 + \mathcal{N}_{(0,1)} \tau\right) , \tag{3.14}$$

where τ is a weight function parameter and $\mathcal{N}_{(0,1)}$ is a random value from a normal distribution.

4. **Family competition**: every chromosome is used to simulated the reflectance spectrum by using the Looyenga EMA rule (Eq. 3.2) and the optical admittance method (Eqs. 3.7 and 3.8). The penalty function (Eq. 3.10) is evaluated for each individual. After, the family competition starts. The individual who has the best fit is the best adapted, it survives to the next generation and becomes a new father. If the new generation gives back a better fit, the mutation value τ is reduced by a factor f. Finally, the steps mentioned above are repeated a J_{G_0} times. The value J_{G_0} is the number of generations, and the individual with the lower value of penalty function represent the bets adapted and is the solution to the problem.

Using the genetic fit, some results from the analysis of measured reflection signals are presented. For all simulations, a $J_{P_0} = 50$ individuals were used for each generation with $K_{off} = 15$ offsprings during $J_{G_0} = 100$ generations. The parameters obtained were the films thickness, porosity, interface roughness, and etch rate. Further, a comparison between thickness obtained by a genetic fit and by SEM is given. Fig. 3.3 shows the experimental and the best fit of the reflectance spectrum for each sample, and table 3.1 shows the value of the fitting parameters obtained. In all samples, the current density during the anodizing was 20 mA/cm^2. It means, due to the self-limited character of the reaction [92, 93] the porosity must remain constant for short anodizing times. This fact can be noted in the value of the porosity in table 3.1. As it was reported elsewhere, the etch rate is almost constant [63, 21]. Therefore, it is expected that the thickness of the samples S2, S3, and S4 are closely an integer multiple value of the thickness of sample S1. As it can be seen, the thickness obtained by genetic fit is close to the obtained value by SEM. However, in all cases, the genetic fit reports lower values than SEM. Even so, the obtained values for genetic fit are in the uncertainty range of the SEM technique, that for this case is ± 10 nm.
The main effect of the interface roughness is the loss of reflected intensity due to the scattering. Also, the branching of the porous can contribute to the scattering. This effect can be appreciated in Fig.3.3 where the genetic fit it was run without roughness correction (blue dash line). It is clear that the best fit has always a higher intensity than the measured reflectance because the scattering is neglected.

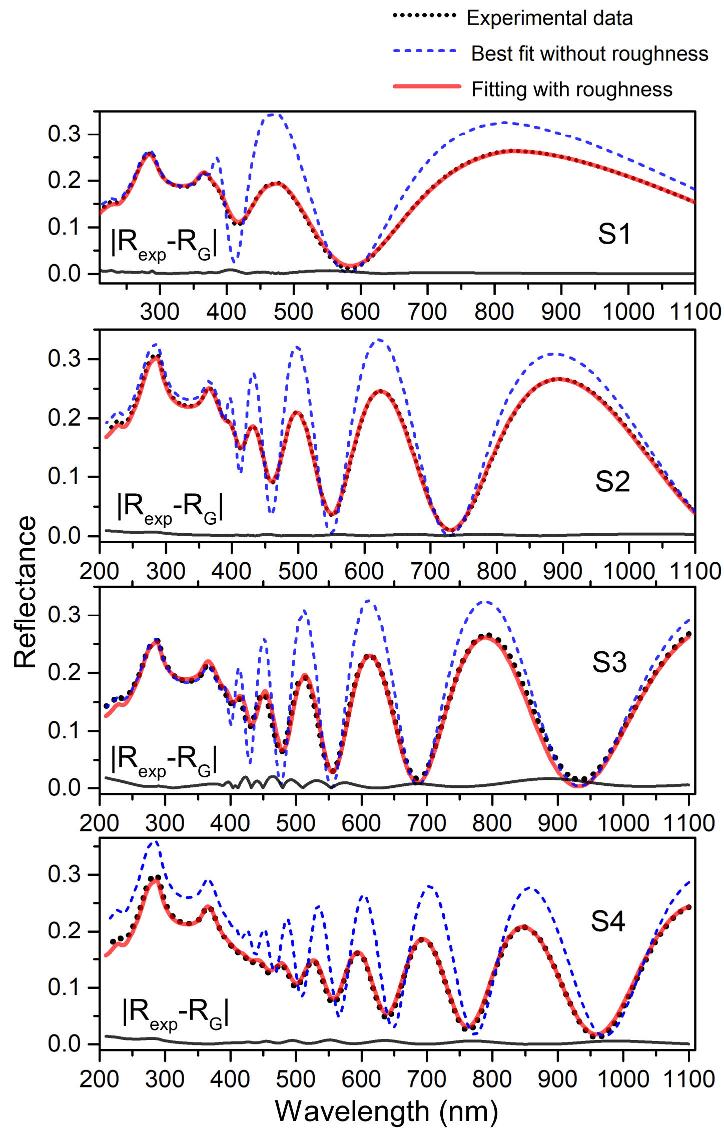

Figure 3.3: Measured reflectance of PSi layers (black dash line), genetic fit without roughness (blue dash line), genetic fit with roughness (red line), and comparison between simulated and measured reflectance (black line)

Table 3.1: Shows the parameter values of best fit for UV-Vis spectra of PSi films shown in Fig. 3.3 and the comparison between the thickness measured by SEM and by the genetic fit.

Sample	$d \pm 5$(nm) GA Fit	$d \pm 10$ (nm) SEM	p ±0,02 GA Fit	$\sigma_0 \pm 1$ (nm) Air/PSi	$\sigma_1 \pm 1$ (nm) PSi/Si	v ±0,1 (nm/s)
S1	225	231	0.63	8	24	8.5
S2	467	477	0.62	5	22	8.3
S3	648	687	0.62	9	23	8.1
S4	900	913	0.62	3	37	8.1

As SEM images Fig 3.2) shows, the interface Air/PSi is smooth, and the values of the σ_0 obtained by genetic fit are lower than 10 nm. This means that the major contribution of the scattering is the PSi/Si interface. It was attained for σ_1 values from 24 nm for S1 to 37.45 nm for S4. Some works about roughness behavior in PSi films reported a monotonous increase of roughness as a function of the etching time until it is reached a saturation value (or limit value) [19, 94]. However, the value of σ_1 remains almost constant for samples S1 to S3 and increases for the sample S4. This fact can be explained due to the effect of other extrinsic parameters such as electrolyte composition [19, 95], temperature [29], and substrate quality [96] that can affect interfacial roughness.

Finally, Fig. 3.4 shows the evolution of the penalty function during 100 generations (Eq. 3.10). The behavior of the penalty function shows that the algorithm finds the solution during the first generations. After that, the algorithms stay in a local minimum even if the mutation parameter increases. This means that there is a bottom edge that the genetic fit cannot overcome. The fitting results of this methodology is dependent on the quality of the measured spectrum and the EMA model used to simulate the theoretical reflectance.

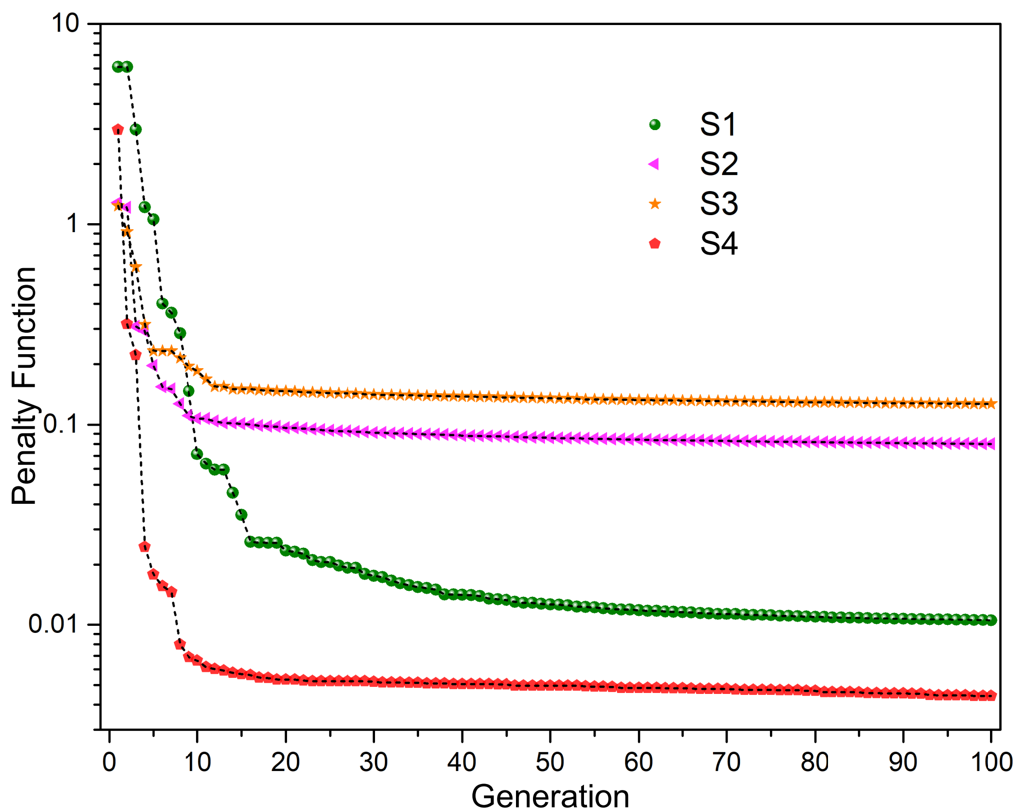

Figure 3.4: Penalty function evaluation progress. Each point represents the best adapted individual of each generation.

3.2. PSi photoluminescence

Photoluminescence (PL) of porous silicon (PSi) has attracted attention in recent years because of its relevance in optoelectronics and sensors applications, and in low dimensional materials physics. There is still a controversy about the origin of each one of the photoluminescence bands, and it is an open scientific and technological problem. It is well known that PL bands may originate mainly from quantum confinement phenomena [51, 97, 98], surface states related to surface chemistry [99, 100, 101], and internal material's interface [102, 103]. In fact, PL generated in silicon (Si) nanostructures arises from complexly interrelated quantum confinement and surface chemistry effects [104], and seems to be because non-interface states are present between Si (substrate) and PSi layers, because silicon columns have not lattice mismatch with the substrate.

The PL spectrum of PSi is strongly dependent on the fabrication parameters, such as ligh-

ting conditions, growing temperature, electrolyte composition, and the intrinsic parameters of the substrate such as the impurity type (p or n), the crystalline orientation, dopant concentration [105], impurities distribution [71], and crystalline quality [40]. In addition, the PL spectrum also depends on extrinsic conditions such as material storage [97, 106], oxidation grade of the surface of PSi, and aging time. Extrinsic and intrinsic parameters involved in the fabrication of PSi, as described above, produce layers with a diversity of mechanical, structural, thermal, and optical properties [97]. Regarding possible applications, an important feature that PSi may offer is as a material for a new generation of anodes with the highest volumetric and gravimetric energy density for Li-ion batteries (LIBs). In this sense, Si, which is cheap and abundant, exhibits the highest energy density known of any LIB's anode material (3.579 mAh/g for Li3.75Si) [107]. However, to accommodate up to 3.75 Li atoms per silicon atom, the silicon structure undergoes a tremendous volume expansion ($>$ 250 %) upon lithiation, resulting in cracking and disintegration of the electrode and severe energy capacity loss [14]. One approach to solve this problem is to produce micro or nanostructured Si anodes that can accommodate the strain. To solve this issue, various methods have been proposed: a) disperse Si nanoparticles between aligned graphene sheets to form a Si/graphene composite [108]; b) flexible graphene sheets that accommodate large volume variations during charge/discharge cycling, preventing particle aggregation, and resulting in significantly enhanced cycling stability; c) producing Si nanowires [107] or 3D porous structures [109]. However, structured Si anodes do not offer a high enough density of the active material yet and may fail when electrode thickness increases. From this point of view, the PSi fabrication process demonstrated in this paper may offer a potential industrial-type approach to produce reliable PSi for LIB's anodes [110].

The dynamics of the growth of PSi films and their evolving, dimensionally dependent, properties are of crucial importance to understand their performance. In the case of the fabrication of thin films and their associated properties, it is necessary to know their physical properties and how these are related to the growth mechanisms and substrate in which films are deposited. One of the main problems related to PSi fabrication is to obtain reproducible materials with the same physical properties, which is directly related to the substrate properties and growing conditions. In this sense, few methodologies have been explored to monitor in-situ the PSi formation. One of these methods is based on monitoring photoacoustic signals emanating from the PSi, which has been demonstrated to be an

excellent technique to follow the formation of the porous layer, to determine etching rate, layer thickness, and refractive index in real time [22, 69]. This methodology guarantees that samples with the same photoacoustic signal are similar.

The controversy in the literature is centered on the mechanisms responsible for PL emission because the porosity of the Si matrix does not guarantee the quantum confinement. The thickness of the silicon walls is not always in the range of confinement, while the surface states are still present due to the broken lattice periodicity, also modified by the presence of other chemical species grown on the surface of Si when exposed to the atmospheric environment. Semiconductor nanostructures exhibit nanometer length scales, and are classified according to their dimensionality: two-dimensional (2-D) quantum wells, one dimensional (1-D) nanowires (or quantum wires) and zero-dimensional (0-D) nanocrystals (or quantum dots) [104]. This classification is directly related to the number of unconfined dimensions along which, carriers (electrons and holes) are still free to move. Sa'ar [104] pointed out that substantially more work is needed to elucidate the origin of the PL bands observed in nanostructured Si, due to the number of variables in the system such as porous sand wall size, porosity, defects density, and impurities, among other factors. However, it has been established that quantum confinement and surface chemistry play critical roles in the underlying mechanism for PSi PL emission.

The porous matrix of PSi obtained by electrochemical etching is a random network which could be described as a pseudo lattice. For nanometric structures, such as nanowire arrays, Lin et al. [98] studied the origin of the PL bands, and they found that the shape and intensity of the PL bands are strongly dependent on the temperature, indicating different origins of each band. However, they did not study the evolution of the PL band as a function of the time under the same laser fluency to identify surface states stability, the origin of the bands, and to establish if quantum confinement or surface chemistry originates these states.

In this work, the PSi samples were obtained by using a photoacoustic cell to monitor in situ the formation of single layers, called A and B, and double layers, called AB and BA. The last ones are stacks formed by a combination of single layers. PL spectra were obtained as a function of temperature from room temperature to 11 K as well as a function of lighting time at 11 K, to study the evolution of the PL bands. Scanning electron microscopy (SEM) was used to measure the PSi layer thickness and to image the nanostructure produced by the etching process. The objective of this work is to study the origins of the PL bands and

develop a methodology to differentiate the contribution of surface states and porous pseudo lattice.

3.2.1. PL experiments on single and double PSi layers

Single layers called A and B were etched using 5 and 40 mA cm $^{-2}$ of current density, respectively, during eight PA cycles. The bilayer AB was etched initially with 5 mA $^{-2}$ to produce the A layer, followed by etching with 40 mA $^{-2}$ to make the B layer. On the other hand, the bilayer BA was etched initially with 40 mA $^{-2}$, followed by etching with 5 mA $^{-2}$. Every current lapse was fixed during four PA cycles. Here, it is crucial to note that the control parameter of the etching process is the PA cycle. If the PA cycle for two different samples exhibits the same behaviors, it is an indicative that both samples have the same physical properties. The etching time is the sum of the PA cycles. After the formation of the porous structure, the samples were rinsed with ethanol and kept on a vacuum conditions for the ex-situ characterizations.

Figure 3.5 shows the PA amplitude signal for all samples. Figure 3.5 (a) shows a single layer A grown during eight PA periods of 46.2 s each; (b) shows layer B with eight periods of 13.3 s each; (c) a bilayer AB that is a combination of current densities of layers A and B, and finally the bilayer BA (Figure 3.5 (d)). It is evident that the period value for each current density is closely the same for the single and the bilayer growth, meaning that the proposed method for in situ monitoring of PSi layer growth is highly accurate. By using the etching methodology described above, it is possible to produce PSi layers, with similar physical characteristics, that is crucial for the design and fabrication of devices based on PSi. The PSi layers were analyzed using top and cross-section SEM imaging to determine surface and edgewise morphologies.

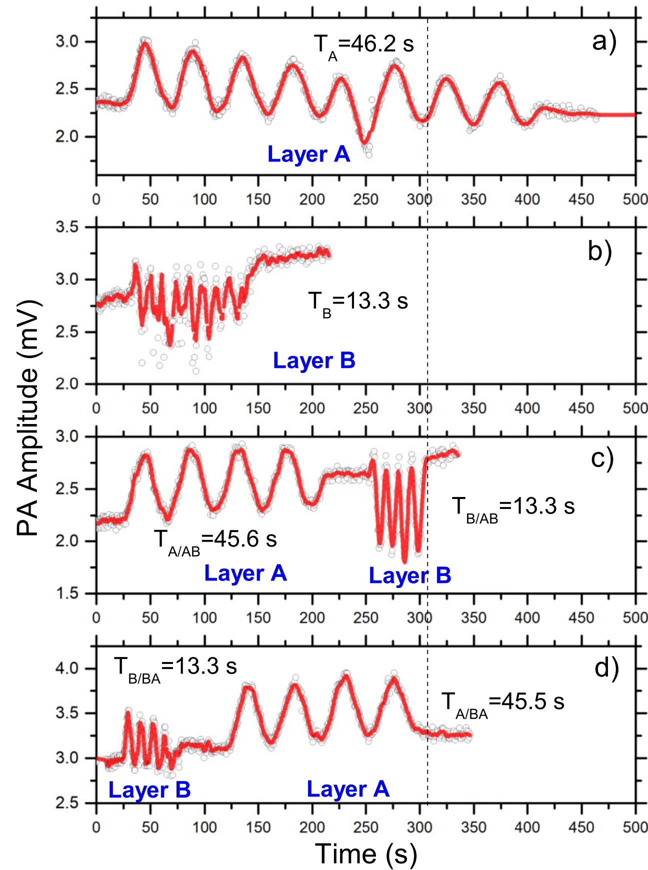

Figure 3.5: Photoacoustic amplitude obtained during the Si etching. (a) Single layer etched at 5 mA cm $^{-2}$, (b) single layer etched at 40 mA cm $^{-2}$, (c) bilayer etched at 5 and 40 mA $^{-2}$, (d) bilayer etched at 40 mA cm−2 and 5 mA cm^{-2}.

Figure 3.6 shows SEM images of the surface of PSi layers. SEM images of the top PSi layers A and B are shown in Figure 3.6 (a) and (b), respectively. The inset in these figures shows the pore size distribution (IMAGEJ) that is, in fact, the Feret diameter. For A layer, the porous distribution is center in 15 nm, and for B layer this parameter exhibits non-Gaussian distribution and porous distribution varies from 20 to 160 nm. An important aspect is that in the case of bilayers AB and BA the porosity of the inner layer does not affect the top layer.

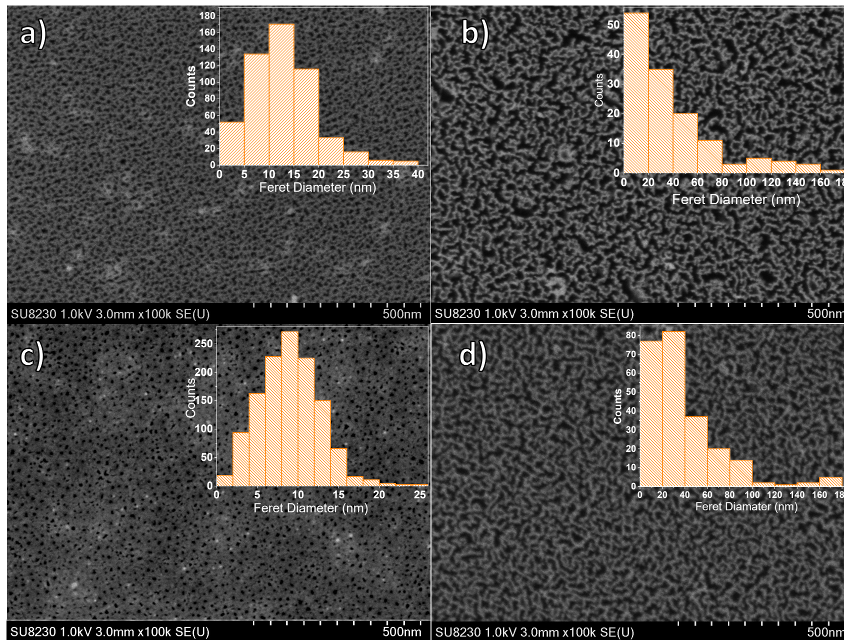

Figure 3.6: Top SEM view of the PSi layers: (a) layer A, (b) layer B, (c) bilayer AB, and (d) bilayer BA.

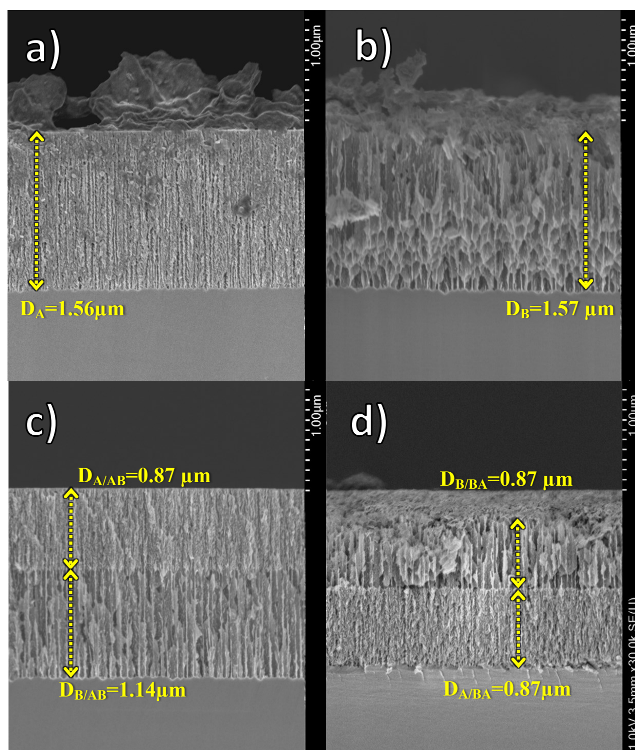

Figure 3.7: Cross section SEM images of PSi layer A (a), layer B (b), bilayer AB (c), and bilayer BA (d).

Figure 3.7 shows cross section SEM images of the PSi layers. The layers thickness obtained through image analysis is 1.56 μm for sample A, 1.57 μm for sample B. For the bilayers, grown with half the cycles of singles layers, the thickness obtained is half the thickness of the single layers. These images showed clearly that through PA technique, we have control on the PSi layer thickness to produce multilayers with closely the same physical dimension. On the other hand, Figure 3.7 shows that if the porous diameter increases, the wall thickness decreases, implying that this parameter could influence the PL spectra.
Figure 3.8 shows the PL spectra of bare and wet PSi layer A at different temperatures (from 11K to 300K). The PL spectra relate to PSi structure does not have any treatment, meaning that the surface of the PSi sample can contain different chemical species such as H, C and O [111]. These spectra are formed by at least three characteristic bands located at 777 nm (1.59 eV), 706 nm (1.75 eV), and 637 nm (1.94 eV) at 11 K. It is relevant to notice that when the temperature decreases there is not a shift of these bands, meaning that these emissions are not associated to band to band transitions of Si and could be associated with surface states. The origin of the surface states is well discussed by Koch et al. [99].

Figure 3.8 (b) shows PL spectra of the bare PSi layer B with the following bands found at 613 nm (2.02 eV), 698 nm, (1.77 eV) and 814 nm (1.52 eV). These bands present a small shift when the temperature decreases, indicating that these spectra involve more than one emission mechanism, potentially related to surface states, quantum confinement, as well as states formed in the PSi layer, originated from a pseudo lattice (dot, wire, well). Layer B, according to the porous analysis, exhibits a higher porosity and less wall thickness than layer A. Here, it is very important to point out that it is possible to have states associated to the PSi pseudo lattice overlapped with surface states. It is important to point out that in the case of layer B, for which the thickness of the walls is less than layer A, there is a blue shift in the PL spectrum.
In the case of Figure 3.8 (c) and (d) for PSi bilayers AB and BA, respectively, the spectra are formed by the superposition of the PL states of layers A and B as is expected. Considering the SEM images shown in Fig 3c and d, and the PL spectra of bilayers shown in Fig. 4c and d, it was confirmed that the Si/ PSi as well as PSi/PSi interfaces do not contribute with new PL sates, which is an indication that no mismatch between interfaces exists.

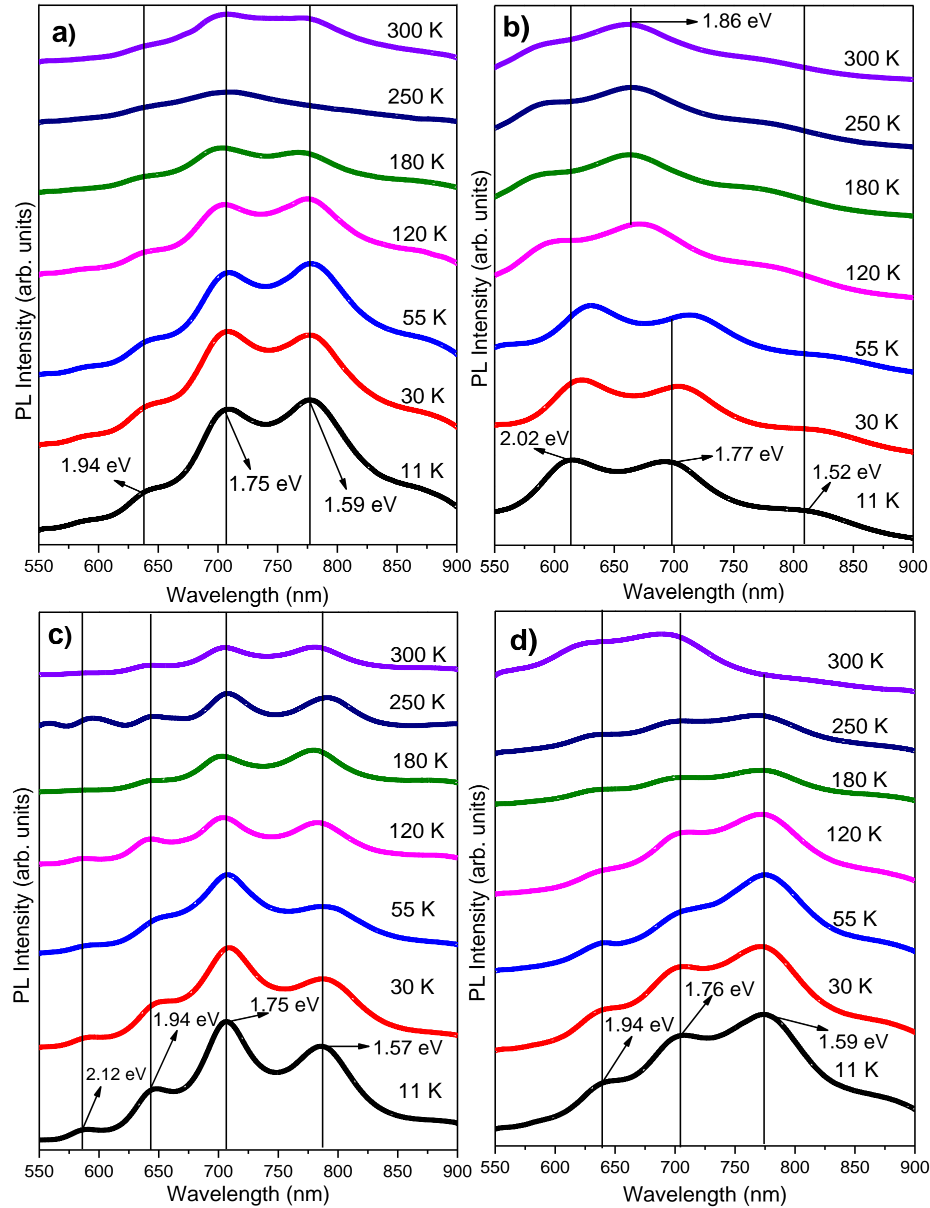

Figure 3.8: PL spectra as a function of temperature for (a) layer A, (b) layer B, (c) bilayer AB, and (d) bilayer BA.

There is an indicative that surface states are mainly responsible for the PL spectra [111] and it is necessary to explore the existence of quantum confinement. To identify the PL contributions, PL spectra were obtained as a function of the time under the same laser fluency and continuous laser excitation. Considering the PL spectra obtained for layers A and B, it is necessary to clarify if these states are only associated with surface states.

Therefore, it is important to study the stability of these surface states. As was pointed out, the surface states are sensitive to the laser fluence and it means that these states can be metastable states. The continue laser fluency produces the optothermal annealing that can be detected by the change in the spectral band of surface states [40].

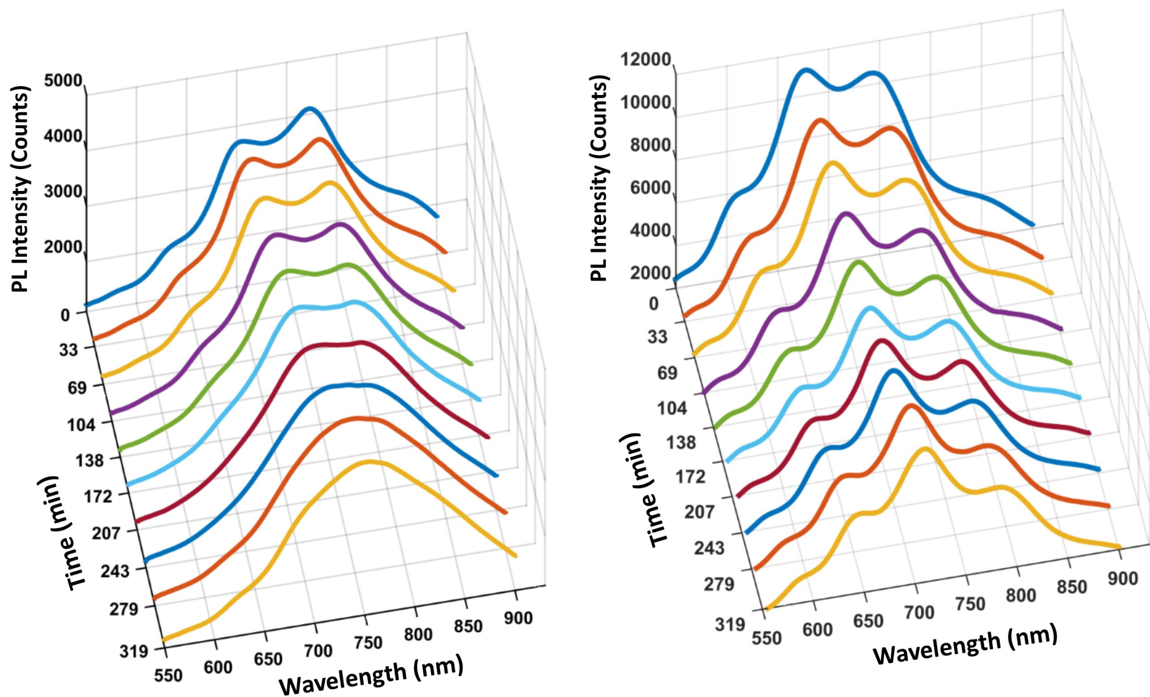

Figure 3.9: Temporal evolution of the PL spectra for layers A and B from 0 min (initial step) to 319 min (final stage) under continuous laser fluency.

Figure 3.9 (a) and (b) show the temporal evolution of the PL spectra for layers A and B from 0 min (initial step) to 319 min (final step) under continuous laser fluency. As it was showed in Figure 4 (a), the surface states located at 777 nm (1.59 eV), 706 nm (1.75 eV), and 637 nm (1.94 eV) at 11K disappear as a function of fluency time, and broadband centered at 755 nm emerges. This broad band, is in fact, a set of states that were overlapped by the surface states. In the case of layer B, this behavior is enhanced: after the long laser fluency, the new bands emerge, indicating that surface states disappear, and the most stable pseudo lattice states were in fact overlapped with surface states. Finally, the PL spectra of PSi can be described as the superposition of the surface states and the states formed by the pseudo lattice.

To study the surface state stability, these samples were kept in the PL chamber at 10^{-6} Torr and 11 K for 24 h without illumination. After that, the laser was stabilized for 40 min and the PL spectrum was taken. Figure 6 shows the PL spectra of the PSi layer A measured at 11 K and 0 min, after 319 min of exposition to laser fluency and after 24 h of sample storage in the vacuum chamber. As can be seen, the surface state appears again indicating that these states are in fact metastable states. Figure 6 (b) shows for layer B the results of the same experiment, in which the surface states appear again.

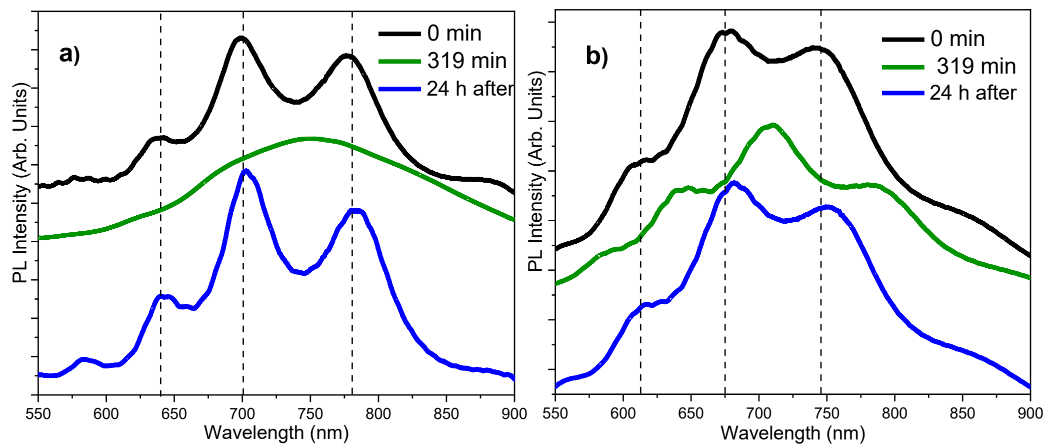

Figure 3.10: (a) PL spectra of layer A taken at 11 K (black line), 319 min after continuous laser fluency (green line), and 24 h after turning off laser incidence (blue line). (b) The same experiment for layer B.

The metastable states can be considered as the states in which there is a possibility that the system returns to the normal excited state by opto-thermal excitation. As expected, the emission bands are sharper at low temperatures than at high temperatures, meaning that dispersive processes increase with temperature but, as maxima do not move in energy, band to band transitions are not responsible for these emissions. According to this result, PL emission is mainly attributed to transitions between states generated in the PSi surface because of its huge surface due to the porous structure. Therefore, the contribution of the porous layer as pseudo lattice is weak compared to the surface contribution. However, surface states are metastable states. The knowledge of the PSi states is fundamental for device design and performance.

CHAPTER 4

One-dimensional photonic crystal based on porous silicon

The refractive index of crystalline silicon exhibits a plateau in the range of 1100 to 500 nm as Figure 4.1 (a) and (b) show. This means that the refractive index and absorption coefficient are almost constants getting it an excellent candidate to fabricate mirrors (distributed Bragg reflectors) and optical microcavities (OMC). Of course, it is required mechanisms to tune the refractive index value to manufacture devices with specific characteristics. This mechanism is the porosification of crystalline silicon making it an effective medium with an effective refractive index. Consequently, this work proposes a methodology to fabricate customized one-dimensional PhC based on porous silicon through the monitoring and control of the electrochemical etching using differential photoacoustics.

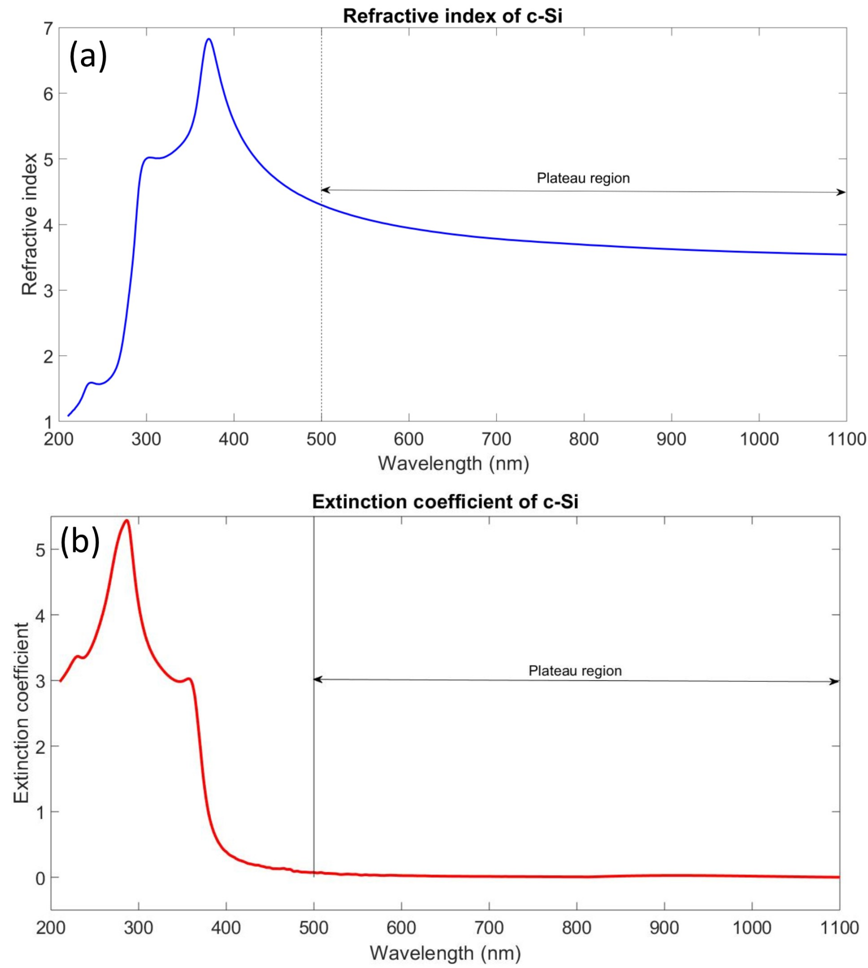

Figure 4.1: Optical constants of crystalline silicon. (a) Refractive index. (b) Extinction coefficient.

4.1. Etch Calibration

The PSi formation using electronically etching in HF media is dependent on several extrinsic and intrinsic parameters. It was found huge variability in the optical and morphological properties of PSi films due to substrate quality and etching process. Despite that, it is possible to obtain reproducible Phc if a calibration of the cell is performed. Consequently, in situ photoacoustics allows this calibration, also permits monitoring and control in real time to correct any unexpected event during the PhC fabrication.

On the other hand, the above chapters were focused on the study of the optical and morphological properties of PSi films grown in HF aqueous media and monitored by using In situ differential photostatic. This information is required for the design of PSi PhC. The optical quality is a crucial aspect of PhC, in particular for PSi-based PhC because of PSi material exhibit a random distribution of porous, branching, and roughness interfaces that produces optical losses through the scattering. Hence, it is imperative to consider this effect over the PhC properties such as stopband position, bandwidth, and reflectance percentage.

4.1.1. Substrate quality determination by PCR imaging

It is well known that Si wafers present non-homogeneous carrier distribution[39, 72], and defects induced for the fabrications method and cleaving process. These can influence the PSi formation during the etching process given that the local magnitude of the electric field changes as a function of the position. Usually, it is recommended to measure the nominal resistivity of the Si substrate [63], but it is an average value that does not give information about local variations of the carrier distribution. Figure 4.2(a) shows ten different areas from the central part of the wafer that were used to obtain the photocarrier images. Figure 4.2(b) shows the PCR amplitude for points 3 to 7 while the inset in this figure shows the changes in the phase for a point in these locations. The changes in the PCR amplitude around 1000 Hz have been associated with the changes in the minority carrier diffusion coefficient that are directly related to the carrier concentration [40, 39]. It means that the wafer does not have a uniform carrier distribution. Moreover, the phase signal is not quite sensitive to the changes in the carrier distribution. Figure (2)c shows the PCR amplitude of the ten regions across the wafer, red colors represent high carrier concentration while the blue ones can be associated with a decrease in the carrier concentration. These PCR images evidence the non-uniformity in the carrier distribution that has to affect any electrochemical process and porous distribution.

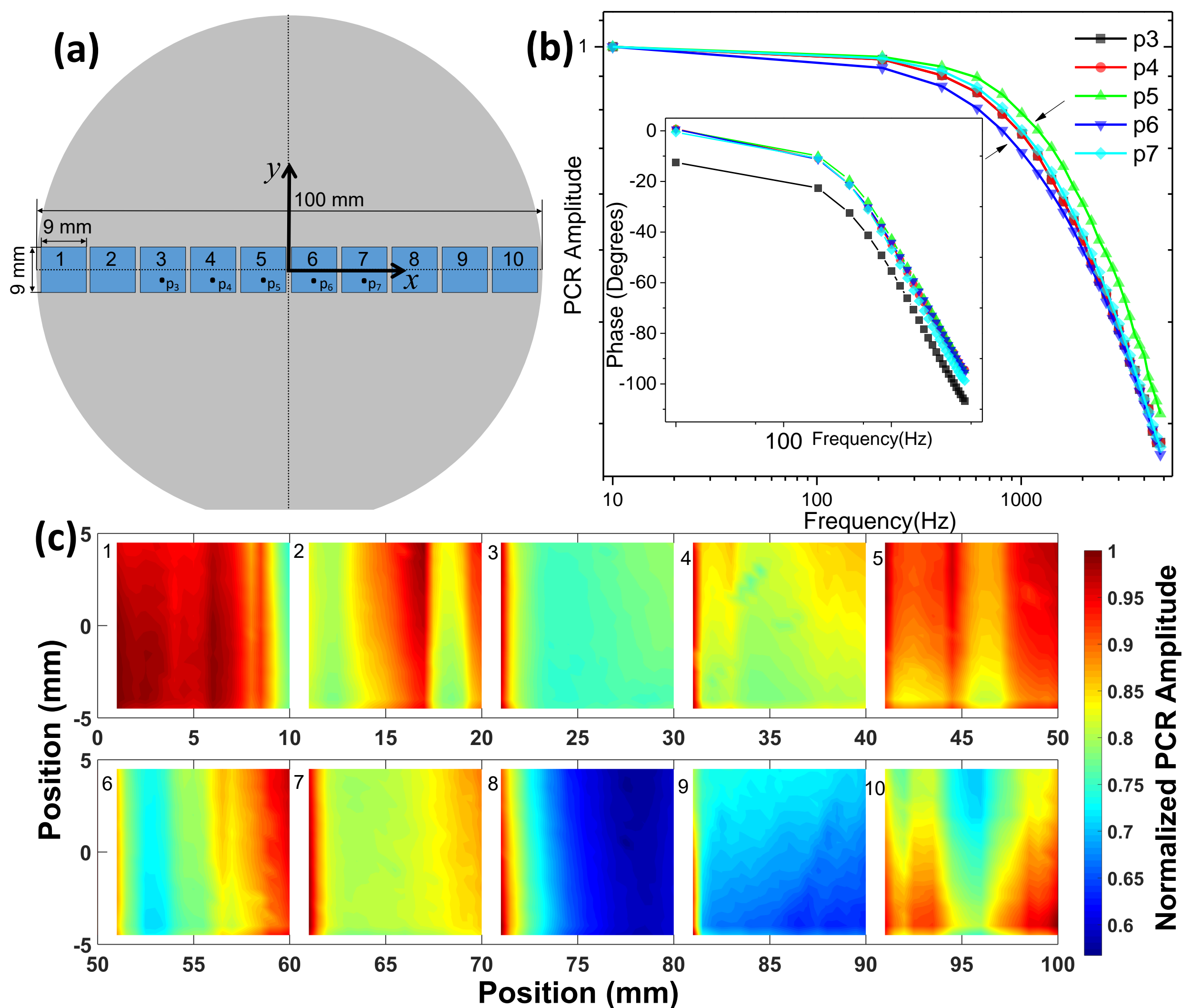

Figure 4.2: (a) Shows the silicon wafer and the scanned places by PCR radiometry. (b) PCR amplitude and phase of five points located at the center of the wafer. (c) Thermal images across the wafer. Laser beam radius 500μm. Frequency 1 kHz.

4.1.2. Etch calibration by in-situ photoacoustics

After a completed PCR imaging of the c-Si sample, a selection of substrates with homogeneous carrier distribution and similar nominal resistivity were chosen (Figure 4.2 (a), i.e., samples 3, 4, 8, 10) to fabricate two series (S1 and S2) of individual layers varying the anodizing current density from 5 to 60 mA cm^{-2}, and to control the cell and electrolyte temperature at 25 °C. These series were used as a calibration of the cell. Each etching was

monitored using a differential photoacoustic system [20]. This technique allows controlling the etching time through the monitoring of one photoacoustic cycle. PA effect is produced by the absorption of modulated light (heat source) that produces a heat diffusion process. Moreover, the changes in the optical path, as a result of the formation of the porous film, makes a self-modulation of the intensity of incident radiation (changes in the reflectance) that modules the PA effect. This modulation is periodic [21] and depends of the phase given for normal incidence by:

$$\delta(t,p) = \frac{2\pi\eta_i(p)d_i(t)}{\lambda_0}, \tag{4.1}$$

where $\eta_i(p)$ is the real part of the refractive index of the film that is porosity (p) dependent, d_i is the thickness film, and λ_0 is the wavelength of the laser. The maximum of PA signal occurs when the reflectance of all the structure is a minimum, and it takes place when $\delta(t,p) = (m - \frac{1}{2})\pi$. Consequently, the minimum of the PA signal is reached in a maximum of reflectance when $\delta(t,p) = m\pi$, for $m = 1, 2, 3...$, that is related to the number of PA cycles.

Figure 4.3(a) shows the time of one PA cycle as a function of current density. As eq 4.1 shows, the increase of current density rises the etching rate and film porosity producing a reduction of the PA cycle. The etching rate is directly related to the velocity formation of the porous film, and it was determined by the PA model developed previously [22]. After that, reflectance spectra were measured and fitted by using genetic algorithms (GA) reported by Ramirez-Gutierrez [86, 112] to determine simultaneously the effective porosity (Figure 4.3(b)), interfaces roughness [54], and thickness using the transfer matrix method (TMM). Figure 4.3(c,d)) shows the interface roughness of air/PSi (σ_{01}) and PSi/Si substrate (σ_{12}) interfaces. This parameter is critical depending on electrolyte composition and temperature. Only roughness values of less than 20 nm were found.

Porosity is usually determined by gravimetric analysis [113], but in this work, two methods to determine it as a function of current density were used (Figure 4.3(b)). In the first one, the reflectance spectrum of every single film was fitted and compared with a simulated one using the refractive index calculated by Looyenga EMA rule [1, 2, 43]. The second was carried out using the anti-reflective condition on the PA signal, and the thickness was determined by SEM. This shows that it is probable to obtain a refractive index for λ_0 using eq 4.1, making it possible to introduce this value in the Looyenga EMA to calculate the

porosity. In order to achieve this, refractive index of HF as 1.157 [114] and for ethanol 1.365 were used.

There are some discrepancies the porosity values (figure 4.3(b)). Nonetheless, it is well known that the porosity determined by optical methods is model dependent [33, 115]. Besides, the roughness of PSi interfaces is critically reliant on electrolyte temperature and composition (HF/surfactant ratio) [29]. For the calibration series, the parameters electrolyte temperature and composition were retained constants.

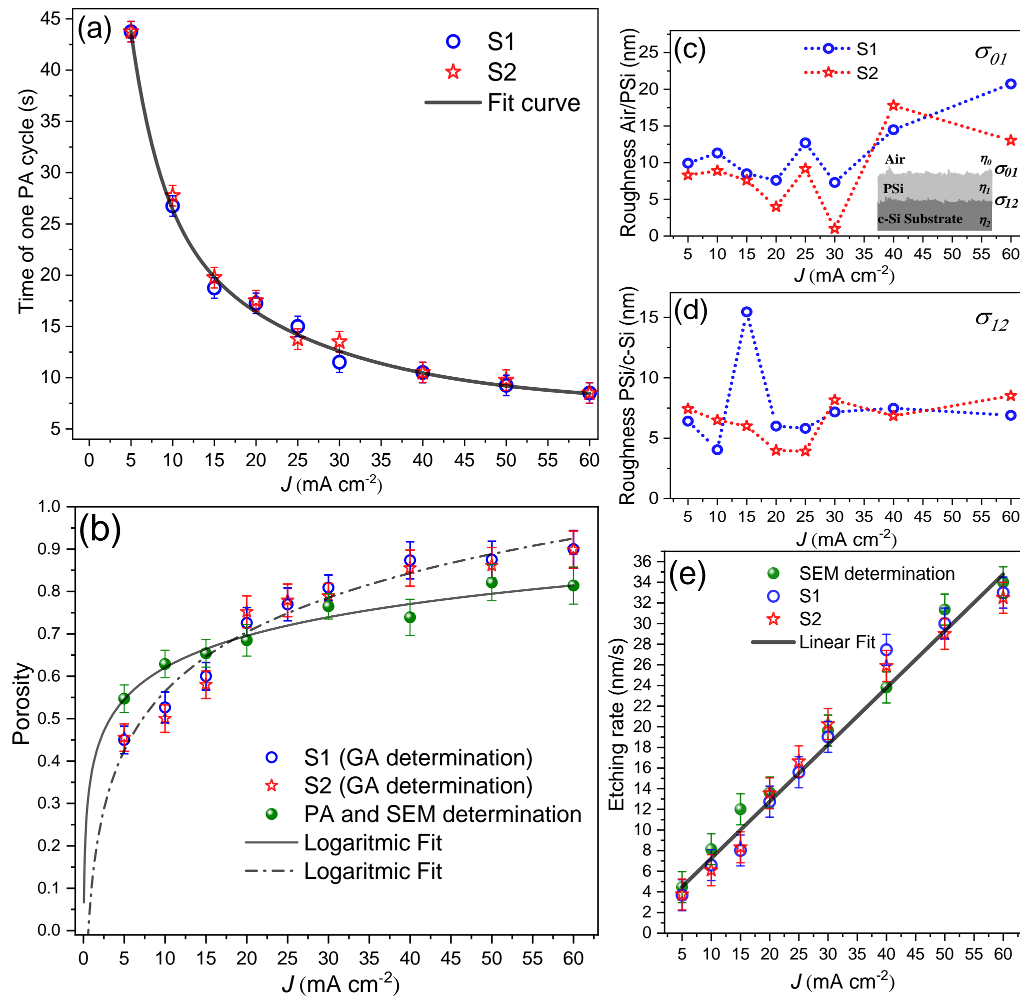

Figure 4.3: Calibration series parameters. (a) PA time as a function of current density that exhibits an exponential decay behavior. (b) Average porosity determined by GA and PA-SEM, (c) and (d) interfaces roughness as a function of current density determined by GA fitting of UV-Vis spectrum. (d) Etching rate that exhibits linear behaviour.

Moreover, layer thicknesses calculated by GA and the ones measured by SEM (Figure 4.4) were close. Also, the etching rate was obtained using two methods: the PA methodology fitting the PA amplitude [22] and by direct calculation using the total etching time and the SEM thickness. Figure 4.3(e) shows the etching rate as a function of current density obtained through the fitting of PA amplitude and SEM images. As can be seen, the etching rate has a linear behavior from 5 to 60 mA cm^{-2} of anodizing current.

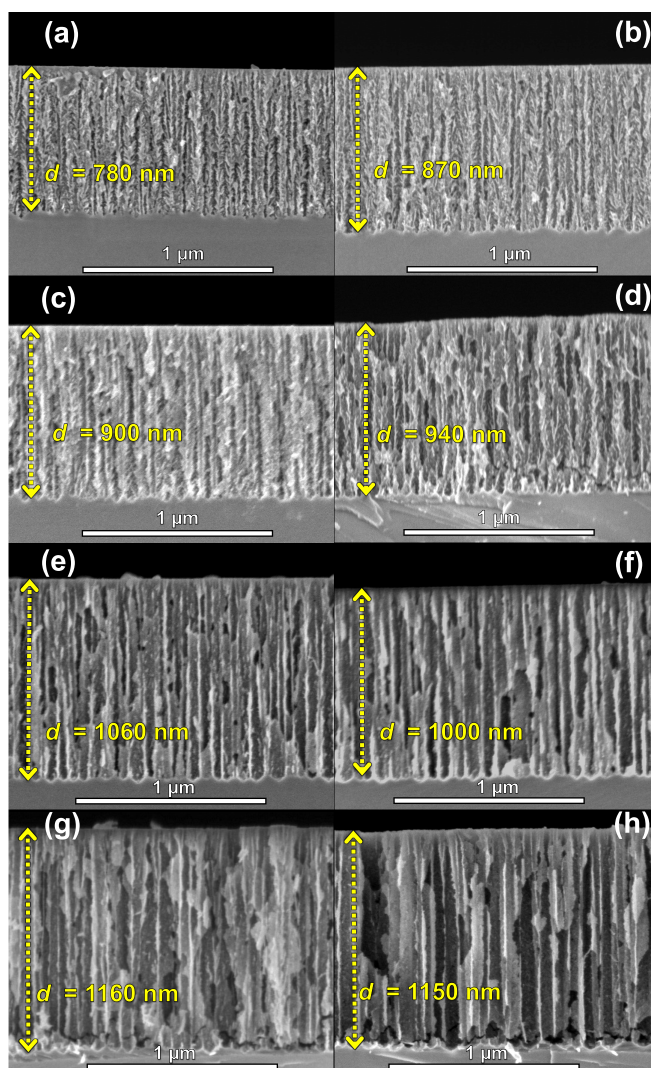

Figure 4.4: Cross-section SEM images of calibration series. (a) 5 mA cm^{-2}, (b) 10 mA cm^{-2}, (c) 15 mA cm^{-2}, (d) 20 mA cm^{-2}, (e) 30 mA cm^{-2}, (f) 40 mA cm^{-2}, (g) 50 mA cm^{-2} y (h) 60 mA cm^{-2}.

Figure 4.4 shows the cross-section of some single films of the calibration series. It was observed in these images that porosity and etching rate increase as a function of the current density. Besides, all samples exhibited straight porous formation and interfacial roughness mainly in the interface PSi/substrate.

4.2. Design and Simulation of Photonic Structures.

Optical properties of a multicomponent system can be described as a mixture of dielectric functions (effective medium approximation), that in the case of PSi is a mixture of dielectric properties of c-Si host matrix ($\hat{\epsilon}_M$) with incrustations within it of another material that full the pores ($\hat{\epsilon}_1$) (some gas or liquid). The incrustations size with a dielectric function ($\hat{\epsilon}_1$) in the majority system ($\hat{\epsilon}_M$) must be comparable or less than the wavelength of the radiation that interacts with the medium. The effective dielectric function [2, 43] can be described as by using Eq. 3.2. In particular, the porosification of c-Si reduces significantly the refractive index compared to the c-Si. This means that the values available of refractive index for PhC design are between the c-Si and the filling material (i.e. $\eta_{Si} = 3{,}675$ and $\eta_{air} \approx 1$ at 800 nm) [116].

Reflectance is calculated through transfer matrix method (TMM) [54, 74, 79]. It is considered a multilayer system of n films with a complex refractive index $\hat{N}_k = \eta_k + i\kappa_k$, and $n+1$ interfaces as is shown in Figure 4.5. At the interface k^{th}, the Fresnel coefficients are defined in terms of the optical admittance, which is a ratio of tangential components of the electric and magnetic fields amplitudes. Besides, this formalism allows introducing the effects produced by random irregularities (roughness) in each interface through the modified Fresnel coefficients.

This approximation supposes that the interface irregularities are smaller than the incident wavelength, i.e., $\Delta h \ll \lambda$. Therefore, the description can be made by using the root mean square (RMS) roughness (σ_k) of each interface.

The effect of the interface roughness in the optical response of photonic crystal was studied by Lujan-Cabrera et. al [54]

Thus, the DBR structures were designed using TMM method considering the quarter-wave condition [117] (eq 4.2) and the bandwidth (eq 4.4) given by

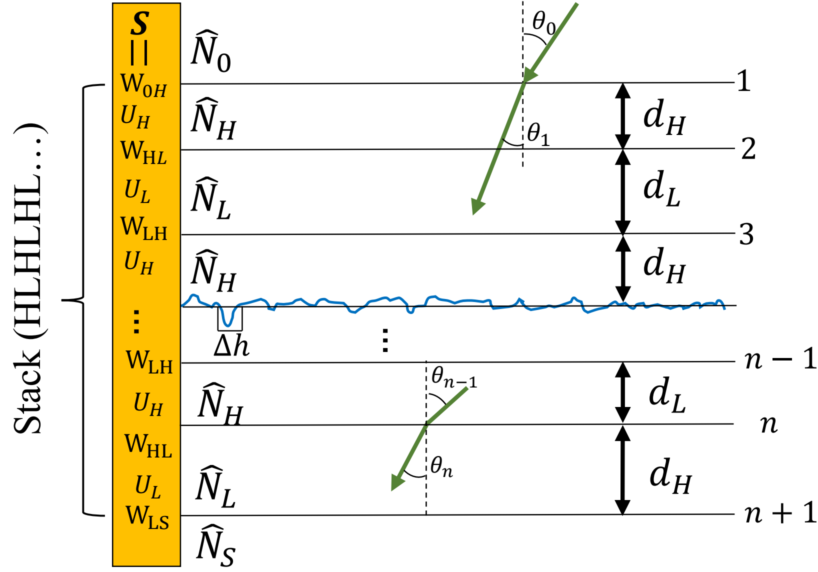

Figure 4.5: Schematic of the multilayer structure composed by n films that form $n+1$ interfaces. The order of subscripts indicates the propagation direction.

$$\lambda_0 = 2\left(\eta_H d_H + \eta_L d_L\right), \tag{4.2}$$

$$\frac{\Delta\lambda}{\lambda_0} = \frac{\pi}{2}\left(\frac{1}{\cos^{-1}(\rho)} - \frac{1}{\cos^{-1}(-\rho)}\right), \tag{4.3}$$

$$\rho = \frac{\eta_H - \eta_L}{\eta_H + \eta_L}, \tag{4.4}$$

where λ_0 is the Bragg wavelength, η_H and η_L, d_H and d_L are the refractive indexes, and thickness of high and low layers respectively. The intensity, shape, and width of the stopband are also dependent on the number of periods of refractive indexes ratio (ρ) of H and L layers as Eq. 4.4 shows. Considering these conditions (Eq. 4.2 and Eq. 4.4), refractive indexes are selected taking into account the desired bandwidth and stopband position. These determine the thickness of each layer.

Table 4.1 shows the parameter values for PhC structure design. For each PhC is summarized the refractive indexes, layers thickness, and the sequence that indicates the number of pairs and the location of the defective layer in the case of the OMC. Furthermore, it is worth noticing that the refractive index of c-Si has a plateau between 500 and 1450 nm, and it increases fastly for values near to UV as the absorption coefficient does[116]. It means that it is recommendable to design PSi PhC in the plateau region.

Table 4.1: Parameters design of photonic PSi structures.

Structure	DBR550	DBR700	DBR750	OMC1	OMC2
sequence	$(HL)^{15}S$	$(HL)^{15}S$	$(HL)^{15}S$	$(HL)^3L_{c_1}(HL)^3S$	$(HL)^3L_{c_2}(LH)^6S$
η_H	1.45	1.68	2.26	1.88	2.08
η_L	1.16	1.18	1.97	1.31	1.25
η_{L_c}	–	–	–	2.21	2.04
d_H (nm)	95	103	83	96	78
d_L(nm)	131	145	96	134	136
d_{L_c}(nm)	–	–	–	323	167
λ_0(nm)	550	700	750	–	700
$\Delta\lambda$(nm)	78	159	66	155	230
σ_{HL}(nm)	10	10	10	10	10

4.3. Fabrication and characterization of photonic structures

The first step was to select c-Si substrates with a homogeneous carrier distribution tested by PCR and Vander Pow method. This guaranteed the substrate quality. The refractive index (Table 4.1) fixes the porosity according to EMA theory [2, 43]. At the same time, the porosity defines the current density for the etching process. These values were selected from the calibration series (Figure 4.3 (b)). The next step was to calculate the etching time using the value of the etching rate (Figure 4.3 (d)). Consequently, all the parameters mentioned above defined the photoacoustic profile that was used as a control parameter for the etching. Table 4.2 summarized the fabrication conditions.

Table 4.2: Experimental parameters used for PSi PhC fabrication. The thickness of each layer was determined by SEM.

Structure	DBR550	DBR700	DBR750	OMC1	OMC2
sequence	$(HL)^{15}S$	$(HL)^{15}S$	$(HL)^{15}S$	$(HL)^3L_{c_1}(HL)^3S$	$(HL)^3L_{c_2}(LH)^6S$
$t_H \pm 0.05$ (s)	6.03	16.87	13.20	16.87	12.28
$t_L \pm 0.05$ (s)	4.40	4.25	8.20	4.25	4.29
t_{L_c} 0.05 (s)	-	-	-	97.25	24.69
J_H (mA/cm^2) ± 0.01	25	7.21	10	7.21	7.21
J_L (mA/cm^2) ± 0.01	60	58.48	20	58.48	58.48
J_{L_c}(mA/cm^2) ± 0.01	-	-	-	4.42	7.21
p_H	0.75	0.41	0.57	0.41	0.41
p_L	0.91	0.91	0.70	0.91	0.91
p_c	-	-	-	0.41	0.41
d_H (nm)	90±5	107±8	110±8	107±6	85±5
d_L (nm)	140±9	143±7	122±8	143±7	152±7
d_c (nm)	-	-	-	335±5	168±7
λ_0 (nm)	572	725	764	700	700
$\Delta\lambda$ (nm)	101	150	67	146	246

The previous works done by this group[21, 22, 20] showed that the PA cycle observed during the PSi formation depends on refractive index, porosity, etching rate, and laser wavelength (Eq. 4.1), and the etching rate is almost constant for short anodizing times. Thus, each frequency component of PA signal is related to a single film formation. In order to obtain good control of the formation process, it was designed a selected layer thickness in which anodizing times were half multiplies of PA cycles. This means a minimum or a maximum to obtain symmetric cycles that is the case of samples DBR550 and DBR700. If the etching time does not satisfy this condition, the PA signal will have a beat behavior. Hence, the PA amplitude contains all frequency components of the etching rate of PSi films formation.

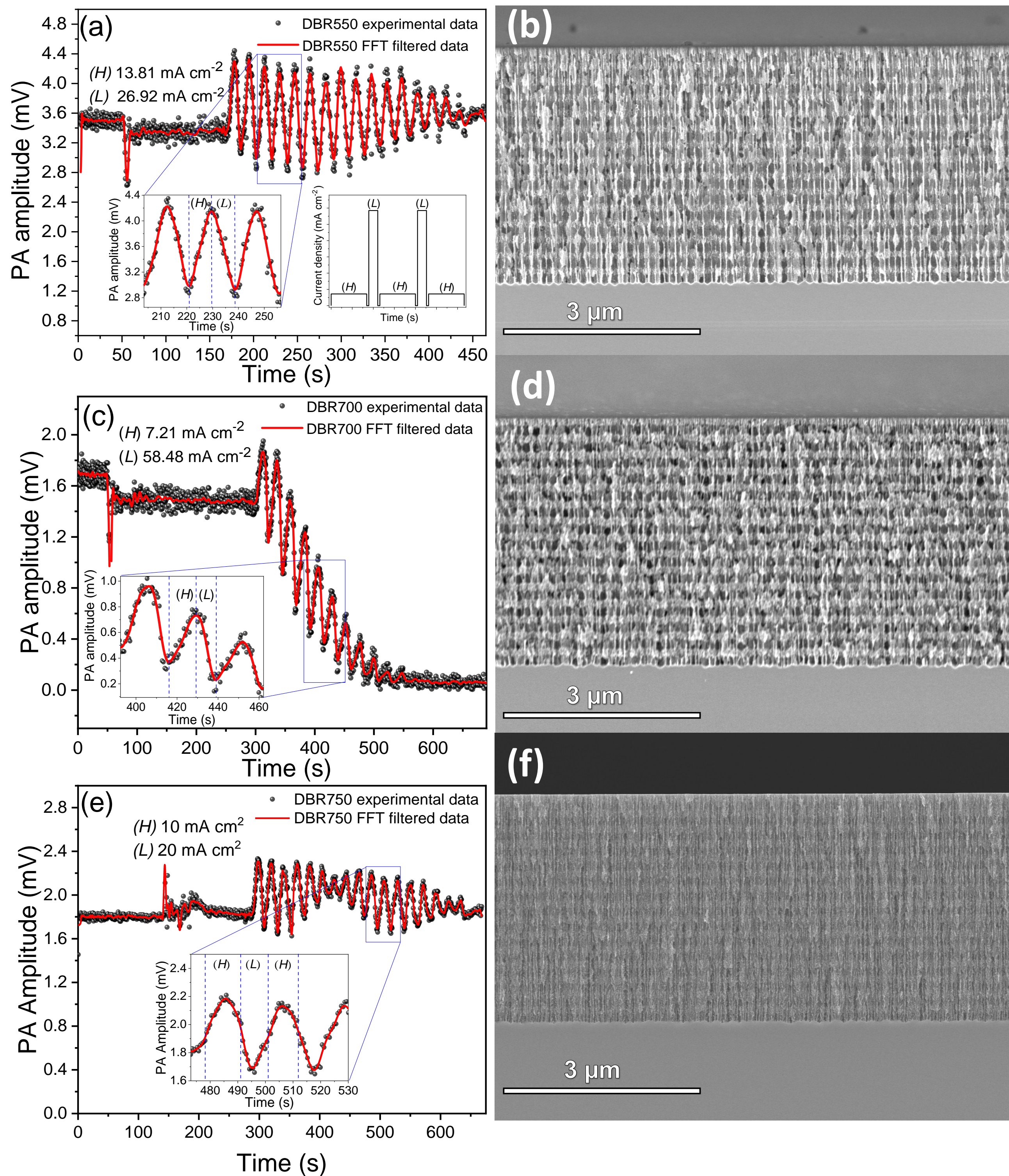

Figure 4.6: PA amplitude during DBRs fabrication. (a) DBR550, (c) DBR700, (e) DBR750. (b), (d), and (f) are its respective cross-section SEM images. Inset in (a) shows the current density profile used for DBRs fabrication.

Figure 4.6 shows the in-situ PA signal for each designed DBRs as well as their cross-section SEM images. For the DBR550 (Figure 4.6 (a)) and DBR700 (Figure 4.6 (c)), the etching time was set as a half of one PA cycle for the corresponding current density (see Table 4.2). Thus, a complete period in the PA signal represented a pair of HL layers. The porosity ratio between H and L allows clear identification of each layer as is shown in Figure 4.6 (b) and (d), furthermore, all interfaces exhibited roughness. In the case of DBR550, the bandgap was centered at 550 nm and its bandwidth was 78 nm, so it did not reflect the wavelength (808 nm) of the laser that produces the PA effect. Therefore, the PA amplitude decreased only when the optical path increased. For DBR700 the PA amplitude decreased fast, even the PA periods disappeared after the formation of eleven pair of layers. This is an expected result given that the optical bandgap was near to the laser wavelength. This means that the most fraction of the incident radiation was reflected and the PA effect disappeared. DBR750 PA signal in Figure 4.6 (e) corresponds to a beat profile since the etching time of each layer is not an integer multiple of a half PA period. For this reason, one period does not correspond to a pair of layers. However, PA amplitude frequency components allow the control of the etching process because the frequency associated with each layer is well known. DBR750 was designed with low porosity ratio and current densities that produce low contrast in the stack cross-section SEM image. Even though, the stack conformation is appreciable.

Measured and simulated reflectance spectra of DBRs are presented in Figure 4.7, and the obtained structural and optical parameters are summarized in Table 4.2. All DBRs display red-shifts and bandwidth narrowing compared with the simulated ones. These are due to parasite capacitance in the stack structure and the electrochemical circuit[118, 119] which the current source cannot control. Consequently, the discharge process held the etching during a short time generating layers thickness higher than the designed ones. Nonetheless, the deviation in the thickness of the layers, related to the designs, was around 15 nm that produced a red-shift in the stopband position proportional to the optical path.

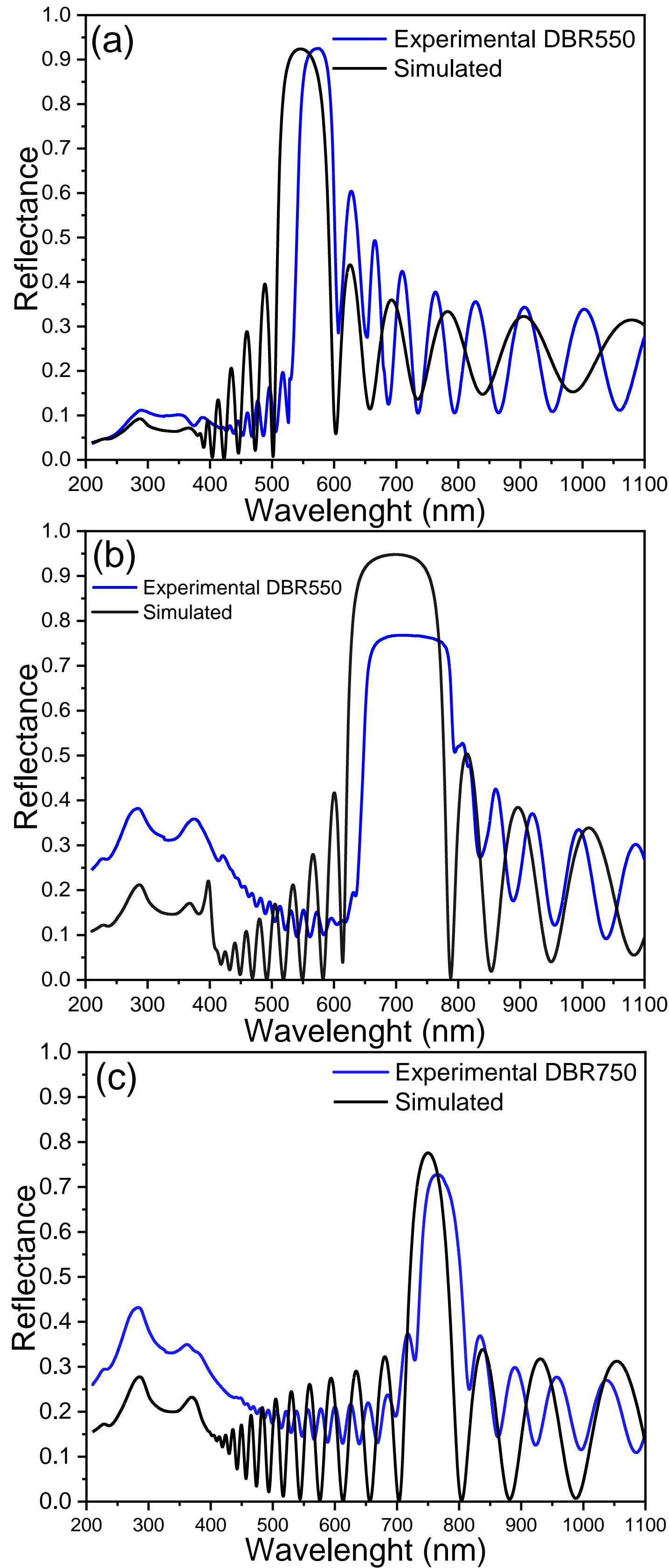

Figure 4.7: Reflectance spectra simulated (blue line) and measured (black line) for (a) DBR550, (b) DBR700, and (c) DBR750.

Figure 4.8 (a) and (c) shows the PA amplitude signals, and insets represent the current profile used to fabricate the OMCs. Figure 4.8 (b) and (d) shows the cross-section SEM images for the OMCs. OMC1 and OMC2 were manufactured using the same conditions of BDR700, this means that it was introduced a defective layer into the DBR700 structure. The experimental parameters used for OMCs fabrication are summarized in Table 4.2.

The OMC1 stack was design as $(HL)^3L_{c_1}(HL)^3S$ sequence. In the micrograph (Figure 4.8 (b)) given that the current density used for the defective layer is near to the used one for H layer, there is no porosity contrast to differentiate H to L_{c1} layer, and it looks like a thick one. However, PA amplitude clearly shows the formation of a defective layer that corresponds to two PA cycles. The defective layer was designed with a thickness of 335 nm to make two cavities into the bandgap located at 650 and 787 nm.
OMC2 (Figure 4.8 (c) and (d)) was design as $(HL)^3L_{c_2}(LH)^6S$ sequence with a defective layer of 168 nm that produces a microcavity (MC) at 668 nm. This sequence was selected to improve the reflectance percentage keeping the cavity depth. Clearly, the PA signal shows the formation of each HL pair of layers and the defective layer. Likewise, in this stack, the sequence after the formation of defective layers is inverted, and it is appreciable in PA amplitude signal. In both OMCs the PA amplitude is sensitive to the photonic gap formation which is evidenced by the quickly signal attenuation.

Figure 4.9 shows the reflectance spectrum of each OMC manufactured. Figure 4.9 (a) corresponds to OMC1, and it is well appreciable the formation of two MC located at 649 and 783 nm with an FWHM about 27 and 32 nm respectively, that corresponds to a relatively high Q-factor. A shift of 1 and 4 nm was produced of each MC compared with the simulation design, respectively. Figure 4.9 (b) corresponds to OMC2 and the MC is located at 672 nm, this means that a red-shift of 4 nm was produced compared with the designed one. Moreover, the sequence of OMC2 improved the Q-factor whose FWHM is 16 nm. In both OMCs, a diminution is observed in the depth of the OM that is caused by the interface roughness of the stack. [54]

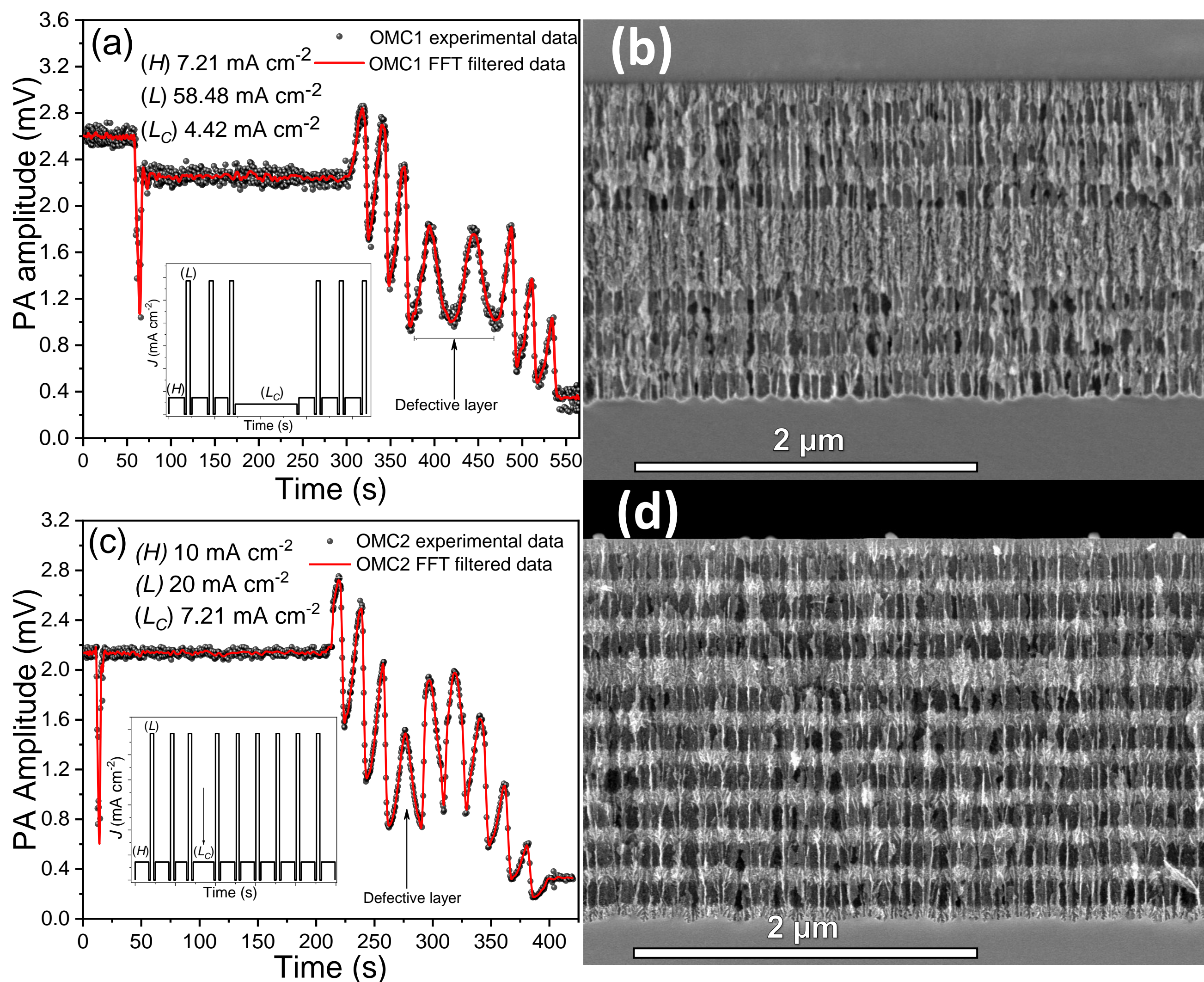

Figure 4.8: PA amplitude during OMC fabrication. (a) OMC1, (c) OMC2, and its respective SEM cross-section images (b) and (d). Inset in (a) and (c) shows the current density profile used.

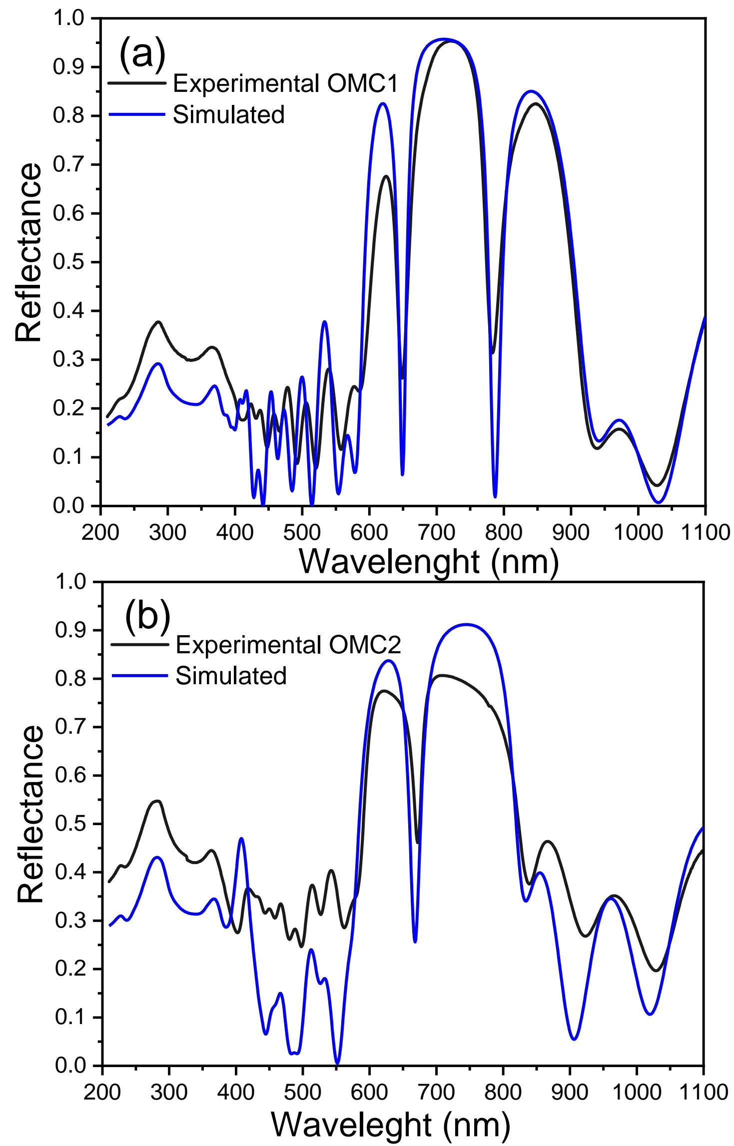

Figure 4.9: Reflectance spectra simulated (blue line) and measured (black line) of (a)OMC1 and (b)OMC2

4.4. Tolerance fabrication

The etching rate of c-Si in HF-based media was not constant for long etching times,[22, 20] and the films presented porosity gradients as a function of depth [12, 24]. Also, the electrolyte composition changed because of the chemical species released during the etching.[9] Furthermore, the silicon-electrolyte interface presented an inherent capacitance[118] that could store enough charge to continue the etch even if the current supply was off. This effect produced layers thicker than the designed ones and generated a red-shifted in the reflectance spectrum. This effect can be reduced if the current density decreases monotonously as a function of the time to compensate the remnant charges. Another alternative is to reduce the etching time. Nevertheless, in this work, and others related, PSi optical devices always presented deviations respect to the design ones. This is mainly attributed to the substrate quality and random fluctuations during the PSi formation. Hence, it is introduced the tolerance fabrication as a term related to the possible deviations of the optical response of the devices. In this work, we found a red-shift in DRBs about 30 nm associated with layers ticker than the designed ones. In this case, the average reflectance shift was the layer thickness deviation times the refractive index. In the case of OMCs, the main effect was observed in the Q factor that is affected by the interface roughness. Several works have reported PhCs based on PSi in the infrared region, which means that the thickness of the layers (optical path) is higher than those for PhC in the visible spectrum as is our case. Thus, deviations in layer thickness because of the intrinsic capacitance has more height on the optical response for the PhC designed in the visible region, usually a red-shift.

CHAPTER 5

Conclusions

This thesis is a systematic study of the optical properties of porous silicon (PSi) obtained from heavy doped p-type crystalline silicon <100> oriented. It is implemented a differential photoacoustic cell coupled to an electrochemical one for monitoring and controlling the etching. This technique allows the study of reaction kinetics and Psi formation process. Despite that, it was found that PSi formation is critically depended on the called substrate quality. It was proved that Si wafers are nonelectrical and nonthermal homogeneous due to nonuniform carrier distribution along the wafers. In the case of p-type Si, boron atoms trend to out-diffusion, this means that particles migrate from the center of the wafer to the boundary. This behavior was observed using photocarrier radiometry (PCR) imaging. This result establishes the methodology to characterize the substrate quality before silicon etching.

This work also studied the optical properties of PSi single films through reflectance measurements. This determination represents an inverse problem that was boarded from the optimization perspective. For that, it was implementing an optimization procedure based on evolutionary algorithms allowing the simultaneous determination of morphological parameters such as film thickness, interface roughness, and porosity, and the optical constants (refractive index and extinction coefficient). Clearly, this methodology requires an effective description of the optical and electrical behavior of a porous material like a mixture between the host material (Si) and the filling material (some fluid). There are different

rules for the electrical description of a mixture such as Maxwell-Garnet, Bruggeman, and Looyenga. In this work, it was proved the above-mentioned rules, and the one that presents better accuracy (best fit to the experimental data) is the effective medium approximation of Looyenga. Also, it is important to mention that PSi presents anisotropic optical properties meaning that this description is only valid in the near specular reflectance regimen where electromagnetic radiation propagation is parallel to the porous orientation.

The great understanding of etching kinetics and optical properties of PSi as a function of anodization conditions allows the design of customized devices such as photonic crystals. A remarkable feature of etching kinetics of silicon is the self-limiting etching. It means the continuous passivation of the porous films that allows the formation of new ones without considerable changes in the last ones formed. This is the principle to manufacture layered system or stacks of different porosity's. Additionally, crystalline silicon gets a regimen of constant values of optical constants from 1100 nm to 500 nm that lets design and manufacture good quality PhC in this range. Previous works had reported manufacture PSi PhCs in the infrared range, and it is understandable because the optical path required for that is mostly big. A considerable challenge is to fabricate distributed Bragg reflector (DBR) or optical microcavities (OMC) in the visible and near to the blue, but it requires every time shorter optical paths. So the control in the etching processes has to be more subtle. In situ monitoring allows that, and in the case of optical interferometry and photoacoustic, the precision is related with the wavelength used for the follow-up. Shorter wavelengths allow more accuracy in the PSi film thickness.

In the case of photoacoustic monitoring, the amplitude signal is periodic as a function of the time, and it is related to the etching rate of the PSi film. This means that the etching rate can be associated with the period (or frequency) of the signal. So, it is possible to design a specific PA amplitude profile that corresponds to defined multilayered PSi structure allowing control of the PSi formation. Starting from this point, this work finally presents a systematic methodology to design, fabricate, and characterize a PSi customized stacks. Remarkable facts to take into account are related to the substrate quality, electrolyte composition, and temperature control. This methodology was proved to fabricate five (5) PhCws with different properties (stop band, bandwidth, defective layers) that behaves in good agreement with the simulations. Despite that, it observed deviations from the simula-

tions that are related to random fluctuations during the PSi formation. These discrepancies are considered in a tolerance range fabrication. The average differences in all manufactured devices are around 30 nm in the spectral position. Finally, the methodology report in this thesis allows design, fabricate and characterize PSi PhC «*à la carte*» in the range of 500 to 1100 nm.

With thin film deposition becoming increasingly critical in the production of advanced electronic and optical devices it is required characterizing phenomena that take place at surfaces and interfaces during thin films formations. Most of the manufacture devices of these days are made without any real time monitoring and controlling. The photoacoustic methodology present in this work can be extrapolated to other systems with similar formation process (layered structures) whether physical or chemical, such as spin coating, chemical vapor deposition, epitaxy, sputtering.

References

[1] H. Looyenga. Dielectric constants of heterogeneous mixtures. *Physica*, 31(3):401 – 406, 1965.

[2] T. C. Choy. *Effective Medium Theory Principles and Applications*, pages 1–24. Oxford University Press, 2 edition, 2016.

[3] E. Yablonovitch. Photonic crystals. *Journal of Modern Optics*, 41(2):173–194, 1994.

[4] Plinio Innocenzi, Luca Malfatti, and Galo J. A. A. Soler-Illia. Hierarchical mesoporous films: From self-assembly to porosity with different length scales. *Chemistry of Materials*, 23(10):2501–2509, 2011.

[5] Hakan Inan, Muhammet Poyraz, Fatih Inci, Mark A. Lifson, Murat Baday, Brian T. Cunningham, and Utkan Demirci. Photonic crystals: emerging biosensors and their promise for point-of-care applications. *Chem. Soc. Rev.*, 46:366–388, 2017.

[6] Jacobo Hernandez-Montelongo, Alvaro Muñoz-Noval, Josefa García-Ruíz, Vicente Torres-Costa, Raul Martin-Palma, and Miguel Manso-Silvan. Nanostructured porous silicon: The winding road from photonics to cell scaffolds. a review. *Frontiers in Bioengineering and Biotechnology*, 3:60, 2015.

[7] Jonathan Rasson, Olivier Poncelet, Sébastien R. Mouchet, Olivier Deparis, and Laurent A. Francis. Vapor sensing using a bio-inspired porous silicon photonic crystal. *Materials Today: Proceedings*, 4(4, Part A):5006 – 5012, 2017.

[8] Shuren Hu, Marwan Khater, Rafael Salas-Montiel, Ernst Kratschmer, Sebastian Engelmann, William Green, and Sharon M. Weiss. Experimental realization of deep-

subwavelength confinement in dielectric optical resonators. *Science Advances*, 4(8), 2018.

[9] H. Föll, M. Christophersen, J. Carstensen, and G. Hasse. Formation and application of porous silicon. *Materials Science and Engineering: R: Reports*, 39(4):93–141, 2002.

[10] Kurt W. Kolasinski. Etching of silicon in fluoride solutions. *Surf. Sci.*, 603(10):1904 – 1911, 2009.

[11] Christian R. Ocier, Neil A. Krueger, Weijun Zhou, and Paul V. Braun. Tunable visibly transparent optics derived from porous silicon. *ACS Photonics*, 4(4):909–914, 2017.

[12] Danilo R. Huanca, Francisco J. Ramirez-Fernandez, and Walter J. Salcedo. Porous silicon optical cavity structure applied to high sensitivity organic solvent sensor. *Microelectronics Journal*, 39(3):499 – 506, 2008. The Sixth International Conference on Low Dimensional Structures and Devices.

[13] Padmavati Sahare, Marcela Ayala, Rafael Vazquez-Duhalt, and Vivechana Agrawal. Immobilization of peroxidase enzyme onto the porous silicon structure for enhancing its activity and stability. *Nanoscale Research Letters*, 9(1):409, Aug 2014.

[14] Marta Martin, Laurent Massif, Elias Estephan, Mari-Belle Saab, Thierry Cloitre, Csilla Gergely, Frédéric J. G. Cuisinier, Christian Larroque, Vivechana Agarwal, and Guy Le Lay. Effect of surface functionalization of porous silicon microcavities on biosensing performance. *Journal of Nanophotonics*, 6(1):1 – 12, 2012.

[15] Thuy Chi Do, Huy Bui, Thuy Van Nguyen, The Anh Nguyen, Thanh Hai Nguyen, and Van Hoi Pham. A microcavity based on a porous silicon multilayer. *Adv. Nat. Sci: Nanosci. Nanotechnol*, 2(3):035001, 2011.

[16] Claudia Pacholski. Photonic crystal sensors based on porous silicon. *Sensors*, 13(4):4694–4713, 2013.

[17] A. Venkateswara Rao, F. Ozanam, and J. N. Chazalviel. In situ fourier-transform electromodulated infrared study of porous silicon formation: Evidence for solvent effects on the vibrational linewidths. *J. Electrochem. Soc.*, 138(1):153–159, 1991.

[18] Elin Steinsland, Terje Finstad, and Anders Hanneborg. Laser reflectance interferometry for in situ determination of silicon etch rate in various solution. *Journal of The Electrochemical Society*, 146(10):3890–3895, 1999.

[19] S. E. Foss, P. Y. Y. Kan, and T. G. Finstad. Single beam determination of porosity and etch rate in situ during etching of porous silicon. *J. Appl. Phys.*, 97(11):114909, 2005.

[20] C. F. Ramirez-Gutierrez, J. D. Castaño-Yepes, and M. E. Rodriguez-Garcia. Optical interferometry and photoacoustics as in-situ techniques to characterize the porous silicon formation: a review. *Open Material Sciences*, 4(1):23–32, 2018.

[21] C. F. Ramirez-Gutierrez, J. D. Castaño-Yepes, and M. E. Rodriguez-García. In situ photoacoustic characterization for porous silicon growing: Detection principles. *J. Appl. Phys.*, 119:185103, 2016.

[22] C. F. Ramirez-Gutierrez, J. D. Castaño-Yepes, and M. E. Rodriguez-García. Modeling the photoacoustic signal during the porous silicon formation. *J. Appl. Phys.*, 121(2):025103, 2017.

[23] Hanna H. Hulkkonen, Turkka Salminen, and Tapio Niemi. Block copolymer patterning for creating porous silicon thin films with tunable refractive indices. *ACS Applied Materials & Interfaces*, 9(37):31260–31265, 2017.

[24] Jaime Caballero-Hernández, Vanda Godinho, Bertrand Lacroix, Maria C. Jiménez de Haro, Damien Jamon, and Asunción Fernández. Fabrication of optical multilayer devices from porous silicon coatings with closed porosity by magnetron sputtering. *ACS Applied Materials & Interfaces*, 7(25):13889–13897, 2015.

[25] R. Nava, M. B. de la Mora, J. Tagüeña-Martínez, and J. A. del Río. Refractive index contrast in porous silicon multilayers. *physica status solidi c*, 6(7):1721–1724, 2009.

[26] D. Estrada-Wiese and J. A. del Río. Refractive index evaluation of porous silicon using bragg reflectors. *Rev. Mex. Fis.*, 64:72–81, 2018.

[27] G. Vincent. Optical properties of porous silicon superlattices. *J. Appl. Phys.*, 64(18):2367–2369, 1994.

[28] L Pavesi and P Dubos. Random porous silicon multilayers: application to distributed bragg reflectors and interferential fabry - pérot filters. *Semicond. Sci. Technol.*, 12(5):570, 1997.

[29] S. Setzu, P. Ferrand, and R. Romestain. Optical properties of multilayered porous silicon. *Mater. Sci. Eng. B.*, 69-70:34–42, 2000.

[30] Han Jung Kim, Young You Kim, and Ki Won Lee. Multiparametric sensor based on dbr porous silicon for detection of ethanol gas. *Curr. Appl. Phys.*, 10(1):181 – 183, 2010.

[31] Wan Ting Tsai, Minh Hang Nguyen, Jian Ren Lai, Hai Binh Nguyen, Ming Chang Lee, and Fan Gang Tseng. ppb-level heavy metal ion detection by electrochemistry-assisted nanoporous silicon (eca-nps) photonic sensors. *Sens. Actuator B-Chem.*, 265:75 – 83, 2018.

[32] Raffaele Caroselli, David Martín Sánchez, Salvador Ponce Alcántara, Francisco Prats Quilez, Luis Torrijos Morán, and Jaime García-Rupérez. Real-time and in-flow sensing using a high sensitivity porous silicon microcavity-based sensor. *Sensors*, 17(12), 2017.

[33] D. Estrada-Wiese, J.A. del Río, R. Nava, J. Gómez-Ocampo, J. Tagüeña-Martínez, and Z. Montiel-González. Staggered padé wavelength distribution for multi-bragg photonic mirrors. *Solar Energy Materials and Solar Cells*, 141:315 – 321, 2015.

[34] M.B. de la Mora, O.A. Jaramillo, R. Nava, J. Tagüeña-Martínez, and J.A. del Río. Viability study of porous silicon photonic mirrors as secondary reflectors for solar concentration systems. *Solar Energy Materials and Solar Cells*, 93(8):1218 – 1224, 2009.

[35] Diederik S. Wiersma. Disordered photonics. *Nature Photonics*, 7:188 – 196, 2013.

[36] Michele Bellingeri, Ilka Kriegel, and Francesco Scotognella. One dimensional disordered photonic structures characterized by uniform distributions of clusters. *Optical Materials*, 39:235 – 238, 2015.

[37] Michele Bellingeri, Alessandro Chiasera, Ilka Kriegel, and Francesco Scotognella. Optical properties of periodic, quasi-periodic, and disordered one-dimensional photonic structures. *Optical Materials*, 72:403 – 421, 2017.

[38] A. A. Abouelsaood, M. Y. Ghannam, L. Stalmans, J. Poortmans, and J. F. Nijs. Experimental testing of a random medium optical model of porous silicon for photovoltaic applications. *Progress in Photovoltaics: Research and Applications*, 9(1):15–26, 2001.

[39] M. E. Rodriguez, A. Mandelis, G. Pan, L. Nicolaides, J. A. Garcia, and Y. Riopel. Computational aspects of laser radiometric multiparameter fit for carrier transport property measurements in si wafers. *Journal of The Electrochemical Society*, 147(2):687, 2000.

[40] M. E. Rodríguez, A. Mandelis, G. Pan, J. A. García, V. Gorodokin, and Y. Raskin. Minority carrier lifetime and iron concentration measurements on p-si wafers by infrared photothermal radiometry and microwave photoconductance decay. *J. Appl. Phys.*, 87(11):8113–8121, 2000.

[41] Cristian F. Ramirez-Gutierrez, Andrés Medina-Herrera, Liliana Tirado-Mejía, Luis F. Zubieta-Otero, Orlando Auciello, and Mario E. Rodriguez-Garcia. Photoluminescence study of porous p-type silicon: Identification of radiative transitions. *J. Lumin.*, 201:11 – 17, 2018.

[42] Pavlo Lishchuk, Mykola Isaiev, Liubov Osminkina, Roman Burbelo, Tetyana Nychyporuk, and Victor Timoshenko. Photoacoustic characterization of nanowire arrays formed by metal-assisted chemical etching of crystalline silicon substrates with different doping level. *Physica E: Low-dimensional Systems and Nanostructures*, 107:131 – 136, 2019.

[43] Xing-Da Liu, Zhi-Ling Hou, Bao-Xun Zhang, Ke-Tao Zhan, Peng He, Kai-Lun Zhang, and Wei-Li Song. A general model of dielectric constant for porous materials. *Applied Physics Letters*, 108(10):102902, 2016.

[44] Bincheng Li, Derrick Shaughnessy, Andreas Mandelis, Jerias Batista, and Jose Garcia. Accuracy of photocarrier radiometric measurement of electronic transport properties of ion-implanted silicon wafers. *J. Appl. Phys.*, 96(1):186–196, 2004.

[45] Andreas Mandelis. Photo-carrier radiometry of semiconductors: A novel powerful optoelectronic diffusion-wave technique for silicon process non-destructive evaluation. *NDT and E Int.*, 39(3):244 – 252, 2006.

[46] J. A. Garcia, X. Guo, A. Mandelis, and A. Simmons. Photo-carrier-radiometry (pcr) metrology for semiconductor manufacturing inspection. *AIP Conference Proceedings*, 788(1):625–627, 2005.

[47] A. Gutiérrez, M.E. Rodríguez-García, and J. Giraldo. Photoelectronic characterization of n-type silicon wafers using photocarrier radiometry. *Physica B Condens. Matter*, 406(19):3687 – 3693, 2011.

[48] A. Uhlir Jr. Electrolytic shaping of germanium and silicon. *Bell System Technical Journal*, 35(2):333–347, 1956.

[49] Dennis R. Turner. Electropolishing silicon in hydrofluoric acid solutions. *Journal of The Electrochemical Society*, 105(7):402–408, 1958.

[50] Takashi Unagami. Oxidation of porous silicon and properties of its oxide film. *Japanese Journal of Applied Physics*, 19(2):231–241, 1980.

[51] L. T. Canham. Silicon quantum wire array fabrication by electrochemical and chemical dissolution of wafers. *Applied Physics Letters*, 57(10):1046–1048, 1990.

[52] C. Pickering, M.I.J. Beale, D.J. Robbins, P.J. Pearson, and R. Greef. Optical properties of porous silicon films. *Thin Solid Films*, 125(1):157 – 163, 1985.

[53] M G Berger, C Dieker, M Thonissen, L Vescan, H Luth, H Munder, W Theiss, M Wernke, and P Grosse. Porosity superlattices: a new class of si heterostructures. *Journal of Physics D: Applied Physics*, 27(6):1333–1336, 1994.

[54] I. A. Lujan-Cabrera, C. F. Ramirez-Gutierrez, J. D. Castaño-Yepes, and M. E. Rodriguez-Garcia. Effects of the interface roughness in the optical response of one-dimensional photonic crystals of porous silicon. *Physica B: Condensed Matter*, 560:133 – 139, 2019.

[55] C. Mazzoleni and L. Pavesi. Application to optical components of dielectric porous silicon multilayers. *Applied Physics Letters*, 67(20):2983–2985, 1995.

[56] Lorenzo Pavesi, Claudio Mazzoleni, Alessandro Tredicucci, and Vittorio Pellegrini. Controlled photon emission in porous silicon microcavities. *Applied Physics Letters*, 67(22):3280–3282, 1995.

[57] Marion Thust, M J Schöning, S Frohnhoff, R Arens-Fischer, P Kordos, and H Lüth. Porous silicon as a substrate material for potentiometric biosensors. *Measurement Science and Technology*, 7(1):26–29, 1996.

[58] Victor S.-Y. Lin, Kianoush Motesharei, Keiki-Pua S. Dancil, Michael J. Sailor, and M. Reza Ghadiri. A porous silicon-based optical interferometric biosensor. *Science*, 278(5339):840–843, 1997.

[59] Nobuaki Noguchi and Ikuo Suemune. Luminescent porous silicon synthesized by visible light irradiation. *Applied Physics Letters*, 62(12):1429–1431, 1993.

[60] É Vázsonyi, E Szilágyi, P Petrik, Z.E Horváth, T Lohner, M Fried, and G Jalsovszky. Porous silicon formation by stain etching. *Thin Solid Films*, 388(1):295 – 302, 2001.

[61] Emily J. Anglin, Lingyun Cheng, William R. Freeman, and Michael J. Sailor. Porous silicon in drug delivery devices and materials. *Advanced Drug Delivery Reviews*, 60(11):1266 – 1277, 2008.

[62] V. Lehmann and U. Gösele. Porous silicon formation: A quantum wire effect. *Applied Physics Letters*, 58(8):856–858, 1991.

[63] M. J. Sailor. *Porous Silicon in Practice*, page 14. Wiley-VCH Verlag GmbH & Co. KGaA, 2011.

[64] R. L. Smith and S. D. Collins. Porous silicon formation mechanisms. *Journal of Applied Physics*, 71(8):R1–R22, 1992.

[65] D. A. G. Bruggeman. Berechnung verschiedener physikalischer konstanten von heterogenen substanzen. i. dielektrizitätskonstanten und leitfähigkeiten der mischkörper aus isotropen substanzen. *Annalen der Physik*, 416(7):636–664, 1935.

[66] Vadim A. Markel. Introduction to the maxwell garnett approximation: tutorial. *J. Opt. Soc. Am. A*, 33(7):1244–1256, 2016.

[67] M. Itano, F. W. Kern, M. Miyashita, and T. Ohmi. Particle removal from silicon wafer surface in wet cleaning process. *IEEE Transactions on Semiconductor Manufacturing*, 6(3):258–267, 1993.

[68] Werner Kern. The evolution of silicon wafer cleaning technology. *Journal of The Electrochemical Society*, 137(6):1887–1892, 1990.

[69] Diego Germán Espinosa-Arbeláez, Rubén Velázquez-Hernández, Julio Petricioli-Carranco, Rafael Quintero-Torres, and Mario Enrique Rodríguez-García. Differential photoacoustic cell to study the wetting process during porous silicon formation. *physica status solidi c*, 8(6):1856–1859, 2011.

[70] L. Sánchez-Cano, R.and Tirado-Mejía, G. Fonthal, H. Ariza-Calderón, and N. Porras-Montenegro. Exciton recombination energy in spherical quantum dots on GaInAsSb-GaSb grown by liquid-phase epitaxy. *Journal of Applied Physics*, 104(11):113706, 2008.

[71] Mario E. Rodriguez, J. A. Garcia, A. Mandelis, C. Jean, and Y. Riopel. Kinetics of surface-state laser annealing in si by frequency-swept infrared photothermal radiometry. *Applied Physics Letters*, 74(17):2429–2431, 1999.

[72] Andreas Mandelis, Jerias Batista, and Derrick Shaughnessy. Infrared photocarrier radiometry of semiconductors: Physical principles, quantitative depth profilometry, and scanning imaging of deep subsurface electronic defects. *Phys. Rev. B*, 67:205208, 2003.

[73] Allan Rosencwaig and Allen Gersho. Theory of the photoacoustic effect with solids. *Journal of Applied Physics*, 47(1):64–69, 1976.

[74] C. L. Mitsas and D. I. Siapkas. Generalized matrix method for analysis of coherent and incoherent reflectance and transmittance of multilayer structures with rough surfaces, interfaces, and finite substrates. *Appl. Opt.*, 34(10):1678–1683, 1995.

[75] C. Tsai, K. H. Li, J. C. Campbell, B. K. Hance, M. F. Arendt, J. M. White, S. L. Yau, and A. J. Bard. Effects of illumination during anodization of porous silicon. *Journal of Electronic Materials*, 21(10):995–1000, 1992.

[76] M. D. Dramićanin, P. M. Nikolić, Z. D. Ristovski, D. G. Vasiljević, and D. M. Todorović. Photoacoustic investigation of transport in semiconductors: Theoretical and experimental study of a ge single crystal. *Phys. Rev. B*, 51:14226–14232, 1995.

[77] Martin A. Green and Mark J. Keevers. Optical properties of intrinsic silicon at 300 k. *Progress in Photovoltaics: Research and Applications*, 3(3):189–192, 1995.

[78] Zhiliang Chen, Tzung-Yin Lee, and Gijs Bosman. Electrical band gap of porous silicon. *Applied Physics Letters*, 64(25):3446–3448, 1994.

[79] Charalambos C. Katsidis and Dimitrios I. Siapkas. General transfer-matrix method for optical multilayer systems with coherent, partially coherent, and incoherent interference. *Appl. Opt.*, 41(19):3978–3987, 2002.

[80] G. Amato, G. Benedetto, R. Spagnolo, and M. Turnaturi. Photoacoustic measurements of doped silicon wafers. *physica status solidi (a)*, 114(2):519–523, 1989.

[81] A. Salnick, A. Mandelis, F. Funak, and C. Jean. Monitoring of ion implantation in si with carrier plasma waves using infrared photothermal radiometry. *Applied Physics Letters*, 71(11):1531–1533, 1997.

[82] A. Pinto Neto, H. Vargas, N. F. Leite, and L. C. M. Miranda. Photoacoustic characterization of semiconductors: Transport properties and thermal diffusivity in gaas and si. *Phys. Rev. B*, 41:9971–9979, 1990.

[83] M. G. Burzo, P. L. Komarov, and P. E. Raad. Non-contact thermal conductivity measurements of p-doped and n-doped gold covered natural and isotopically-pure silicon and their oxides. In *5th International Conference on Thermal and Mechanical Simulation and Experiments in Microelectronics and Microsystems, 2004. EuroSimE 2004. Proceedings of the*, pages 269–276, 2004.

[84] J. C. Dixon. *Appendix B: Properties of Air*, pages 375–378. John Wiley and Sons, Ltd, 2007.

[85] Guo Chun, Kong Mingdong, Gao Weidong, and Li Bincheng. Simultaneous determination of optical constants, thickness, and surface roughness of thin film from spectrophotometric measurements. *Opt. Lett.*, 38(1):40–42, 2013.

[86] V. Torres-Costa, R. J. Martín-Palma, and J. M. Martínez-Duart. Optical constants of porous silicon films and multilayers determined by genetic algorithms. *Journal of Applied Physics*, 96(8):4197–4203, 2004.

[87] Pornchai Bumroongsri and Soorathep Kheawhom. Simultaneous estimation of thin film thickness and optical properties using two-stage optimization. *J. Global Optim.*, 54(3):583–597, Nov 2012.

[88] Ernesto G. Birgin, Ivan E. Chambouleyron, and Sergio D. Martínez, José Mario and. Ventura. Estimation of optical parameters of very thin films. *Applied Numerical Mathematics*, 47(2):109 – 119, 2003.

[89] C.F. Ramirez-Gutierrez, J.C. Mosquera-Mosquera, and M.E. Rodríguez-García. Study of percolation and modeling of the order–disorder transition for zincblende–diamond structures: Percolation and the existence of a unique band of events. *Computational Condensed Matter*, 1:58– 64, 2014.

[90] C. Peña and J. Torres. Calculation of optical constants in porous silicon thin films using diffused and specular reflectance measurement. *Surf. Rev. Lett.*, 09(05n06):1821–1825, 2002.

[91] Nalin H. Maniya, Sanjaykumar R. Patel, and Z.V.P. Murthy. Simulation and fabrication study of porous silicon photonic crystal. *Optik*, 125(2):828 – 831, 2014.

[92] George C. John and Vijay A. Singh. Self-organization in porous silicon formation. *Phys. Rev. B*, 56:4638–4641, 1997.

[93] Shervin Keshavarzi, Ulrich Mescheder, and Holger Reinecke. Formation mechanisms of self-organized needles in porous silicon based needle-like surfaces. *J. Electrochem. Soc.*, 165(3):E108–E114, 2018.

[94] G. Lérondel, R. Romestain, and S. Barret. Roughness of the porous silicon dissolution interface. *J. Appl. Phys.*, 81(9):6171–6178, 1997.

[95] J. Charrier, V. Alaiwan, P. Pirasteh, A. Najar, and M. Gadonna. Influence of experimental parameters on physical properties of porous silicon and oxidized porous silicon layers. *Appl. Surf. Sci.*, 253(21):8632 – 8636, 2007.

[96] St. Frohnhoff, M.G. Berger, M. Thönissen, C. Dieker, L. Vescan, H. Münder, and H. Lüth. Formation techniques for porous silicon superlattices. *Thin Solid Films*, 255(1):59 – 62, 1995.

[97] A. G. Cullis, L. T. Canham, and P. D. J. Calcott. The structural and luminescence properties of porous silicon. *Journal of Applied Physics*, 82(3):909–965, 1997.

[98] L. H. Lin, X. Z. Sun, R. Tao, Z. C. Li, J. Y. Feng, and Z. J. Zhang. Photoluminescence origins of the porous silicon nanowire arrays. *Journal of Applied Physics*, 110(7):073109, 2011.

[99] F. Koch, V. Petrova-Koch, and T. Muschik. The luminescence of porous si: the case for the surface state mechanism. *Journal of Luminescence*, 57(1):271 – 281, 1993.

[100] Jeffrey M. Lauerhaas and Michael J. Sailor. Chemical modification of the photoluminescence quenching of porous silicon. *Science*, 261(5128):1567–1568, 1993.

[101] Michael J. Sailor and Elizabeth C. Wu. Photoluminescence-based sensing with porous silicon films, microparticles, and nanoparticles. *Advanced Functional Materials*, 19(20):3195–3208, 2009.

[102] W. E. Carlos and S. M. Prokes. The ex defect center in porous silicon. *Journal of Applied Physics*, 78(3):2129–2131, 1995.

[103] Qianqian Yu, Haiping He, Lu Gan, and Zhizhen Ye. The defect nature of photoluminescence from a porous silicon nanowire array. *RSC Adv.*, 5:80526–80529, 2015.

[104] Amir Saar. Photoluminescence from silicon nanostructures: The mutual role of quantum confinement and surface chemistry. *Journal of Nanophotonics*, 3(1):1 – 42 – 42, 2009.

[105] X. G. Zhang. Morphology and formation mechanisms of porous silicon. *Journal of The Electrochemical Society*, 151(1):C69–C80, 2004.

[106] Leszek Bychto, Maria Balaguer, Ester Pastor, Vladimir Chirvony, and Eugenia Matveeva. Influence of preparation and storage conditions on photoluminescence of porous silicon powder with embedded si nanocrystals. *Journal of Nanoparticle Research*, 10(8):1241–1249, 2008.

[107] Cary M. Hayner, Xin Zhao, and Harold H. Kung. Materials for rechargeable lithium-ion batteries. *Annual Review of Chemical and Biomolecular Engineering*, 3(1):445–471, 2012.

[108] Jeong K. Lee, Kurt B. Smith, Cary M. Hayner, and Harold H. Kung. Silicon nanoparticles–graphene paper composites for li ion battery anodes. *Chemical Communications.*, 46:2025–2027, 2010.

[109] A. Magasinski, P. Dixon, B. Hertzberg, A. Kvit, J. Ayala, and G. Yushin. High-performance lithium-ion anodes using a hierarchical bottom-up approach. *Nature Materials*, 9:353–358, 2010.

[110] Yin-Wei Cheng, Chi-Kai Lin, Yueh-Chieh Chu, Ali Abouimrane, Zonghai Chen, Yang Ren, Chuan-Pu Liu, Yonhua Tzeng, and Orlando Auciello. Electrically conductive ultrananocrystalline diamond-coated natural graphite-copper anode for new long life lithium-ion battery. *Advanced Materials*, 26(22):3724–3729, 2014.

[111] V.M. Dubin, F. Ozanam, and J.-N. Chazalviel. In situ infrared spectroscopic study of luminescent porous silicon. *Vibrational Spectroscopy*, 8(2):159 – 166, 1995. 6th Austrian-Hungarian International Conference on Vibrational Spectroscopy.

[112] C. F. Ramirez-Gutierrez, J. D. Castaño-Yepes, and M. E. Rodriguez-García. Porosity and roughness determination of porous silicon thin films by genetic algorithms. *Optik*, 173:271 – 278, 2018.

[113] Claudia Pacholski, Marta Sartor, Michael J. Sailor, Frédérique Cunin, and Gordon M. Miskelly. Biosensing using porous silicon double-layer interferometers: Reflective interferometric fourier transform spectroscopy. *Journal of the American Chemical Society*, 127(33):11636–11645, 2005.

[114] Robert A. Smith. *Fluorine Compounds, Inorganic, Hydrogen*, pages 1–26. American Cancer Society, 2003.

[115] Andrea Edit Pap, Krisztián Kordás, Jouko Vähäkangas, Antti Uusimäki, Seppo Leppävuori, Laurent Pilon, and Sándor Szatmári. Optical properties of porous silicon. part iii: Comparison of experimental and theoretical results. *Optical Materials*, 28(5):506 – 513, 2006.

[116] Martin A. Green. Self-consistent optical parameters of intrinsic silicon at 300k including temperature coefficients. *Solar Energy Materials and Solar Cells*, 92(11):1305 – 1310, 2008.

[117] T Starkey and P. Vukusic. Light manipulation principles in biological photonic systems. *Nanophotonics*, 2(4):289 – 307, 2013.

[118] Ronald L. Meek. n+ silicon-electrolyte i nterface capacitance. *Surface Science*, 25(3):526 – 536, 1971.

[119] A. S. Mogoda and Y. H. Ahmad. Electrochemical impedance study of porous silicon prepared by metal-assisted chemical etching. *Silicon*, 2019.

Appendix A

In situ Photoacoustic signals from calibration series

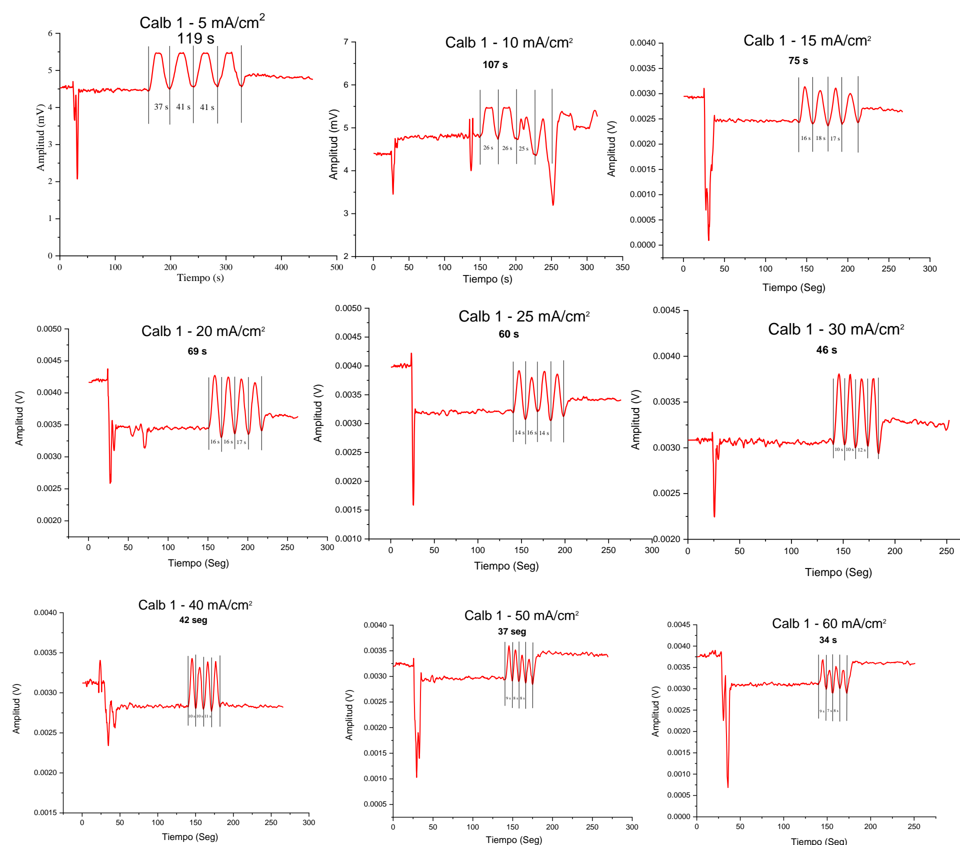

Figure A.1: PA amplitude of the calibration series. Anodization current density from 5 mA cm^{-2} to 60 mA cm^{-2}

Appendix B

UV-Vis spectra of calibration series

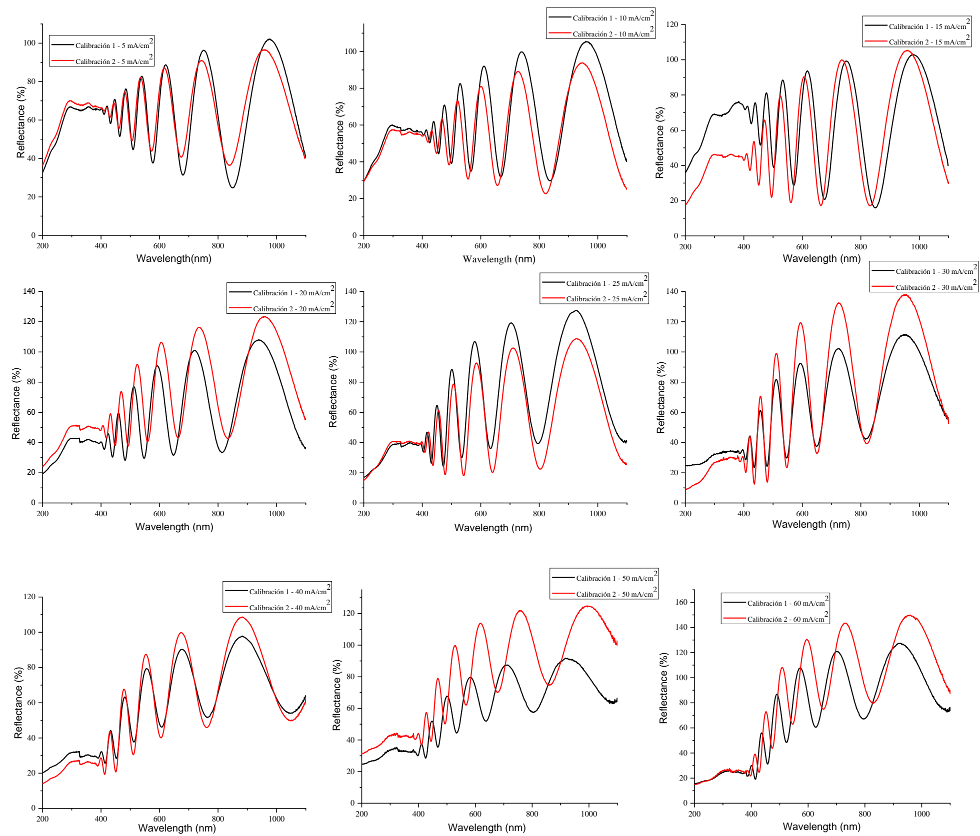

Figure B.1: UV-Vis reflectance spectrum of the calibration series. Anodization current density from 5 mA cm^{-2} to 60 mA cm^{-2}

Appendix C

Effects of the interface roughness in the optical response of one-dimensional photonic crystals

A single PSi layer and PSi DBRs centered about $\lambda_0 = 700$ nm were designed and simulated with the features shown in table C.1. Also, in the same table, a high refractive index layer is noted as H, the low refractive index layer with L, and the c-Si substrate like S. This notation allows to write the sequence of layers of the heterostructure designed.

Four cases were studied. The first corresponds to a single PSi layer over a c-Si substrate with the roughness contribution in the interface PSi/c-Si. The other examples are PSi DBRs where roughness contributions where located at different interfaces. DBR1 is the case where the rough interface is located between the air and the first layer of the DBR (H), so this interface is called Air/DBR. In the sample DBR2 roughness contribution is located along all interfaces of DBR, this means at the interfaces H/L and L/H. Finally, DBR3 consider the roughness between the last L layer and the c-Si substrate, this interface is called DBR/c-Si. In all cases, the optical response is simulated as a function of the roughness values in the allowed range.

Table C.1: It shows the simulated values for the single layer PSi and the DBRs. Also, it contains the place where rough contribution is located and the sequence of the structure.

Structure	d_H (nm)	d_L (nm)	p_H	p_L	σ	sequence
Single PSi layer	450	–	0.66	–	PSi/c-Si	HS
DBR1	102	146	0.91	0.68	Air/DBR	$(HL)^{15}S$
DBR2	102	146	0.91	0.68	(H/L)	$(HL)^{15}S$
DBR3	102	146	0.91	0.68	DBR/c-Si	$(HL)^{15}S$

Numerical results

The optical response of PSi single layer and PhCs as a function of the RMS roughness are shown in Fig. C.1. Color bar represents the reflectance. The first case (Fig C.1(a)), shows the simulation of the reflectance of a single PSi layer over the c-Si substrate with 450 nm of thickness and $p = 0{,}66$ of porosity (see table C.1). This shows the change in the reflectance as a function of roughness interface PSi/c-Si the range of 210-1100 nm. The main effect is the loss of the intensity of the interference effect in visible and infrared regions. As it can be seen, the optical response in the UV region remains constant, this means that reflectance was not affected by roughness increasing at the substrate interface. This effect is produced due to the high absorption that PSi presents in the UV region, which causes the light to be absorbed first before reaching the PSi/c-Si interface. This effect can be observed in Fig. C.2(a) that shows the aspect ratio between a smooth single PSi layer and a rough one, whose is about 1 in the UV region.

For DBR1 sample, Fig C.1(b) where the rough interface is located at Air/DBR, the simulations were run from 0 to 50 nm in σ RMS value to be comparable with the thickness of the layers that compose the DBR. The noticeable effect is a decrease in the reflectance in the UV region, caused because the size of wavelength is of the same order of the surface irregularities placed in the first interface. Therefore, the radiation is scattered in random directions producing a reduction in the specular reflectance detected. Also, a part of the visible (400 to 650 nm) and infrared (800 to 1100 nm) are slightly scattered. The PhC bandgap is not affected considerable, and the reflectance remains constant for σ values

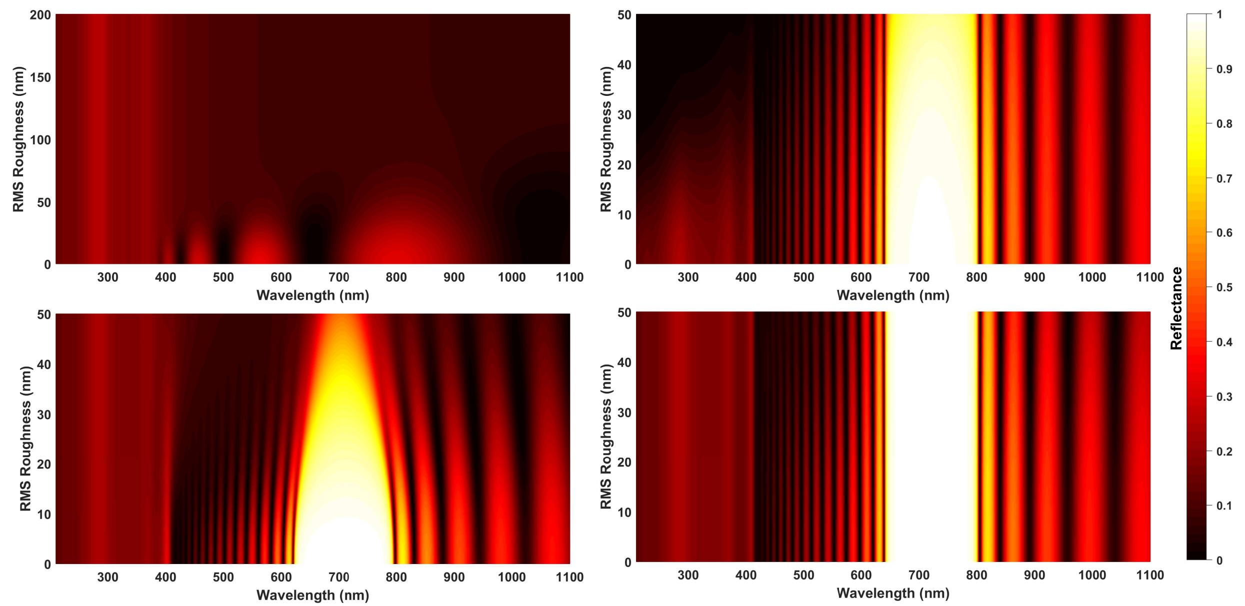

Figure C.1: Numerical results. (a) Single PSi layer with a roughness contribution in PSi/c-Si (substrate) interface. PSi DBR optical response with roughness contribution on: (b) Air/DBR interface, (c) DBR2 internal interfaces (H/L), and (d) DBR/c-Si (Substrate) interface.

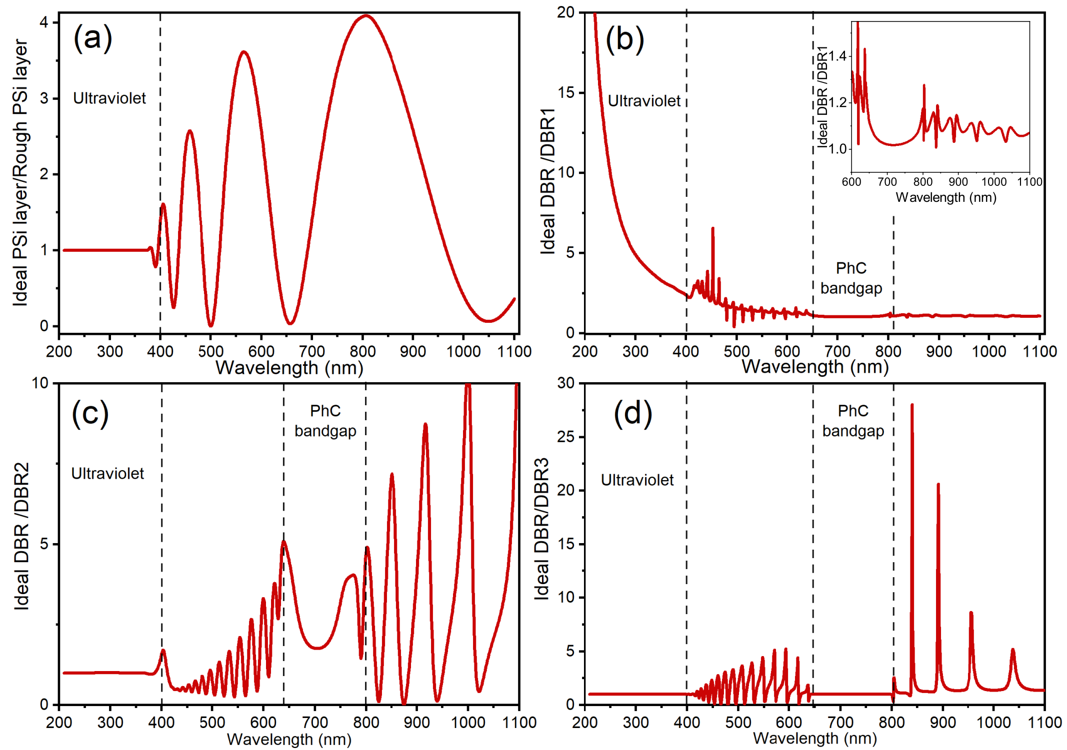

Figure C.2: Aspect ratio between ideal reflectance and the reflectance with roughness contributions for: (a) Single PSi layer case, (b) DBR1, (c) DBR2, and (d) DBR3.

under 20 nm. For values more significant than 20 nm, DRB1 exhibits a narrowing in the bandwidth, and a decrease of about 20 % is observed in the reflectance. Fig. C.2(b) shows this demeanor in the above-mentioned regions.

Now, the case of DBR2 whit roughness contribution at the interfaces H/L and L/H along the DBR is analyzed, Fig C.1(c) shows that reflectance in the UV region remains constant (see Fig. C.2(c)) because there is not any roughness contribution at the Air/DBR interface. The main effect is observed in the photonic bandgap, which gets (more and more) narrowed, and the reflectance intensity diminished as the roughness increases. This effect occurs because the wavelengths that satisfy the quarter-wave condition (Eq. **??**) start to be scattered and there is a loss in multiple reflections and interference that generate the photonic bandgap. The maximum reflectance in the bandgap goes from 0.93, for a smooth DBR to nearly 0.5 for a DBR with irregularities about 50 nm. Also, the irregularities along the 15 periods of the PhC have effects in the intensity of the interference fringes, even in the IR region as Fig. C.2 shows.

DBR3 is the case where roughness contribution is located at DBR/c-Si interface. Starting from the fact that there is no roughness contribution on the first or any of the H/L and L/H interfaces, the PhC bandgap is not disturbed, so the total response of the system is not affected for this roughness contribution. This behavior can be observed in Figs. C.1(d) and. C.2(d) where there are no changes in the UV and PhC bandgap regions. However, Fig. C.2(d) shows intensity variations in the interference fringes at both sides of PhC band gap. This means that these wavelengths reach to be scattered in the substrate interface.

On the other hand, this model and simulations can be done for other photonic systems such as DBRs with a defective layer or optical micro-cavities (OMC). In any case, the effects on the optical response will be similar, that is to say, that the intensity of defective mode will get affected by energy losses due to surface scattering and volume absorption.

Experimental Results

A PSi DBR was manufactured to perform the comparison between the simulations and the experimental system. Heavy boron doped c-Si (p^{++}) with [100] direction, and 0.005 Ω cm of resistivity were used as a substrate. Samples were cut into squares of 14×14 mm and cleaned using the RCA method. Etching was carried out in an electrolyte composed by hydrofluoric acid (HF) at 40 % and ethanol at 99.67 % in 3:7 volume ratio at 25 °C. It followed the etching procedure monitored by photoacoustics [20] to control the thickness of the layers. This methodology allows the fabrication of PSi layers with high accuracy in porosity and thickness. Anodization parameters are summarized in table C.2.

Table C.2: Etch conditions used for PSi DBR fabrication. SEM determined the layer thickness and roughness, and the porosity and refractive index calculated by fitting the UV-Vis spectrum.

Layer	ρ(mA/cm^2)	Etching time (s)	p	d	η(700 nm)	σ (H/L)
	±0,01	±0,05	±0,001	±10	±0.01	±1
L	7.21	16.81	0.680	102	1.73	20
H	45.91	4.25	0.911	143	1.20	20

As a result, Fig. C.3(a) shows the comparison between the ideal DBR previously designed (see table C.1) and the measured reflectance obtained for the experimental PSi DBR. As it can be seen, the bandwidth and intensity exhibit considerable reductions, while the position of the band remains about $\lambda_0 = 700$ nm. This fact is an indication of the scattering effect of rough interfaces. SEM images in Fig. C.3 (b) show the cross-section of the heterostructure that is composed by 15 periods of LH layers, and Fig. C.3 (c) corresponds an inside look where the rough nature of the interfaces is evidenced. Despite this, the fitted reflectance still disagrees to the experimental. This fact can be explained owing to optical losses generated by other lossy mechanisms such as surface absorption [112], bulk scattering, and the absorption due to quantum confinement produced by the c-Si walls of the high porosity layer (H) [41]. However, the above mentioned mechanisms only have effects over the intensity of the reflectance. This effect is also observed in the baseline level increased

in the spectrum. Fig C.3 (d) shows the frontal look of the films for layer H that exhibits spinodal interconnected porosity, so on walls thickness is about 15 nm that confirms the quantum confinement. The frontal look of layer L(Fig C.3 (e)) shows a regular distribution of porous.

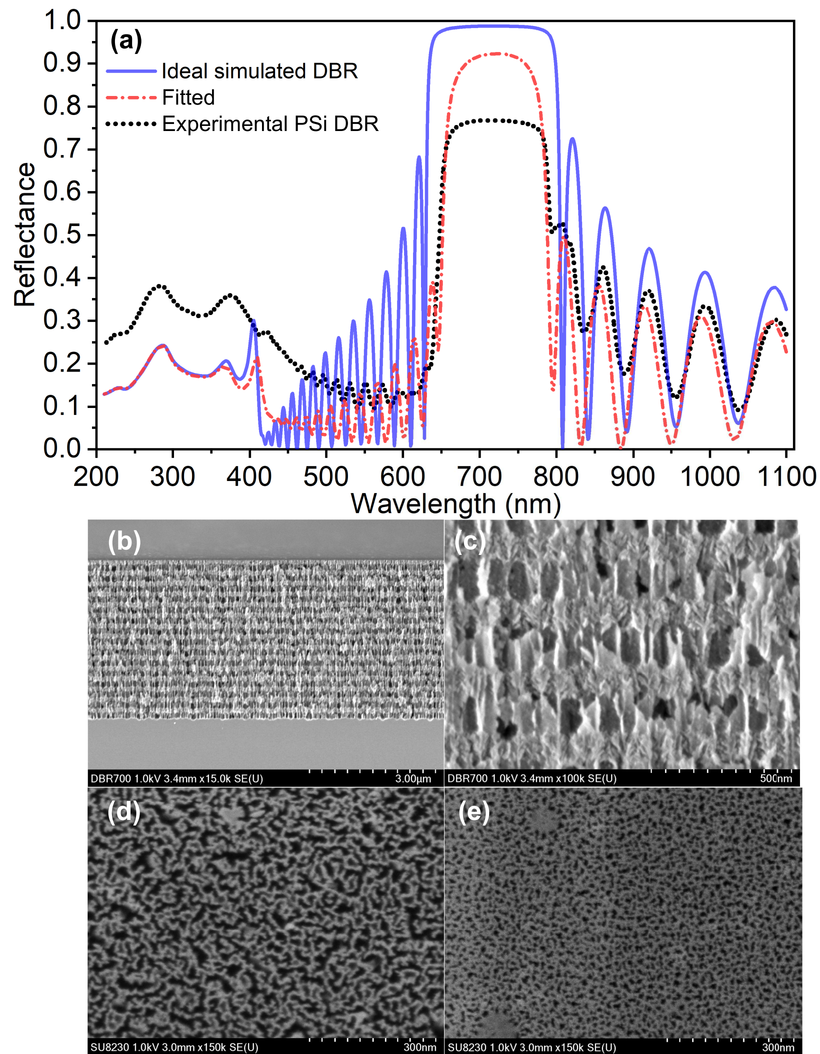

Figure C.3: (a) Comparison of the optical response of ideal PSi DBR (blue line), the fitted reflectance with a contribution of H/L interface roughness of 20 nm (red line), and the experimental PSi DBR fabricated (black line). (b) and (c) SEM images of cross section of PSi DBR. (d) and (e) correspond top view of high porosity and low porosity layer respectively.

Appendix D

Papers published during PhD studies

D.1. 2016

D.1.1. In situ photoacoustic characterization for porous silicon growing: Detection principles

C. F. Ramirez-Gutierrez, J. D. Castaño-Yepes, and M. E. Rodriguez-García.
Journal of Applied Physics **119**, 185103 (2016).
doi: 10.1063/1.4948946

D.1.2. Study of bovine hydroxyapatite obtained by calcination at low heating rates and cooled in furnace air

Sandra M. Londoño-Restrepo, **Cristian F. Ramirez-Gutierrez**, Alicia del Real, Efrain Rubio-Rosas, Mario E. Rodriguez-García.
Journal of Material Science **51**(9), 4431–4441 (2016).
doi: 10.1007/s10853-016-9755-4

D.2. 2017

D.2.1. Modeling the photoacoustic signal during the porous silicon formation

C. F. Ramirez-Gutierrez, J. D. Castaño-Yepes, and M. E. Rodriguez-Garcia.
Journal of Applied Physics **121**, 025103 (2017).
doi: 10.1063/1.4973940

D.2.2. Effect of the temperature and sintering time on the thermal, structural,morphological, and vibrational properties of hydroxyapatite derived frompig bone

C.F. Ramirez-Gutierrez, S.M. Londoño-Restrepo, A. del Real, M.A. Mondragónd, M.E. Rodriguez-Garcia.
Ceramics International **43**, 7552–7559 (2017).
doi: 10.1016/j.ceramint.2017.03.046

D.3. 2018

D.3.1. Photoluminescence study of porous p-type silicon: Identification of radiative transitions

Cristian F. Ramirez-Gutierrez, Andrés Medina-Herrera, Liliana Tirado-Mejía, Luis F. Zubieta-Otero, Orlando Auciello, Mario E. Rodriguez-Garcia.
Journal of Luminescence **201**, 11–17 (2018).
doi: 10.1016/j.jlumin.2018.04.036

D.3.2. Porosity and roughness determination of porous silicon thin films by genetic algorithms

C. F. Ramirez-Gutierrez, J. D. Castaño-Yepes, and M. E. Rodriguez-Garcia.
Optik **173**, 271–278 (2018).
doi: 10.1016/j.ijleo.2018.08.019

D.3.3. Optical interferometry and photoacoustics as in-situ techniques to characterize the porous silicon formation: a review

Cristian F. Ramirez-Gutierrez, Jorge D. Castaño-Yepes, and Mario E. Rodriguez-Garcia
Open Materials Science **4**, 23–32 2018.
doi:10.1515/oms-2018-0003

D.3.4. A comparative study on heat capacity, magnetization and magnetic susceptibility for a GaAs quantum dot with asymmetric confinement

J.D. Castaño-Yepesa, **C.F. Ramirez-Gutierrez**, H. Correa-Gallego, Edgar A. Gómez.
Physica E: Low-dimensional Systems and Nanostructures **103**, 464-720 (2018).
doi: 10.1016/j.physe.2018.05.022

D.3.5. The Influence of the Precipitation Heat Treatment Temperature on the Metallurgical, Microstructure, Thermal Properties, and Microhardness of an Alpha Brass

Ignacio Rojas-Rodríguez, Alberto Lara-Guevara, Mauricio Salazar-Sicacha, Julio Cesar Mosquera-Mosquera, Minerva Robles-Agudo, **Cristian Ramirez-Gutierrez**, Mario Rodríguez-

García.
Materials Sciences and Applications **9**, 440-454 (2018).
doi: 10.4236/msa.2018.9403

D.4. 2019

D.4.1. Effects of the interface roughness in the optical response of one-dimensional photonic crystals of porous silicon

I.A. Lujan-Cabrera, **C.F. Ramirez-Gutierrez**, J.D. Castaño-Yepes, M.E. Rodriguez-Garcia.
Physica B: Condensed Matter **560** , 133–139 (2019).

D.4.2. Impact of a topological defect and Rashba spin-orbit interaction on the thermo-magnetic and optical properties of a 2D semiconductor quantum dot with Gaussian confinement

Jorge David Castaño-Yepes, D.A. Amor-Quiroza, **C.F. Ramirez-Gutierrez**, Edgar A. Gómez.
Physica E: Low-dimensional Systems and Nanostructures **109**, 59–66 (2019).
doi: 10.1016/j.physe.2019.01.001

D.4.3. Chapter 14 - Study of microstructural, structural, mechanical, and vibrational properties of defatted trabecular bovine bones: natural sponges

Book title: Materials for Biomedical Engineering Hydrogels and Polymer-Based Scaffolds.
Edited by: Alina-Maria Holban and Alexandru Mihai Grumezescu.

Sandra M. Londoño-Restrepo, **Cristian F. Ramirez-Gutierrez**, Herminso Villarraga-Gómez, Mario E. Rodriguez-García, Pages 441-485.

doi: 10.1016/B978-0-12-816901-8.00014-6